UNIVERSITÀ DEGLI STUDI DI NAPOLI FEDERICO II

CHEMICAL SCIENCES DOCTORATE

XXXI CYCLE

Development of innovative materials for high efficiency polymer solar cells

Tutors:

Prof. Claudio De Rosa
Prof. Finizia Auriemma
Dr. Pasquale Morvillo

Candidate:

Carmen Sasso

Supervisor:

Prof. Michele Pavone

PhD Coordinator:

Prof. Luigi Paduano

Table of Contents

Chapter 3

Organic Photovoltaics (OPV): Experimental section

Chapter 4

Laminated flexible polymer solar cells (PSCs)

Chapter 5

Hybrid Nanomaterials

Chapter 6

Hybrid Nanomaterials: Experimental Section

Chapter 7

Appendix

Preface

Photovoltaics (PV) is one of main renewable energy technologies. It can potentially cope with growing global energy demand providing a more economical, sustainable and environmentally friendly energy than that produced by fossil fuels. In this scenario, polymer solar cells (PSCs) have attracted considerable interest thanks to their unique properties of low cost, easy fabrication, light weight and flexibility. Currently, the main challenge of this research field is to develop competitive devices having a correct compromise between efficiency and stability for versatile applications.

This PhD project is a collaboration between University of Naples "Federico II" and ENEA, Portici Research Center. The research activity about the laminated PSCs (vide infra) was carried out at Linköpings Universitet (Sweden) in the Research Group "Biomolecular and Organic Electronics" leaded by Prof. Olle Inganäs.

The present thesis focuses on the implementation of suitable strategies for the realization of polymer solar cells (PSCs) in order to improve the device performances.

The first part of dissertation is dedicated to the fabrication of the inverted bulk heterojunction (BHJ) organic solar cells with the purpose to study various active layer materials based both on low and wide band-gap polymers as donors and both on fullerene and non fullerene compounds as acceptors. Special attention is given to various aspects such as the optimization process of PSC structure to achieve the best electrical performance; the impact of thermal behavior of active layer materials on

the device performance and compatibility of chosen materials with printing and coating techniques in a view to develop feasible scale up processes.

In particular, a study of fully solution-processed PSCs and mini-modules, coated on flexible electrode and processed by roll lamination method, is also attempted during my stage abroad in Sweden. The interest for this approach is due to its intrinsic simplicity, low cost and the potential use for the flexible module fabrication for new indoor applications.

The last part of the present work is focused on the study of block copolymers (BCPs). Their ability to self-assemble into ordered nanostructures, with sizes in the nanometric range, is investigated in order to make active layers for hybrid PSCs based on well-ordered polymeric morphology hosting *n*- and *p*-type semiconductor nanoparticles (NPs) in target domains. The BCP approach is an effective way to prevent self-aggregation of the nanoparticles, maximizing, at the same time, the surface area at the interface between domains of material for carriers of opposite charge in order to promote efficient exciton dissociation and charge transport processes.

CHAPTER I

Introduction

1.1 Solar Energy

In the last years there has been a considerable increase in energy consumption. The global energy demand grew by 2.2% in 2017, up from 1.2% in 2016 with a 10-year average of 1.7%. In 2017, the total power consumption of the world's population rose to ~13500 million tons of oil equivalent. [1](Fig. 1.1)

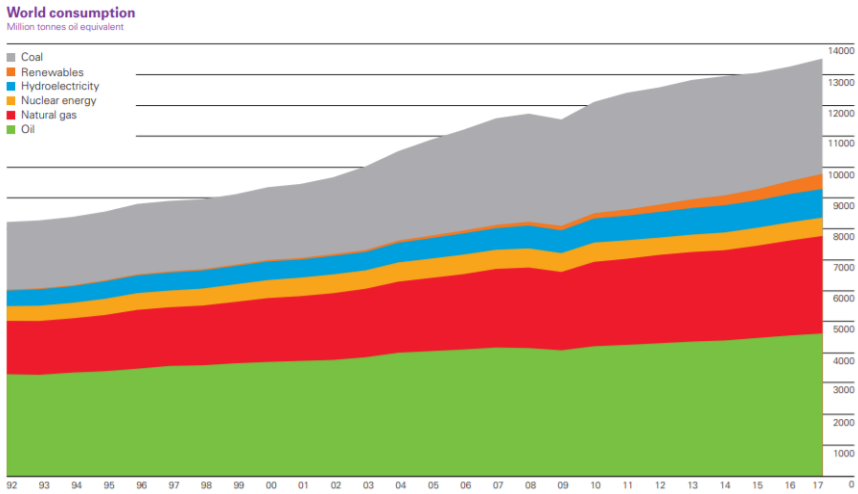

Fig. 1.1. World primary energy consumption in the period 1992-2017. [1]

Currently, the main energy sources are based on fossil fuels such as oil, coal, and natural gas, but their limited availability and their long-term harmful environmental impact have induced the need to develop new sustainable strategies.

The renewable energies are the potential kind of technology which can lead to a progressive and essential replacement of fossil fuels.
In particular, solar energy, among other renewable sources, is a clean, economical, abundant and freely available energy source.
A vast amount of energy in the form of solar irradiation (~ 101 PJ every second (~ 10^{15} W) [2], roughly 6700 times the current world consumption in a year reaches the surface of the Earth. Merely a small fraction would be enough for conversion to desired energy forms in order to manage long-term issues in energy crisis.
Solar industry is developing quickly all over the world to realize different technologies which allow to convert the sunlight into thermal or electrical energy.
The fastest and most efficient direct conversion of sunlight into electrical energy is possible through the *photovoltaic devices*.

1.2 Photovoltaics (PV)

In 1839 Becquerel, working on electrolytic cells, observed for the first time an electrical current in a material produced by light exposure. He discovered the *photovoltaic effect*. [3]. The concept of photoconductivity was shown for selenium by Smith in 1873 and in 1883 Fritts built the first solar cell made by gold coated selenium having a power conversion efficiency (PCE) of 1%. [4] The interest in selenium photovoltaics continued for the next several decades even if its commercial use was limited.
In 1902, Philip Lenard studied how the energy of the emitted photoelectrons varied with the intensity of the light. Later on, in 1905, A. Einstein gave a simple theoretically interpretation of Lenard's results,

receiving the Nobel Prize for this work in 1921. These studies allowed to obtain a better understanding of photo electricity achieving important scientific results in PV field in the 20th century.

In particular, the main advance in the development of solar cell technology occurred in 1954 at Bell Labs when the first silicon solar cell with an efficiency of around 6% was developed. [5] From that moment, solar cells have been intensively studied with the goal of reducing the costs and increasing the efficiency to make solar power more competitive with fossil fuels.

1.2.1 PV generations

Today solar cell technologies are divided into three generations (Fig. 1.2)

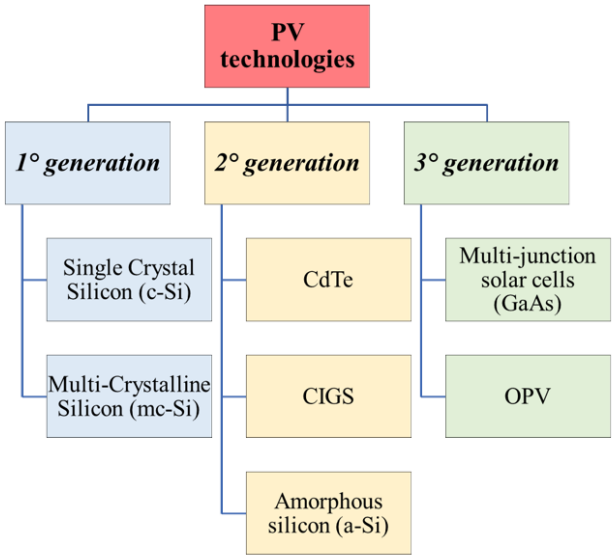

Fig. 1.2. Overview of main PV technologies.

First generation solar cells are characterized by single-junction solar cells based on silicon wafers including single crystal (c-Si) and multi-

crystalline silicon (mc-Si). These types of solar cells have reached record lab cell efficiencies of 26.7% and 22.3%, respectively. [6]
They are still predominant products in the PV market due to their good performance and their high stability. The main disadvantage is the cost of high-purity silicon. It is an indirect band-gap semiconductor with a weaker absorption than other semiconductors, so thicker layers of silicon are generally required to obtain the same properties. [7] Therefore, the research activities have been focused on the development of new technologies that can use less material such as thin films or smaller active layers.

The second generation solar cells are based on cadmium telluride (CdTe), copper indium gallium selenide (CIGS), amorphous silicon (a-Si).
These technologies can potentially achieve high conversion efficiencies but not in terms of stability (e.g. Staebler-Wronski effect in amorphous silicon solar cell). [8] Currently, CdTe solar cells have reached a record for laboratory efficiency of 21%, CIGS 21.7% and amorphous silicon of about 10%. [6]
An advantage of second generation materials is represented by the possibility to deposit thin films onto a glass or ceramic substrates to reduce material mass and so the production costs.

The third generation includes different types of solar cells:

1) multi-junction solar cells (i.e. GaAs cells);
2) organic solar cells (OSC), consisting of:
    - Dye-sensitized solar cells (DSSC),
    - Polymer solar cells (PSC)
3) Perovskite solar cells.

Multi-junction solar cells use multiple layers that are able to more efficiently convert different portions of the solar spectrum depending on the band gap of layers. The highest efficiencies reported for multijunction solar cells are over 45%. [9] but, up to now, it has been difficult to find a commercial application because of the high production costs.

As regards PSC, they have reached a record efficiency of 14.2% and for DSSC of 13%. [10, 11] The research interest in polymer solar cells is increased significantly in recent years due to the several advantages offered by this technology in terms of simplicity, speed and potentially inexpensive large-scale production.

Lately, a new class of thin film solar cells based on perovskite materials has achieved a record efficiency of over 20% on very small area. [12]

Moreover, unique features of the second and third generations like flexibility, transparency and lower costs have expanded the field of applicability for solar cells, i.e. indoor integration or recharging surfaces for electronic devices, compared to the limits of first one. [13, 14] Fig. 1.3 shows the record efficiency of different solar cell technologies that have been verified in 2018 by the National Renewable Energy Laboratory (NREL). [15]

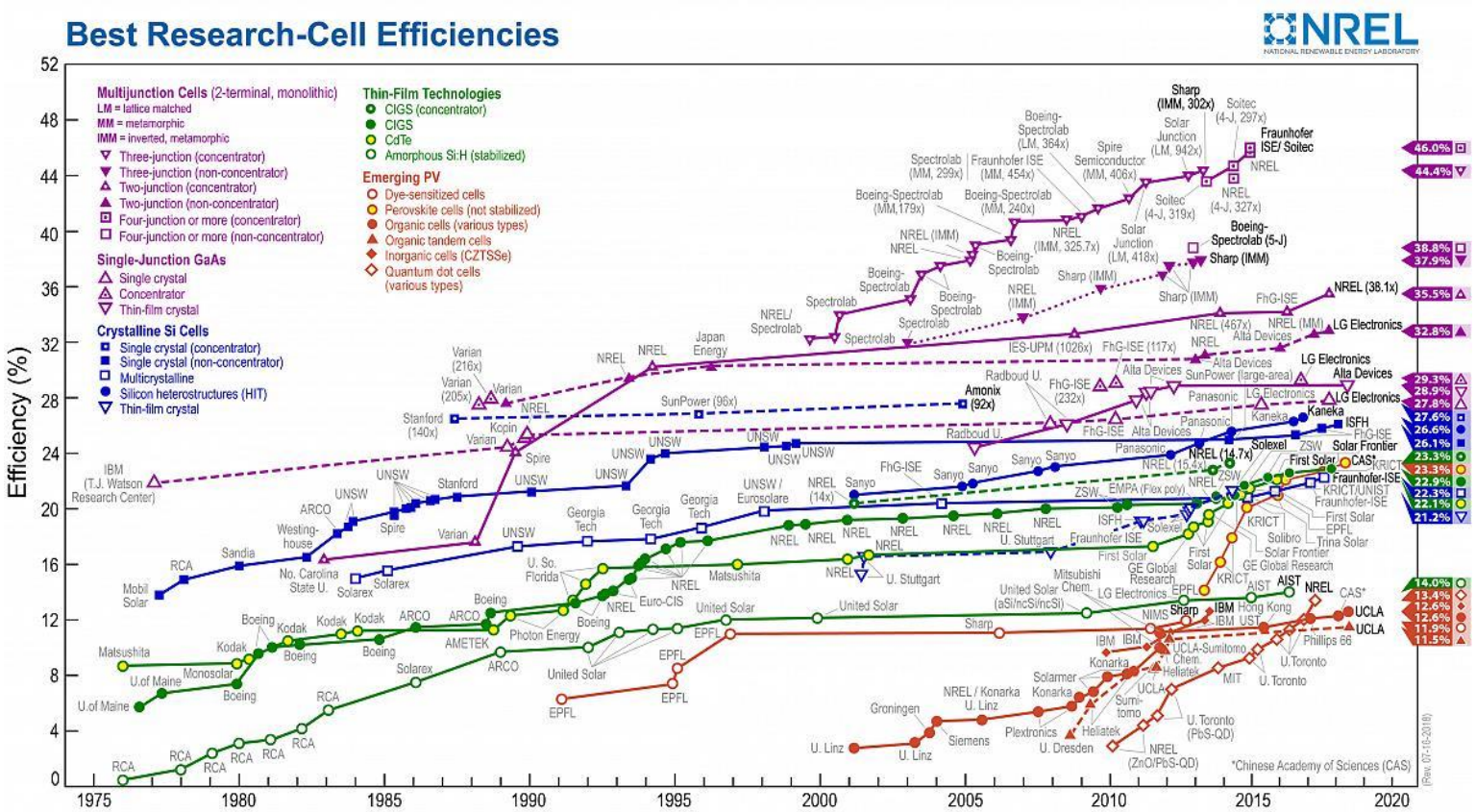

Fig. 1.3. Best research solar cell efficiencies reported by NREL (2018). [15]

1.3 Inorganic and organic semiconductors

This thesis will mainly focus on the realization of solar cells using both inorganic and organic semiconductor materials.

The organic semiconductors are conjugated materials, such as polymers or small molecules, where each carbon atom along the backbone form three sp^2 hybridized orbitals and one unhybridized p_z-orbital. The overlapping of sp^2 orbitals form σ-bonds (a lower energy bonding σ-molecular orbital and a higher energy antibonding σ*-molecular orbital) and the overlapping p_z-orbitals form π-bonds (π and π*-molecular orbitals) where the delocalization of π-electrons occurs along the conjugated backbone. [16, 17]
The energy difference between the highest occupied molecular orbital (HOMO) and the lowest unoccupied molecular orbital (LUMO) is the band-gap of material whose value for conjugated polymers is in the range of 1-4 eV. [18]
As regards the inorganic semiconductors, they are characterized by highly crystalline ordered structures where atoms are covalently bound and electrons are spatially delocalized over the crystalline lattice. The energy states allowed for these electrons form continuous energy bands, known as the semiconductor valence (VB) and conduction bands (CB), separated by an energy band-gap (Eg) whose values are in the same range of organic materials.

The main differences between inorganic and organic semiconductor materials are based on their electronic structures:

- *Charge transport.* In organic semiconductors, the charge carriers move through the conjugated backbone hopping from one localized state to the adjacent one, limiting the macroscopic charge transport. [19] This is fundamentally different from traditional inorganic compounds where the atoms are well ordered and the charge are free to move.

  Therefore, the charge carrier mobility in organic semiconductors is much lower than in most inorganic semiconductors.
- *Absorption coeffecient.* In the organic materials they are relatively high (α, the absorption coefficient, > 105 cm^{-1}). This is important for a photovoltaic device because in this way it is possible to capture most of the photons (within the absorption range) using a very thin layer (~100 – 200 nm) preserving a good charge transport. [20]
- *Exciton binding energy.* Organic materials generally have a low dielectric constant (ε_r = 2−4), so, after light absorption, tightly bound Frenkel excitons are formed. [21] The exciton is an electrically neutral quasiparticle consisting of an electron and a hole which are bound by electrostatic Coulomb force.

  On the contrary, in inorganic semiconductors, after photons absorption, free charges are instantly generated. The exciton binding energies for these materials are low, hence, the thermal energy available at room temperature of about 25 meV is sufficient to dissociate the exciton into free charges, whereas in organic materials, where the exciton binding energies are usually in the range of 0.3-1 eV [22], it is necessary to apply an additional electric field to dissociate it into free charge carriers.

1.4 Description of thesis work

This work targets on the study of new nanomaterials that can be used for the realization of polymer solar cells (PSCs).

The interest on PSCs concerns the unique properties of the polymer materials such as low production costs, compatibility with flexible and transparent substrates, the easy and environmentally friendly production and tunability of their optoelectronics properties.

Currently, the main challenge is to fabricate materials with these properties overcoming the main limitations linked to a low stability and efficiency. Indeed, in comparison to the inorganic photovoltaics, in PSCs technology both performance and stability are fundamental and complex issue to be solved before the commercialization. These two aspects can be due to several factors such as the type of chosen materials, the bulk-heterojunction morphology, the diffusion of electrode or buffer layer components into adjacent layers, light and heat.

This work aims to provide a systematic study of different materials and methods for the production of high efficiency PSCs using commercial deposition techniques investigating, at the same time, the main device degradation processes with particular attention to the effects induced by temperature.

In summary, the main tasks of present PhD thesis are:

1) Realization and optimization of bulk heterojunction (BHJ) PSCs compatible with printing techniques in terms of processability in air and thermal stability.
2) Realization of photoactive layers based on nanostructured inorganic hybrid materials combining the semiconductor

properties of nanoparticles (NPs) and self-assembly of block copolymers (BCPs).

The research activity, described here, was performed in collaboration with ENEA, Portici research center.

After this overview on the PV technologies and the main differences between the organic and inorganic semiconductor materials, the Chapter 2 introduces the working principles of organic photovoltaics (OPV) and summarizes the fabrication and characterization techniques used in the work.

The Chapter 3 is focused on the optimization of the PSC performances through a deeper study on the role of different materials with the aim of producing thermal stable and fully solution-processed devices.

The Chapter 4 regards the fabrication of flexible non fullerene ternary PSCs and mini-modules through the lamination process.

The Chapter 5 gives a description of the materials such as block copolymers (BCPs) and semiconductor nanoparticles (NPs), and methods used for preparing and characterizing the morphology of hybrid inorganic nanocomposites.

The Chapter 6 describes the results obtained in the characterization of the thin films based on semiconductor nanoparticles (NPs) and block copolymers (BCPs) to obtain a nanostructured hybrid material as photoactive layer.

The Chapter 7 is dedicated to the conclusions.

Bibliography of Chapter 1

[1] «BP Statistical Review of World Energy 2018,» [Online]. Available: https://www.bp.com/en/global/corporate/energy-economics/statistical-review-of-world-energy.html.

[2] A. Cho, *Science,* vol. 329, n. 5993, pp. 786-787.

[3] A. E. Becquerel, *Comptes Rendus,* vol. 9, pp. 561-567, 1939.

[4] C. E. Fritts, *American Journal of Science,* vol. 26, pp. 465-472, 1883.

[5] D. M. Chapin, C. S. Fuller and L. G. Pearson, *Journal of Applied Physics,* vol. 25, no. 5, pp. 676-677, 1954.

[6] M. A. Green, Y. Hishikawa, E. D. Dunlop, D. H. Levi, J. Hohl-Ebinger and A. W. Y. Ho-Baillie, *Prog. Photovolt. Res. Appl.*, vol. 26, pp. 3-12, 2018.

[7] S. S. Hegedus and A. Luque, in *Handbook of Photovoltaic Science and Engineering*, 2003, pp. 1-43.

[8] "Amorphous Silicon and Nanocrystaline Silicon Solar Cells.," [Online]. Available: http://siser.eps.hw. ac.uk/research/thin-film/amorphous-silicon-and-nanocrystaline-siliconsolar-cells.

[9] F. Dimroth, M. Grave, P. Beutel, U. Fiedeler, C. Karcher, T. N. D. Tibbits, E. Oliva, G. Siefer, M. Schachtner, A. Wekkeli, A. W. Bett, R. Krause, M. Piccin, N. Blanc, C. Drazek, E. Guiot, B. Ghyselen, T. Salvetat and A. Tauzin, *Progress in Photovoltaics: Research and Applications,* vol. 22, pp. 277-282, 2014.

[10] S. Li, L. Y. W. Zhao, H. Yan, B. Yang, D. Liu, W. Li, H. Ade and J. Hou, *J. Am. Chem. Soc.* , vol. 140, p. 7159−7167, 2018.

[11] S. Mathewetal, *Nature chemistry*, vol. 6, pp. 242-247, 2014.

[12] W. S. Yang, J. H. Noh, N. J. Jeon, Y. C. Kim, S. Ryu, J. Seo and S. Seok, *Science*, vol. 348, no. 6240, pp. 1234-1237, 2015.

[13] "Africa supplies green electricity. Completion of world's largest building-integrated OPV system.," 2015. [Online]. Available: http://www.sunflower-fp7.eu/site/images/images/News/BEL_PM_201509-29_CarlStahl-Addis_EN.pdf.

[14] "The OPV living room.," 2016. [Online]. Available: http://www.sunflower-fp7.eu/site/index.php/news/156sunflower-wins-the-best-publicly-funded-demonstrator-award-in-the-2016oe-a-competition.

[15] "The National Center for Photovoltaics," [Online]. Available: https://www.nrel.gov/pv/.

[16] M. C. Petty, M. R. Bryce and D. Bloor, in *Introduction to molecular electronics*, London, Edward Arnold, 1995.

[17] S. S. Sun and L. R. Dalton, in *Introduction to Organic Electronic and Optoelectronic Materials and Devices CRC Press*, Boca Raton,, 2008.

[18] W. R. Salaneck, R. H. Friend and J. L. L. Brédas, *Physics Reports*, vol. 319, pp. 231-251, 1999.

[19] D. Hertel and H. Bassler, *ChemPhysChem*, vol. 9, p. 666, 2008.

[20] L. Dou, J. You, Z. Hong, Z. Xu, G. Li, R. Street and Y. Yang, *Advanced Materials*, vol. 25, no. 46, pp. 6642-6671, 2013.

[21] J. Frenkel, *Physical Review*, vol. 37, pp. 17-44, 1931.

[22] R. Z. G. Li and Y. Yang, *Nature Photonics*, vol. 6, p. 153, 2012.

CHAPTER 2

Organic Photovoltaics (OPVs): The basics

2.1 Introduction

The structure of the organic solar cells is a stack of layers where the active layer can be considered as the *heart* of device.

It is placed in the middle of the stack and, according to its characteristics, it is possible to discern different OPV architectures (Fig. 2.1):

1) Single layer
2) Bilayer or planar heterojunction (PHJ)
3) Bulk heterojunction (BHJ)

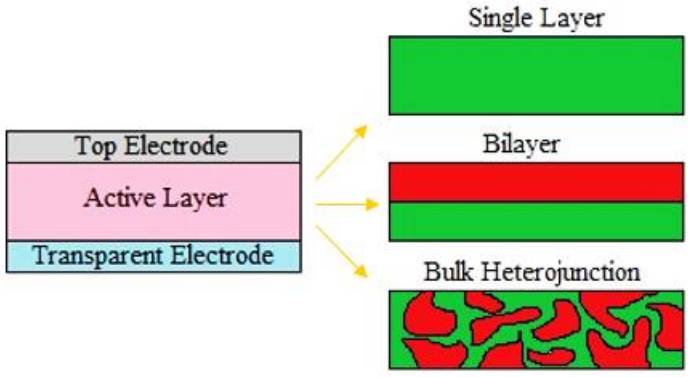

Fig. 2.1. Device structure of an organic solar cells.

The first example of organic solar cell was a single organic layer sandwiched between two electrodes having suitable work functions (WF). The electrical performances of this device were very low (~0.3%) due to poor charge mobility between the organic layer and the charges-extracting electrodes. [1]

To overcome the problems of single layer solar cells, Tang in 1986 introduced a new type of architecture: the *bilayer* structure or *planar* heterojunction. [2] This structure consists of stacking two different materials, *p*- and *n*- type organic semiconductors (this nomenclature is referred to the type of material conductivity), also called as donor (D) and acceptor (A) respectively, to create a *p*-*n* junction. In particular, thin layers of donor small molecules (copper phthalocyanine, CuPc) and acceptor molecules (perylene diimide derivative) were thermally evaporated between the transparent conductive substrate (indium thin oxide, ITO) and silver Ag top electrode. This bilayer device resulted in a surprising power conversion efficiency of ~1 % under an illumination of 75 mW/m^2, probably due to a better efficient charge separation at the donor-acceptor (D-A) interface.

A significant scientific progress occurred with the introduction of a new architecture, called *bulk heterojunction* (BHJ).

In such a device, the donor and acceptor materials are intimately mixed on a nanostructured scale (about 10 nm) at a certain ratio, so that the D/A interface is distributed throughout the device forming percolation pathways for the charges which can reach to the appropriate electrode.

In 1995, Gang Yu et al [3] reported a successful example of blend structure based on donor polymer MEH-PPV and a soluble derivative of C_{60}, [6,6]-phenyl C_{61} butyric acid methyl ester ([60]PCBM) as acceptor, yielding a PCE up to ~1.5% under low-intensity illumination.

From that moment, the BHJ has become the most common OPV structure and is developing quickly, achieving important results in terms of efficiency (~ 14 %). [4] Unfortunately, up to now, some main issues are still left unsolved such as the device lifetime and the large scale-production.

2.2 Working principles in organic solar cells

The basic working principles of organic solar cells are illustrated in Fig. 2.2 and can be summarize into different steps.

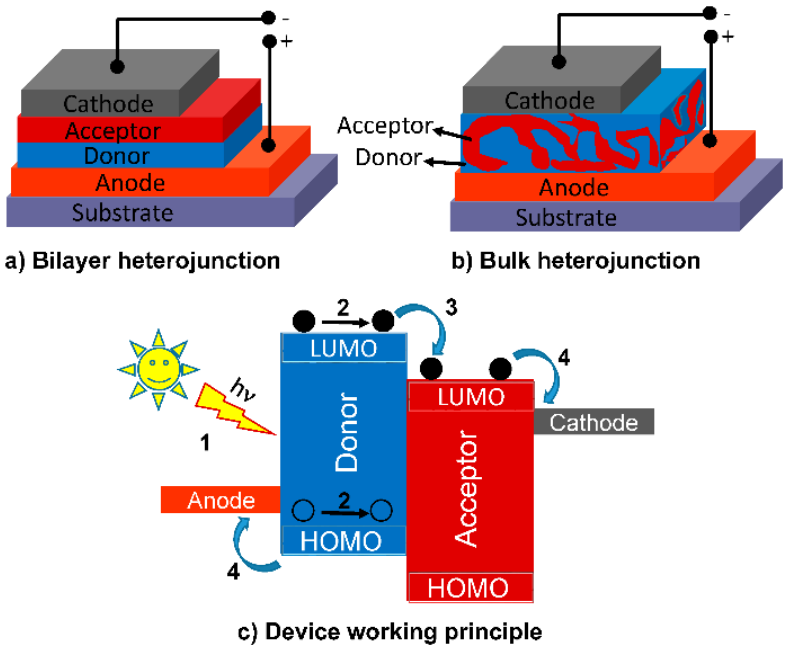

Fig. 2.2. Schematic representation of the steps in OPV devices. [5]

- *Photon absorption*

The first step is the absorption of a photon in the active layer. For this to happen, a fundamental condition has to be satisfied: the energy of the incident photon has to be equal or larger than the materials optical energy gap (Eq. 2.1):

$$E_{ph} \geq E_g \qquad Eq.2.1$$

In this way, there is the promotion of the electron from the highest occupied molecular orbital (HOMO), usually of the donor material, to the lowest

unoccupied molecular orbital (LUMO), usually of the acceptor material, and the subsequent formation of a Frenkel exciton.

The absorption is a crucial event and is defined by Lambert-Beer law (Eq. 2.2) which allows to determine the number of absorbed photons at a certain wavelength. In particular, the absorbance is given by:

$$A = log_{10}\left(\frac{I_0}{I_t}\right) = \alpha d \qquad Eq.\,2.2$$

where A is the absorbance, the incident light (I_0) and the light transmitted by the sample (I_t). The efficiency of light absorption is directly correlated to film thickness (d) and to the optical absorption coefficient (α). The α value, in turn, is defined by molar extinction coefficient (the ability to absorb light by a single molecule), the mass density and molecular absorption cross section.

In order to enhance the absorption, it occurs to find suitable materials with specific properties such as a high absorption coefficient, an optimized thickness of the stacks to not affect the mobility of free charge carriers and an optimal value the band gap of the polymer tuned to the solar spectrum in the way that it collects the highest number of photons possible.

- *Exciton diffusion to the donor/acceptor interface*

In organic materials the exciton binding energies are usually in the range of 0.3-1 eV [6] and the thermal energy available at room temperature (of about 25 meV) is not sufficient to dissociate the exciton into free charges. Therefore, the quasi-particle has to diffuse inside the donor material and reaches the D/A interface to be split before recombination (Fig. 2.3).

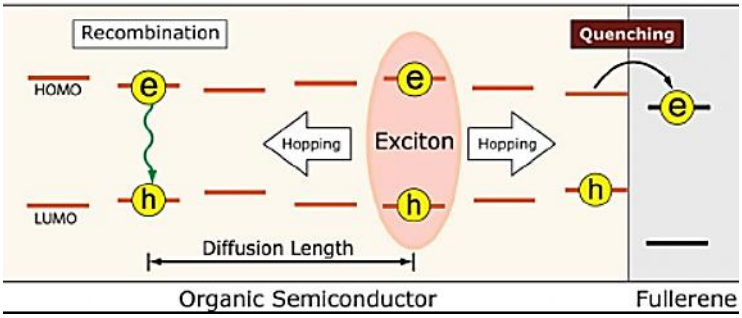

Fig. 2.3. Exciton diffusion to the donor/acceptor interface. [7]

An important parameter in this process is the exciton diffusion length (L_D) and it is given by the Eq 2.3:

$$L_D = \sqrt{D\tau} \qquad Eq.\,2.3$$

where D is the diffusion coefficient and τ is photoluminescence decay lifetime of the exciton. A longer diffusion length means a larger probability that the exciton reaches the interface (D/A) and is separated into free charges.

Generally, for conjugated polymers, the diffusion length is about of 10 nm. [8] For this reason, the morphology of the active layer plays an important role, in fact, it is necessary that the size of the domains is small enough in order that the process takes place and to prevent the recombination.

- *Exciton dissociation at the donor/acceptor interface*

Once the exciton diffuses to D/A interface, it can split into free charge if the energy difference between the ionization potential (I_P) of the donor material and the electron affinity (E_A) of the acceptor material is larger than the exciton binding energy. This process is usually very efficient and fast (order of femtoseconds). [9, 10]

At this point, the charge carriers are spatially separated but still bound by Coulombic forces at the interface, thus, an electric field is needed. This is

obtained by the different work-functions of the bottom and top electrodes of device. If this difference is sufficiently high, the separated charges can reach the contacts, otherwise the geminate recombination takes place.

- *Charge transport*

After the dissociation, the free charges have to travel through the donor and acceptor materials to the respective electrodes for extraction.
The only possible loss mechanism is the recombination between electrons and holes. In a bilayer structure, the recombination probability of charges should be low, because electrons and holes are placed in two different and spatially separated layers, whereas, in a bulk heterojunction, the intermixed phases could lead to non-geminate recombination between electrons and holes originated from different electron-hole pairs.
Generally, charge transport mechanisms can be classified as *band transport* for highly purified molecular crystals or *hopping transport* for amorphous organic semiconductors.

- *Charge collection at the electrodes*

Once the electrodes are reached, the charge carriers can be extracted. The efficiency of the process is determined by the good match between the work functions (WF) of the electrodes and the frontier orbitals energy of the donor and acceptor materials (Eq. 2.4 - 2.5). In particular:

$$WF_{anode} \geq HOMO_{donor} \qquad Eq.2.4$$

$$WF_{cathode} \leq LUMO_{acceptor} \qquad Eq.2.5$$

If these energy conditions are verified, a good energy level alignment, known as ohmic contact, is realized and, hence, there is the injection of charges at the corresponding electrodes. On the other hand, if the electrode/organic contact is non-ohmic, the energy level misalignment could lead to electrical losses for the device. In these cases, anode and cathode interlayers are used to improve the energy level alignment between the active layer and the metal contacts, and to enhance the device performances.

An important issue is that one of the electrodes has to be transparent to the light. The most used substrate is the highly conductive Indium Tin Oxide (ITO). It is a heavily-doped *n*-type semiconductor (typically 90% In_2O_3, 10% SnO_2 by weight) with a large bandgap of around 4 eV [11] and mostly transparent (>80%) in the visible region of the solar spectrum. [12] On the contrary, it is opaque in the ultraviolet because of band-to-band absorption and also in the near infrared, because of free carrier absorption.

The other electrode is usually a metal, such as: Al, Ca, Au, Ag, that is evaporated over the active layer and its charge extraction ability is depending on the type of organic buffer material.

2.3 Advantages and limits of organic solar cells

The polymer solar cells (PSCs) have many potential advantages such as flexibility, low material costs and low weight. Thanks to these features and compatibility with a wide range of substrates, they present a good versatility in several production methods included solution processes, high throughput printing techniques and roll-to-roll (R2R) technology.

Moreover, the PSC manufacturing process allows to consume less energy than the amount required for conventional inorganic cells. For this reason,

PSCs technology should be considered an eco-friendly method but, actually, it is not completely sustainable due to the toxicity of some used components such as PET, ITO and halogenated solvents in the inks.
Therefore, in the last years the research activity has been focused on development of new green materials able to replace the toxic ones.
Regarding organic materials, an important advantage is the ability to tune the molecular properties (molecular mass, bandgap, and ability to generate charges) to obtain a series of desirable properties for specific applications.
Currently, the main PSCs disadvantages are their low efficiency and short lifetime. The fast degradation is mainly due to different chemical and physical factors which can be harmful for the solar cells, for example water, oxygen, light and temperature.
For this reason, the polymer solar cells cannot yet replace silicon cells in the energy conversion field.
Nevertheless, the light-weight, the compatibility with transparent and flexible substrate, added to the potential processability through high-throughput printing techniques, allow to use the OPV technology in different and innovative applications such as recharging surfaces for laptops, phones or window integrations.

2.4. OPV geometries and Materials

An important step in building organic solar cells is choice of the best geometrical layout to enhance the device performance. There are two type of structure, known as *conventional* and *inverted* geometries. (Fig. 2.4)

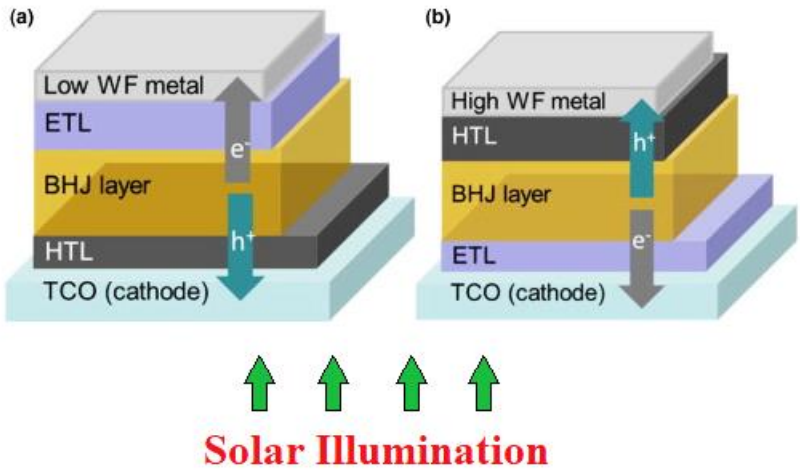

Fig. 2.4. a) Conventional and b) Inverted OPV geometries.

The conventional geometry, also called as "standard device", has been studied for a long period of time, thanks to good efficiencies and relatively easy production. [13, 14] Nevertheless, there are several drawbacks that can be considered detrimental:

- *poor reproducibility* of results [15];
- *air instability* due to the use of low work function metals, like Al, responsible for very fast oxidation when exposed to air and, thus, producing conductivity losses.
- *vertical phase separation*: a stratified composition of blend components occurs during the film formation [16, 17]. It is noticeable for polymer-fullerene based solar cells where the fullerene phase (acceptor) is mainly concentrated at the bottom of the film whereas the polymer phase (donor) at the top of the film, creating unfavorable situation for the proper functioning of an PV device.

Most of these problems have been overcome with the introduction of the "inverted geometry" where the polarity of charge collection is reversed by forcing electron to transparent conductive substrate (i.e. ITO) that acts as cathode while the top metal electrode, like silver or gold (Ag or Au), acts as anode thanks to a high work function electrode.
Several studies have demonstrated the better performances of inverted architecture than the normal one. [18, 19, 20] The better stability associated to a reduced corrosion at contact interfaces allows the use of this geometry in printed electronics field and the application to roll-to-roll (R2R) processing methods.
All the devices presented in this thesis were made using inverted geometry.

Another important issue for fabricating process is the choice of materials forming the BHJ solar cells, such as semiconductor polymers, acceptor and interfacial materials.
In the following sections the main features of the used OPV materials are described.

2.4.1 Interface materials

In order to achieve good performances, the introduction of a hole transport layers (HTLs) and an electron transport layers (ETLs) in a bulk heterojunction (BHJ) is mandatory. Their role, as mentioned above, is that to fulfil three main functions [21]:

a) *Selective contacts*: Reduction of charge leakage at the contacts by blocking charge transfer such that HTL blocks electrons and ETL blocks holes. This is possible due to a high LUMO (HOMO) offset between buffer and active layer.

b) Ohmic contact to electrodes: The interlayers are highly conductive and allow to improve the energy level alignment at the interfaces between the active layer and the electrical contacts.

c) Optical spacer: The interlayers are highly transparent material due to a wide band-gap for improving the light absorption thereby enhancing the photocurrent.

The interfacial materials used in this thesis are described as follows.

2.4.1.1 Electron Transport Layer (ETL)

Among the *n*-type metal oxides used in inverted PSCs, Zinc Oxide (ZnO) is an interesting interfacial material due to its high transparency in the visible range, relatively high electron mobility, appropriate energy band structure and environmental stability. [22, 23, 24, 25]

ZnO can act as hole blocking layer because its valence band is much lower than HOMO of the materials (polymers and fullerenes) usually employed in the realization of the blend. In addition, the possibility to be easily processed *via* a solution method, followed by low temperature annealing, makes ZnO fully compatible with flexible substrates using R2R methods. [26]

Very thin layers of ZnO can be easily obtained by means of different deposition techniques, like sol-gel [27], spray-coating [28] and nanoparticle (NP) deposition. [29]

In this work, the inverted PSCs were realized by using a sol–gel derived ZnO thin films, as electron transport layer, obtained starting from a solution of zinc acetate and ethanolamine in 2-methoxyethanol deposited on ITO substrates and annealed at T=150 °C for 5 minutes.

One of the most important parameters that determines the overall performances of the device is the morphology (and, consequently, the roughness) of the ZnO layer.
In particular, it has been shown that the annealing temperature is a key factor in order to determine the optimal morphology of the layer. The low-temperature annealing process (T=150°C) prolongs the presence of solvent molecules in the thin film producing nano-ridges morphology. This is useful because it increases the contact area between the active layers and the ETLs with consequent improvement of the absorption and the photogeneration inside the overlying blend. [30, 31, 32]

2.4.1.2 Hole Transport Layer (HTL)

The most important HTLs used for the fabrication of inverted BHJ are polymers, like poly(3,4-ethylenedioxythiophene) polystyrene sulfonate (PEDOT:PSS), or transition metal oxides, like MoO_x, V_2O_5, WO_3, NiO.
In this research activity, emphasis was given to the use of two among these materials: evaporated MoO_x and the solution-processed PEDOT:PSS.

a) Molibdenum Oxide (MoO_x)

Generally, molybdenum oxide layer greatly improves the electrical device performances. For this reason, it has been widely used as hole selective layer for both inverted [33, 34, 35, 36] and standard PSCs. [37, 38]
The mechanism of hole transport, that occurs in a nanostructured MoO_x layer, is described as an hopping process of the holes *via* the shallow defect states present in its band gap formed as a result of oxygen vacancies. [39, 40, 41, 42]

This material presents interesting properties due to its high work function and tunability of its physical, chemical and electronic properties.

The main advantages are the reduction of the charge recombination by suppressing the exciton quenching and the resistance at the photoactive layer/anode interface [42, 43] and the better air stability in inverted structure compared to the conventional one. [36]

Moreover, several research group have demonstrated that the improvement of overall performances can depend on a variation of the MoO_x thickness [44, 45, 35] and on the post-processing thermal treatment. [46] In particular, it has been shown that the thermal annealing on the device is deleterious for the interface between MoO_x and Ag due to a diffusion of silver ions and oxygen inside the active layer and, thus, MoO_x layer evolves into an alloy of Ag and MoO_x. [45]

There are different methods to deposit a thin MoO_x layer on substrate such as from dilute solution or through thermal evaporation. The latter method has been effectively used in the fabrication of the devices presented in this work.

In general, thermal evaporation is the best technique but it is uneconomical in the upscaling of PSCs and represents a limiting step in an otherwise fast roll-to-roll production line. In particular, one of the key points of this research activity was the replacement of evaporated materials with solution-processed alternatives.

PEDOT:PSS

One of the most used HTL layers in both inverted and standard devices is poly(3,4-ethylenedioxythiophene):polystyrene sulfonate, known as PEDOT:PSS.

It is a polymeric salt with insoluble PEDOT in its oxidized state with a positive charge and PSS having a deprotonated sulfonyl group carrying a negative charge.

The PEDOT:PSS structure is reported in Fig. 2.5.

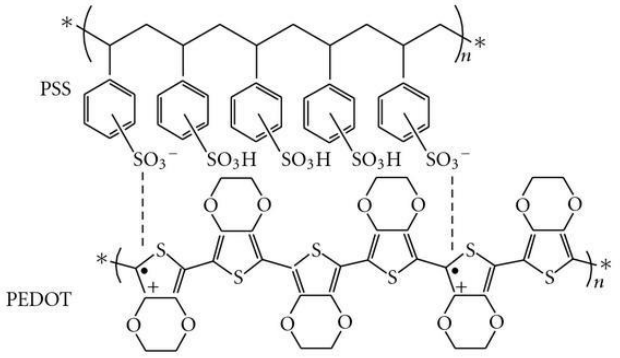

Fig. 2.5. Chemical structure of the PEDOT:PSS.

PEDOT:PSS is a water soluble and insoluble in common organic solvents. The interest for this interfacial material is due to its high transparency in the visible range, good electrical conductivity (> 200 S/cm) [47], excellent electrochemical and thermal stability, high charge carrier mobility [48] and compatibility with printing processes.

Nevertheless, there are several drawbacks. This material is highly hygroscopic, in fact it retains a large fraction of water (10-15 wt%) [49, 50] and has hydrophilic nature. It means that a bad film morphology and worse electrical properties can occur when deposited as the HTL onto the hydrophobic active layer in inverted devices. [51, 52] In order to increase the wettability on hydrophobic surface, it is possible to use surfactants which allow to have the van der Waals-type interactions between the hydrophobic alkyl backbone and the hydrophobic active layer surface,

making the organic layer hydrophilic with subsequent good PEDOT:PSS film forming properties on top. [53]

PEDOT:PSS solution used in the present work was prepared by using Heraeus Clevios™ P VP AI 4083 with a ratio of 1:6 of PEDOT to PSS, and a conductivity of the order of 10^{-3} S/cm. [49]

2.4.2 Active Layer materials

The most important part in a BHJ solar cell is the light absorbing active layer. It is formed by a blend of a donor and an acceptor material.

Currently, the main challenge of OPV field is to develop materials able to achieve optimal efficiencies and high stability in different environmental conditions. At the same time, other important features are low costs, compatibility with printing techniques and to process for large scale productions.

The following sections describe the basic properties of used donor and acceptor materials.

2.4.2.1 Donor materials

Polymer semiconductors are promising materials that can be potentially applied for large scale OPV production.

Polymers used in OPV are characterized by being highly π-conjugated. In fact, the presence of delocalized energy states within the structure allows to promote an efficient intermolecular transport and to guarantee an optimal optical absorption.

In order to achieve high performance solar cells, an ideal polymer has to satisfy some criteria: [54, 55]

1. a high solubility and a good solution processability;

2. broad absorption spectrum, complementary to the *n*-type material one;

3. a bandgap in the 1.30−1.90 eV range, with a deep HOMO energy level (≤ -5.20 eV);

4. high hole mobility.

Among conducting polymers, polythiophene and its derivatives are the mainly investigated materials for PSCs. This polymer class follows the mentioned criteria such as the tunability of band-gap and their optical properties, [56, 57] good solution processability, [55, 58] high stability and lifetime. [59]

In this regards, the most studied conducting polymer has been poly(3-hexylthiophene) (P3HT) due to its highly crystalline structure, with an HOMO level of 5.2 eV and low band-gap of 1.9 eV and high hole mobility ($\sim 10^{-4}$–10^{-3}) $m^2V^{-1}s^{-1}$ [60, 61]. The best efficiency for P3HT:PCBM based OPV devices was reached in 2005 and is around 5%. [14]

More recently, novel and efficient donor materials were synthetized. They are based on the combination of alternated electron rich and electron poor units in so called *push-pull* or *donor-acceptor* structures.

The most representative polymers for this category are:

- ✓ poly[[4,8-bis[(2-ethylhexyl)oxy]benzo[1,2-b:4,5-b']dithiophene-2,6-diyl] [3-fluoro-2[(2-ethylhexyl)carbonyl] thieno[3,4-b] thiophenediyl], known as PTB7, which have a high hole mobility of 5.8×10^{-4} $cm^2V^{-1}s^{-1}$, HOMO level of 5.15 eV [62] and a narrow band-gap of 1.8 eV, [50]
- ✓ poly[[2,6´-4,8-di(5-ethylhexylthienyl)-benzo[1,2-b;3,3-b]dithiophene][3-fluoro-2[(2 ethylhexyl)carbonyl]-thieno[3,4-b]thiophenediyl]], also called PTB7-Th or PCE10, with an even narrow

band gap of 1.59 eV which is closer to the optimum bandgap (~1.1–1.5eV) for a single-junction cell, as proven by Shockley and Queisser after considering all optical losses. [63] The best efficiency for inverted PTB7-Th:[70]PCBM-based PSCs is 10.3%. [64]

Another example of donor-acceptor polymer is poly[2,3-bis-(3-octyloxyphenyl) quinoxaline-5,8-diyl-alt-thiophene-2,5-diyl] (TQ1). TQ1 is an alternating copolymer that consists of thiophene, the donor-like unit, and quinoxaline, acceptor-like unit. The PSCs based on TQ1 and fullerene achieved an efficiency of ~7%. [65]

A promising electron-donating copolymer is poly[(2,6-(4,8-bis(5-(2-ethylhexyl)thiophen-2-yl)benzo[1,2-b:4,5-b']dithiophene))-alt-(5,5-(1',3'-di-2-thienyl-5',7'bis(2-ethylhexyl)benzo[1',2'-c:4',5'-c']dithiophene-4,8-dione))]), or known as PBDB-T. It, used in combination with small molecules acceptor (ITIC), has exceeded the PCE barrier of 11%. [66]

Fig. 2.6 shows some chemical structures of the polymers described in this paragraph and used for the fabrication of inverted PSCs in the present thesis work.

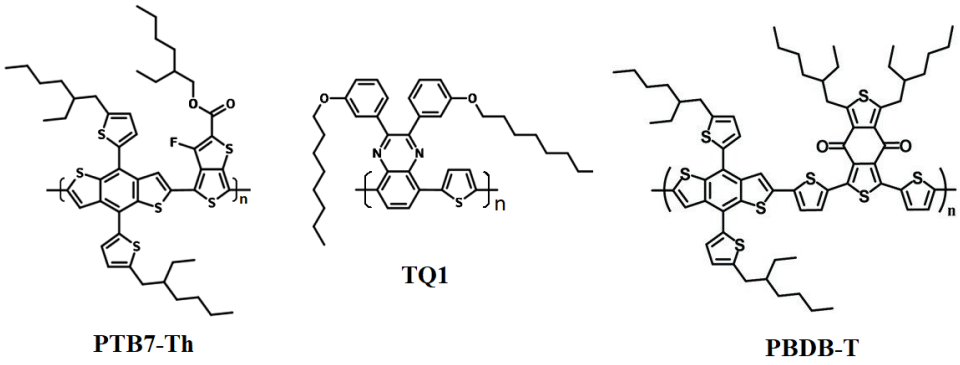

Fig. 2.6. Molecular structure of the donor materials used in this thesis.

2.4.2.2 Acceptor Materials

The most used electron acceptors in OPV are fullerene derivatives. Their structure consists of fullerene cage with suitable functional groups which help to improve the low solubility in the common organic solvents.
The two most important examples are (Fig. 2.7):

1. [6,6]-phenyl-C61-butyric acid methyl ester, known as [60]PCBM
2. [6,6]-phenyl C71-butyric acid methyl ester, also called [70]PCBM

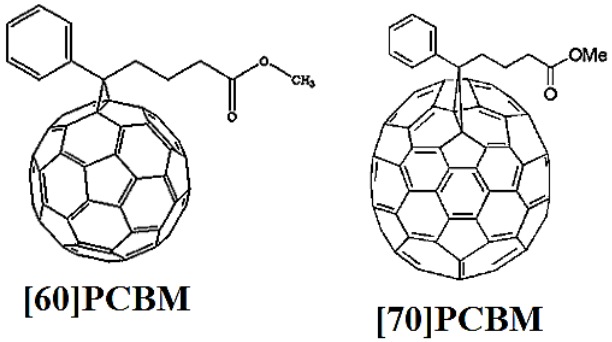

Fig. 2.7. Molecular structure of [60]PCBM and [70]PCBM.

The main advantages derive from the 3D-conjugated cage structure and they are:

- the ability to easily accept electrons due to a high electron affinity [67]
- the reasonably good electron mobility [68] thanks to efficient delocalization of the molecular orbitals across the 3D fullerene cages. [69]

Nevertheless, there are also some significant disadvantages which limit the device performances such as a poor tunability of frontier molecular orbitals (FMOs), a very low absorption in the UV-visible range, the strong tendency of fullerenes to aggregate and the very high costs.

In order to overcome many of these issues, the research activity has been focused on their replacement with adequately designed acceptor materials. Non-fullerene acceptors (NFAs) are an attractive alternative characterized by a *pull-push* structure, similar to donor polymers, which allows to absorb strongly in the visible and near IR region of the solar spectrum. Moreover, their structure can be easily modified tuning conveniently the LUMO energy levels to achieve higher V_{OC} in devices or introducing the steric hindrance in derivatives bearing alkyl chains to improve solubility and simultaneously prevent aggregation phenomena. [70]

Currently, the most promising replacements for fullerenes are an interesting class of electron acceptors, called acceptor–donor–acceptor (A–D–A) calamitic-type small molecules. Their structure consists of an electron rich donor central core flanked on either side by electron deficient acceptor units. [70]

Notable are the A–D–A small molecules based on Indacenodithiophene (IDT) or indacenodithienothiophene (IDTT) core that are characterized by strong electron donating and planar structures and good stability.

A good NFA example is 9-bis(2-methylene-(3-(1,1-dicyanomethylene)-indanone))-5,5,11,11-tetrakis(4hexylphenyl)-dithieno[2,3-d:2’,3’-d’]-s-indaceno[1,2-b:5,6-b’]dithiophene, also known as ITIC. This acceptor consists of IDTT unit as the core and has a band-gap of 1.59 eV. When paired with PBDB-T, the OPV devices exhibited a high power conversion efficiency (PCE) of 11.21%, excellent thermal stability and promising photovoltaic properties.

However, the best efficiency (11.34%) was achieved using ITIC with a wide bandgap donor polymer, named PBQ-4F. [71]

Other two important examples of small molecule acceptors are O-IDTBR and O-IDFBR. The former made use of the IDT core which involves a narrow band-gap (1.63eV) and a good structural planarization whereas the latter uses an indeno[1,2-b] fluorene moiety as its electron rich core.

In a recent report it has been shown how the combination of these two acceptors with P3HT polymer clearly improves the electrical performances of ternary OPV devices achieving a high efficiency of 7.7%. [72]

In recent years, the use of NFAs has become predominant due to the several advantages and, for this reason, the research activity is constantly focused on developing new approaches to improve molecule design and device performances.

The chemical structures of described small molecule acceptors are reported in Fig. 2.8.

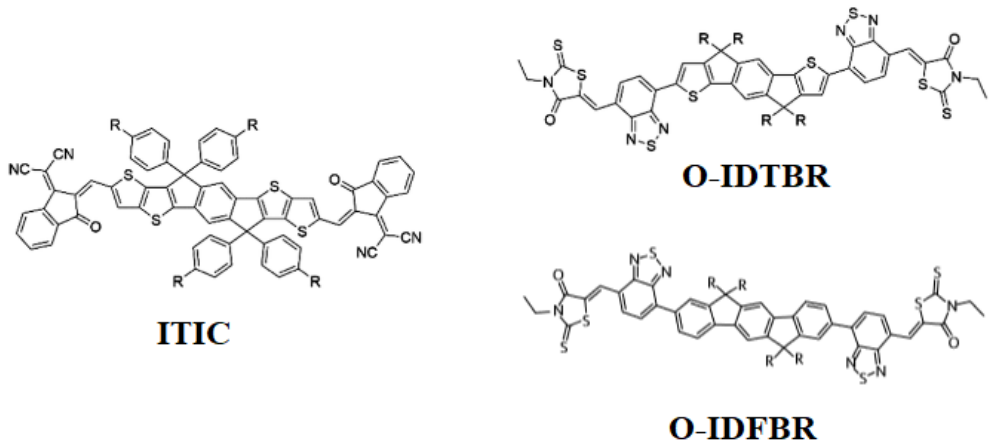

Fig. 2.8. Molecular structure of the small molecule acceptors used in this thesis.

2.5 Methods

The fabrication process of polymer solar cells (PSCs) is crucial and consists of several steps that can be summarized as follows:

1) Substrate preparation (cleaning and ITO photolithography)
2) Interfacial and active layers deposition
3) Back electrode deposition

During the present PhD activity, the different PSC layers were deposited by using:

- Solution processing methods (coating and printing techniques for thin liquid layer deposition);
- Evaporation techniques (i.e. thermal evaporation).

The main used fabrication and characterization techniques for the realization of inverted PSCs are described in the following sections.

2.5.1 Substrate preparation

In microelectronics, the substrate preparation is a fundamental step for obtaining reproducible results.

The solar cells presented in this thesis were realized using indium tin oxide (ITO) as a transparent substrate. Thin films of ITO are commonly deposited on glass surfaces by physical vapor deposition, electron beam evaporation or sputter deposition techniques.

The used glass/ITO substrates were purchased from Delta Technologies with a transparency ≥85%, a thickness of about 160 nm and a sheet resistivity ~12 Ω/sq.

The substrate preparation was based on photolithographic patterning of ITO to define the electrode geometry (Fig. 2.9), cutting the ITO coated-glass in the suitable sizes (20 mm x 20 mm), and the subsequent rigorous washing procedure to remove dust and impurities on the surface, since they could be deleterious for fabrication process and device performances.

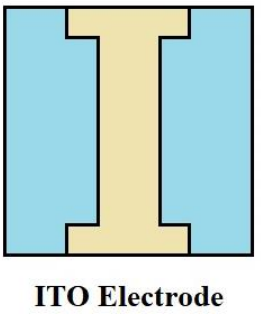

Fig. 2.9. ITO pattern onto glass substrate after photolithography process.

The cleaning procedure was as follows: initially, the substrates were sonicated in a hot water ultrasonic bath (~80°C) with Deconex detergent for 2h, followed by several rinses with DI water. After this, ultrasonic baths of acetone and isopropanol (15 min each) were used. Finally, the substrates were dried in vacuum at 130°C overnight.

2.5.2 Thin film deposition techniques

This is an overview on different thin film deposition techniques, coating and printing, used in this work to deposit the active and/or interfacial layers from solution.

They can be distinguished in methods compatible with laboratory-scale production and methods compatible with roll-to-roll (R2R) large-scale production.

- ***Spin coating***

The spin coating is the main method used on lab-scale to obtain thin films with high reproducibility and good uniformity. The thickness of the films depends on the angular spinning speed, the concentration of the solution, the molar mass and the distribution of molar masses of the used polymer. [73]

The theoretical aspects have been investigated by Emslie and Meyerhofer. [74, 75]. They developed semiempirical equations to define the thickness of layer. In particular, the variation of the film thickness is a function of time and is directly proportional to the inverse square root of the angular spinning speed.

Basically, a certain amount of solution is deposited onto substrate. Then, it starts to rotate and the solution is spread evenly over the surface by centrifugal force, with excess solution ejected off the edge. Solvent evaporation occurs while the substrate is still spinning and, finally, there is the formation of a thin and uniform film covering the substrate. (Fig. 2.10)

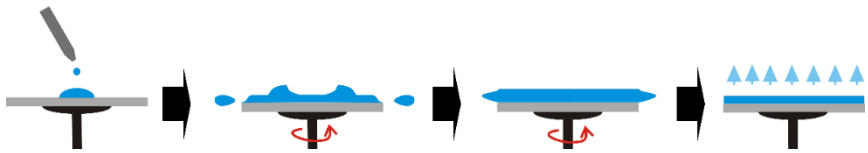

Fig. 2.10. Steps of spin coating process.

If the concentration of the solution, the substrate surface and the amount of solution deposited on the substrate are constant, higher angular speed means that the film will be thinner. The spinning time is determined by the boiling point of various used solvents.

- ***Blade coating***

Blade coating is a simple and cheap printing techniques compatible for large area production on rigid or flexible substrates.

The technique is based on the use of a sharp blade at a fixed distance from the substrate surface. The coating solution is then deposited in front of the blade that is then moved across the substrate forming a thin film. (Fig. 2.11)

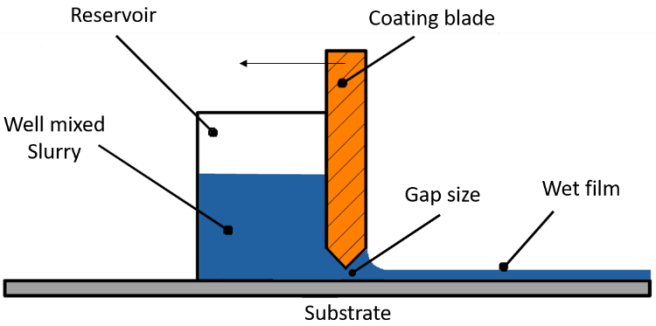

Fig. 2.11. Blade coating process.

The final thickness, *d*, is roughly half of the gap width depending on the coating speed and flow behavior [76] and can be empirically calculated according to Eq. 2.6:

$$d = \frac{1}{2}\left(g\frac{c}{\rho}\right) \qquad Eq.\,2.6$$

where g is the gap distance between the blade and the substrate, c is the concentration of the solid material in the coating solution (g*cm^{-3}) and, ρ is the density of the material in the final film (g*cm^{-3}). [77]

The main disadvantage of this method is the low speed that could lead to the aggregation or crystallization at high concentration of materials during the coating process.

- ***Screen printing***

Screen printing is one of the oldest printing techniques that began to develop in the early 1900s.

It allows to print very thick layers using primarily viscous materials. It is normally useful for printing electrodes.

There are two different types of screen printing: flatbed (Fig. 2.12) and rotary screen printing.

In this thesis, only the first one was used. The technique works through a squeegee that moves along the horizontal plane, forces the ink paste through the opening of the mesh and forming the desired motif on the substrate.

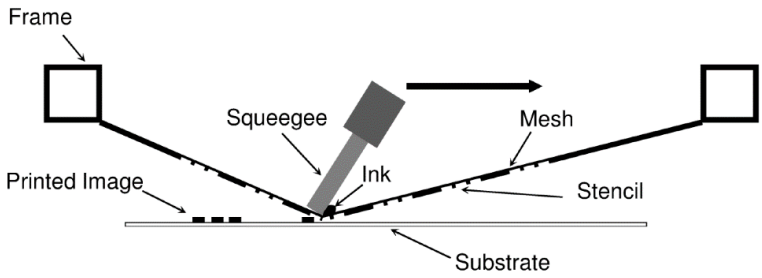

Fig. 2.12. Screen printing process.

The main advantages are the low cost of masks and the possibility to print on very large areas (on the scale of 10 square meters). [78]

- ***Slot die printing***

Slot-die coating is one of many methods to deposit a thin liquid film onto a substrate. Its main feature is the ease of integration into scale-up processes (like roll-to-roll coating).

This technique is robust and simple in operation and allows to coat stripes of material useful for making, for example, solar modules.

There are several advantages related to the use of this printing technology such as high levels of coating uniformity across the length/width of the coating surface, a deposition of variable thin-films thicknesses ranging from a few nanometres to many micrometres and the use of a wide range of solution types and viscosities.

The instrument used in the present activity was FOM Technologies Mini Roll Coater (MRC) shown in Fig. 2.13.

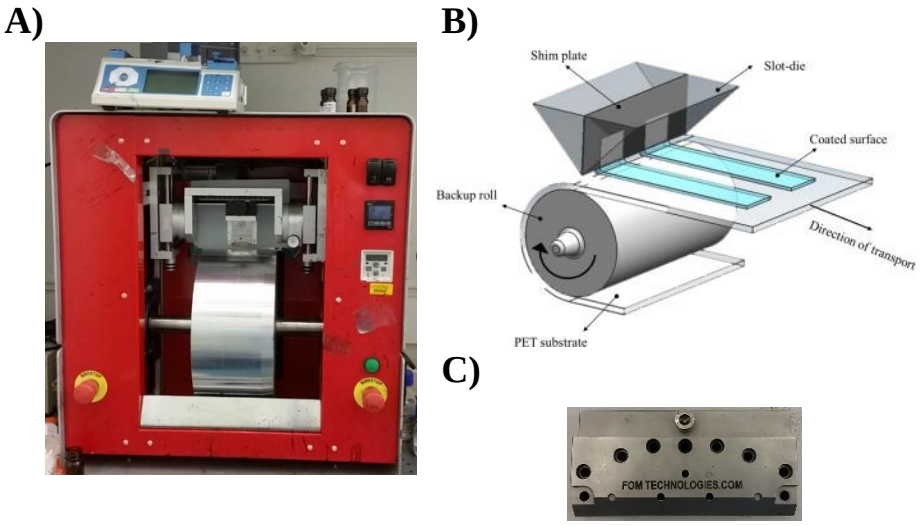

Fig. 2.13. A) Photograph of used Mini roll coater (MRC), B) slot-die coating process, C) Photograph of used printing head.

The MRC consists of an aluminium drum (diameter of 320 mm) in which it is possible to set the temperature. Generally, the drum gives a velocity of 0 to 2 m/min, while an ink flows from the coating head, forming the coated layer.

2.5.3 Thermal Evaporation

Thermal evaporation is one of the simplest among the Physical Vapor Deposition (PVD) techniques and is mainly used for deposition of metal oxide interlayers and metallic back electrodes.

Basically, materials are placed in a vacuum chamber and evaporated from crucibles by passing a current through a heating coil surrounding the crucible.

When the atoms at the surface of the material have a sufficient energy to leave the surface, they will travel across the vacuum chamber and coat a substrate positioned above the evaporating material (average working distances are 200 mm to 1 meter). The pressure in the chamber is typically ~10^{-4} Torr or lower in order to avoid oxidation of the source and collision among atoms and other particles in the chamber. In particular, the free path must be longer than the distance between evaporation source and the substrate, where the free path means the average distance that an atom or molecule can travel in a vacuum chamber before colliding.

A schematic representation of thermal evaporation mechanism is shown in Fig. 2.14.

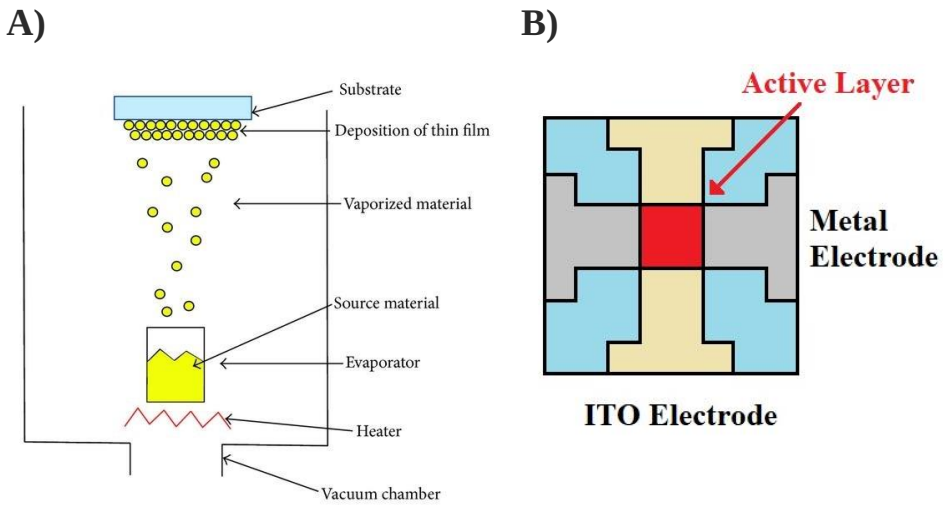

Fig. 2.14. A) Thermal evaporation process; B) Device geometry.

For the evaporation process, the use of masks is required because it allows to define the pattern of the substrate to cover in order to obtain the correct device geometry (Fig. 2.14 B).

The thickness of the deposited material is checked by a quartz crystal microbalance (QCM).

The instrument used in this work was Kurt J. Lesker MiniSpectros.

The main evaporation parameters are deposition rate, crucible material and final film thickness. In particular, the main used materials are reported in Tab. 2.1.

Tab. 2.1. Thermal evaporation parameters used in this work.

Material	Crucible Material	Film Thickness (nm)	Deposition Rate ($Å s^{-1}$)
Molybdenum Oxide (MoO_x)	Aluminium oxide (Al_2O_3)	5-10	0.5
Aluminium (Al)	Boron Nitride (BN) or TiB_2-BN	100-120	0.5
Silver (Ag)	Tungsten (W)	100	0.5

2.5.4 Characterization techniques

2.5.4.1 Current-Voltage characteristics

The most important characterization method for OPV is the measurement of the current-voltage characteristics (I-V curve), both in dark and under illumination.

This type of measurement should be carried out under real solar illumination or at a well-defined conditions that are correlated to the intensity and spectrum of the solar light which reaches the Earth.

Ideally, the spectrum of the solar radiation is close to black body but, actually, the amount that indeed reaches the Earth's surface depends on:

- Absorption and scattering phenomena of molecules forming the atmosphere. In particular, some wavelengths are strongly absorbed by atmospheric components, such as water vapour (H_2O), oxygen (O_2) and

carbon dioxide (CO_2) which are absorbing molecules in the visible and infrared regions while ozone (O_3) in the UV region;

- The sun inclination on the horizon.

For these reasons, the solar spectrum changes. Standard reference spectra, AM0 and AM1.5 (Fig. 2.15), are defined to allow the performance comparison of photovoltaic devices from different manufacturers and research laboratories. The syntax "AM" indicates the air coefficient mass and is given by the Eq. 2.7:

$$AM = \frac{1}{\cos(\theta)} \qquad Eq.2.7$$

where θ is the zenith angle of the sun.

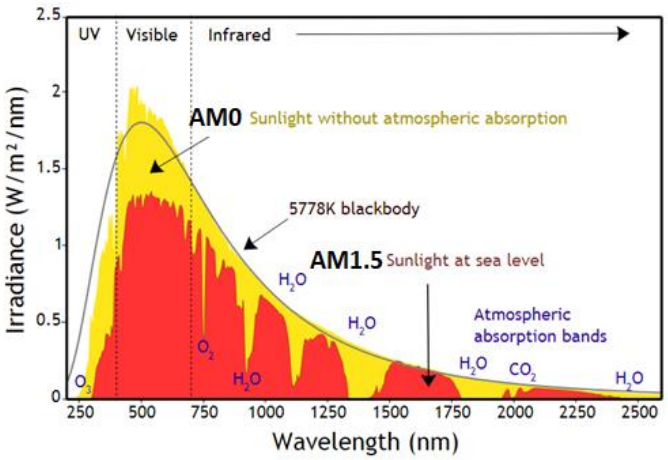

Fig. 2.15. The solar radiation spectrum for direct light at both the top of the Earth's atmosphere (AM0) and at sea level (AM1.5). These curves are based on the American Society for Testing and Materials (ASTM) Terrestrial Reference Spectra.

In this study, standard conditions used for solar cell characterization are the AM1.5G spectrum (1 Sun) with a fixed intensity of 100 $mWcm^{-2}$ and T = 25°C.

All I-V measurement of this study were carried out under nitrogen atmosphere (O_2 and H_2O < 1 ppm) and using a AAA class solar simulator from Photo Emission Tech, model CT100AAA, equipped with 150W Xenon Lamp whose intensity was calibrated using a mono-Si reference cell equipped with KG5 filter for 1 Sun intensity.

Generally, the current generated under illumination depends on illuminated area, A, hence, Current Density, J (mA cm^{-2}) is usually reported instead of Current I.

The basic current density–voltage characteristics (J–V curve) for a typical solar cell are shown in Fig. 2.16.

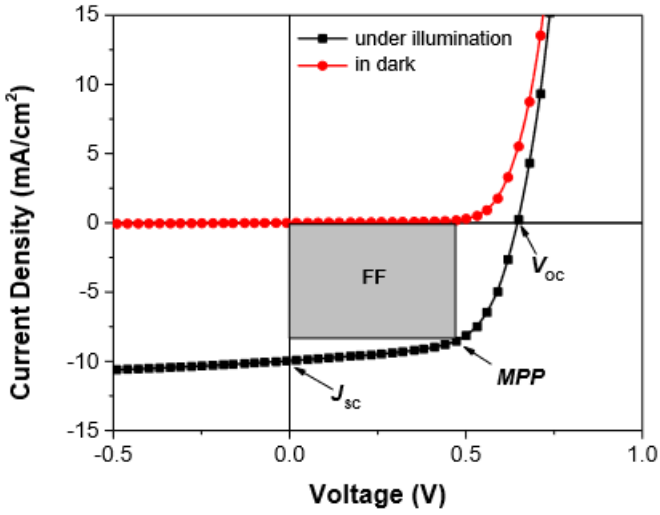

Fig. 2.16. J-V characteristics of a solar cell.

The J-V curve of the cell under illumination is a superposition of the dark J-V with the light generated current and the curve is shifted down to the 4th quadrant.

From J-V characteristics, various parameters can be determined such as open circuit voltage (V_{OC}), short circuit current (J_{SC}) and fill factor (FF).

Open-circuit Voltage (V_{OC}) is the maximum voltage available from a solar cell and this occurs at zero current. Its thermodynamic limit is given by the bandgap of the active materials. [79]

Short-circuit Current Density (J_{SC}) is the current through the solar cell when the voltage is zero on a given active area A. It represents the number of charge carriers that are generated and collected at the electrodes. Therefore, J_{SC} primarily depends on the property of the D and A materials, active layer morphology and the carrier mobility in the D and A phases.

Fill Factor (FF) is defined as a ratio between practical produced power and the theoretically possible (Eq. 2.8):

$$FF = \frac{I_{MPP} \cdot V_{MPP}}{I_{SC} \cdot V_{OC}} = \frac{J_{MPP} \cdot V_{MPP}}{J_{SC} \cdot V_{OC}} \qquad Eq.\,2.8$$

Where J_{MPP} and V_{MPP} are the current density and voltage at the point of maximum power output, respectively.

The FF is an indicator of the quality of a photovoltaic cell and it should be as high as possible. Its value can be significantly affected both by the ideality factor (n) of the cell, but also from its electrical resistances (series resistance, R_S, and shunt resistance, R_{sh}). In particular, the series resistance (R_S) includes all resistances at the interfaces between the layers, the conductivity of the semiconductors and the electrodes. It should be low for a good performing device. The shunt resistance (R_{sh}) needs to be high and includes all the current leakage through shunts as a result of defects in the layers.

All these parameters allow to calculate the most important benchmark value for solar cells, the power conversion efficiency (PCE). It is defined as the ratio between the maximum electrical power (I_{MPP}*V_{MPP}) of a cell and the power of the incident light (P_{in}), from the simulated AM1.5G solar spectrum, on a given active area A (Eq. 2.9):

$$PCE = \frac{P_{out}}{P_{in}} = \frac{I_{MPP} \cdot V_{MPP}}{P_{in} \cdot A} = FF \cdot \frac{I_{SC} \cdot V_{OC}}{P_{in} \cdot A} = FF \cdot \frac{J_{SC} \cdot V_{OC}}{P_{in}} \qquad Eq.\,2.9$$

2.5.4.2 External Quantum Efficiency

The quantum efficiency measurements give information on the current that a solar cell will produce when illuminated by a particular wavelength.
The "external quantum efficiency" (E.Q.E.) indicates the ratio of the number of carriers collected by the solar cell to the number of photons of a given energy incident on the solar cell. (Eq. 2.10)

$$EQE\ (\lambda) = \frac{(\frac{electrons}{s})}{(\frac{photons}{s})} \qquad Eq.\,2.10$$

An EQE of 100% means that for a given wavelength, all incident photons are converted to free charges and collected at the contacts.
An example of EQE curve for silicon (Si) solar cell is given in Fig. 2.17.

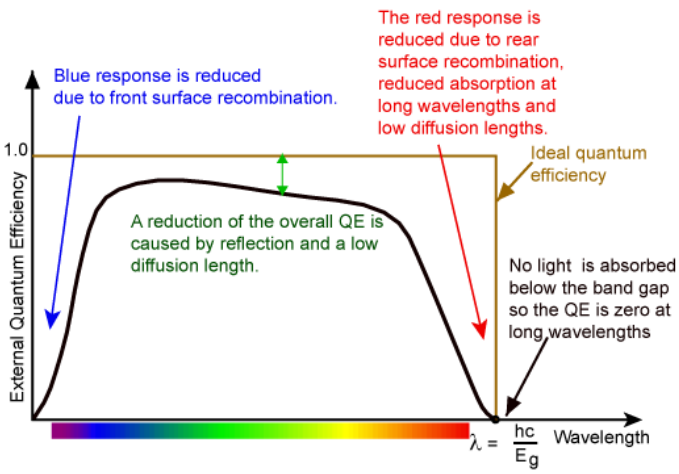

Fig.2.17. The external quantum efficiency (EQE) of a silicon (Si) solar cell.

There is a direct correlation between EQE and J-V measurements. In fact, it is possible to calculate the value of J_{SC} from EQE measurement and compare it to the value obtained by the cell measured by solar simulator, using the Eq. 2.11:

$$J_{SC} = \int_0^{\infty} eEQE(\lambda)\frac{\lambda}{hc}E_{\lambda}^{AM1.5G}(\lambda)d\lambda \qquad Eq.2.11$$

where $E_{\lambda}^{AM1.5G}$ is the spectral irradiance of the AM1.5G spectrum, λ is the wavelength, *h* is Planck's constant, *c* is the speed of light, and *e* is the elementary charge.

The EQE measurements reported in the present thesis were carried out using a Bentham PVE300 apparatus calibrated with a Si detector.

2.5.4.3 Absorbance spectroscopy

Absorbance spectroscopy was used to measure the transmission and reflectance of light at various wavelengths for different samples.

Basically, the total absorption of the stack is given by Eq. 2.12:

$$A = 1 - T - R \qquad Eq.2.12$$

Where T is the transmittance of the sample and R is its reflectance. Reflection-based experiment was performed using an integrating sphere as shown in Fig. 2.18.

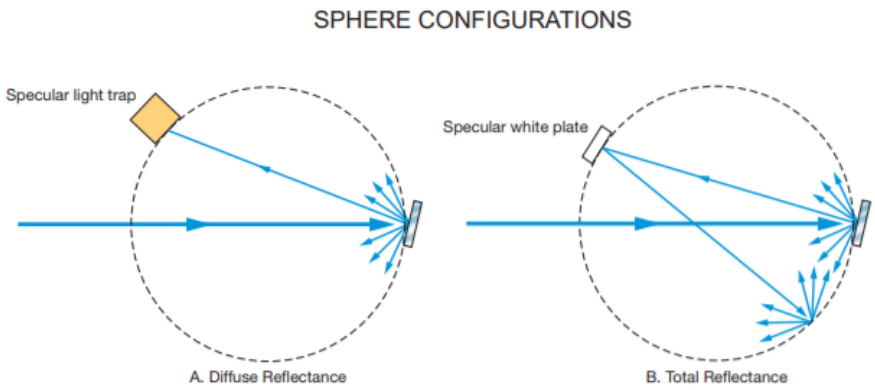

Fig. 2.18. Sampling configurations for diffuse and specular reflectance.

The UV-visible spectrophotometer used in this work (Perkin-Elmer Lambda 900 Spectrophotometer) is a double ray instrument and it is equipped with a deuterium and pre-aligned tungsten-halogen sources with a double monochromator.

2.5.4.4 Profilometry

Thickness is one of the most important film parameters, from which some properties of the material can depend.

The used technique to measure the thickness of the thin films is very simple. It consists of creating a neat step between the investigated materials

and the substrate and measurement of surface variation as shown in Fig. 2.19.

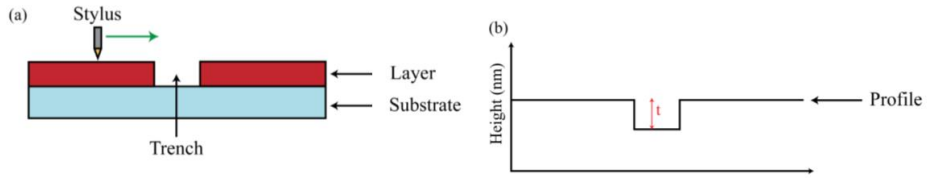

Fig. 2.19. a) Stylus moving linearly across layer surface. b) Measured height profile of sample with layer depth, t.

Basically, a diamond stylus is moved laterally along the sample for a specified distance and specified contact force. A typical profilometer can measure small vertical features ranging in height from 10 nanometers to 1 millimeter.

All thickness measurements were performed electromechanically by using a KLA Tencor P-10 model-Surface Profile Measuring System. KLA Tencor can provide height measurements with vertical resolution of 5 Å in a long lateral scan range of 50 μm to 30 mm, accuracy of 10 Å, 1σ step height repeatability, hence, enabling precise measurements of thin films thickness below 100 Å.

Bibliography of Chapter 2

[1] G. Chamberlain, *Sol. Cells,* vol. 8, pp. 47-83, 1983.

[2] C. W. Tang, *Applied Physics Letters,* vol. 48, pp. 183-185, 1986.

[3] G. Yu, J. Gao, J. C. Hummelen, F. Wudl and A. J. Heeger, *Science,* vol. 270, p. 1789, 1995.

[4] S. Li, Y. L., W. Zhao, H. Yan, B. Yang, D. Liu, W. Li, H. Ade and J. Hou, *J. Am. Chem. Soc. ,* vol. 140, p. 7159−7167, 2018.

[5] P. Kumaresan, S. Vegiraju, Y. Ezhumalai, S. L. Yau, C. Kim, W. H. Lee and M. C. Chen, *Polymers,* vol. 6, no. 10, pp. 2645-2669, 2014.

[6] R. Z. G. Li and Y. Yang, *Nature Photonics,* vol. 6, p. 153, 2012.

[7] O. V. Mikhnenko, P. W. M. Blom and T. Q. Nguyen, *Energy Environ. Sci.,* vol. 8, p. 1867, 2015.

[8] B. C. Thompson and J. M. J. Fréchet, *Angew. Chem. ,* vol. 47, no. 1, pp. 58-77, 2008.

[9] N. S. Sariciftci, L. Smilowitz, A. J. Heeger and F. Wudl, *Science,* vol. 258, no. 5087, p. 1474, 1992.

[10] A. A. Bakulin, D. S. Martyanov, D. Y. Paraschuk, M. S. Pshenichnikov and P. H. M. van Loosdrecht, *The Journal of Physical Chemistry B,* vol. 112, no. 44, p. 13730–13737, 2008.

[11] H. Kim and C. M. Gilmore, *J. Appl. Phys.,* vol. 86, no. 11, p. 6451, 1999.

[12] W. S. Jahng, H. A. Francis, H. Moon, J. I. Nanos and M. D. Curtis, *Appl. Phys. Lett.,* vol. 88, p. 093504, 2006.

[13] G. Li, V. Shrotriya, J. Huang, Y. Yao, T. Moriarty, K. Emery and Y. Yang, *Nat. Mater. ,* vol. 4, pp. 864-868, 2005.

[14] W. Ma, C. Yang, X. Gong, K. Lee and A. J. Heeger, *Advanced Functional Materials,* vol. 15, pp. 1617-1622, 2005.

[15] M. Jorgensen, J. Carle, R. Sondergaard, M. Lauritzen, N. Dagnaes-Hansen, S. Byskov, T. Andersen, T. Larsen-Olsen, A. Bottiger, B. Andreasen, L. Fu, L. Zuo, Y. Liu, E. Bundgaard, X. Zhan, H. Chen and F. C. Krebs, *Sol. Energy Mater. Sol. Cells* , vol. 119, pp. 84-93, 2013.

[16] K. H. Yim, Z. Zheng, R. H. Friend, W. T. S. Huck and J. S. Kim, *Adv. Funct. Mater.,* vol. 18, p. 2897–2904, 2008.

[17] E. Pavlopoulou, G. Fleury, D. Deribew, F. Cousin, M. Geoghegan and G. Hadziioannou, *Org. Electron.* , vol. 14, pp. 1249-1254, 2013.

[18] C. Waldauf, M. Morana, P. Denk, P. Schilinsky, K. Coakley, S. A. Choulis and C. L. Brabec, *Appl. Phys. Lett.,* vol. 89, p. 233517, 2006.

[19] T. Ameri, G. Dennler, C. Waldauf, P. Denk, K. Forberich, M. Scharber, C. Brabec and K. Hingerl, *J. Appl. Phys.* , vol. 103, p. 084506, 2008.

[20] J. Yuan, X. Huang, H. Dong, J. Lu, T. Yang, Y. Li, A. Gallagher and W. Ma, *Org. Electron.* , vol. 14, pp. 635-643, 2013.

[21] W. Tress, "Device Physics of Organic Solar Cells," Dresden, 2011.

[22] I. Litzov and C. J. Brabec, *Materials,* vol. 6, pp. 5796-5820, 2013.

[23] S. K. Hau, H. L. Yip, N. S. Baek, J. Zou, K. O'Malley and A. K. Y. Jen, *Appl. Phys. Lett.,* vol. 92, p. 253301, 2008.

[24] S. Schumann, R. D. Campo, B. Illy, A. C. Cruickshank, M. A. McLachlan, M. P. Ryan, D. J. Riley, D. W. McComb and T. S. Jones, *J. Mater. Chem.,* vol. 21, pp. 2381-2386, 2011.

[25] Z. Q. Liang, Q. F. Zhang, O. Wiranwetchayan, J. T. Xi, Z. Yang, K. Park, C. D. Li and G. Z. Cao, *Adv. Funct. Mater.,* vol. 22, pp. 2194-2201, 2012.

[26] F. C. Krebs, Polimeric Solar Cells: Materials, Design, Manufacture, Lancaster, PA (US) : DEStech Publications, 2010.

[27] A. K. K. Kyaw, X. W. Sun, C. Y. Jiang, G. Q. Lo, D. W. Zhao and D. L. Kwong, *Appl. Phys. Lett.* , vol. 93, p. 221107, 2008.

[28] Y. J. Kang, K. Lim, S. Jung, D. G. Kim, J. K. Kim, C. S. Kim, S. Kim and J. W. Kang, *Sol. Energy Mater. Sol. Cells*, vol. 96, pp. 137-140, 2012.

[29] M. A. Ibrahem, H. Y. Wei, M. H. Tsai, K. C. Ho, J. J. Shyue and C. W. Chu, *Sol. Energy Mater. Sol. Cells* , vol. 108, pp. 156-163, 2013.

[30] N. Sekine, C. H. Chou, W. L. Kwan and Y. Yang, *Org. Electron.*, vol. 10, pp. 1473-1477, 2009.

[31] H. Y. Park, D. Lim, K. D. Kim and S. Y. Jang, *J. Mater. Chem. A*, vol. 1, pp. 6327-6334, 2013.

[32] P. Morvillo, R. Diana, A. Mucci, E. Bobeico, R. Ricciardi and C.Minarini, *Solar Energy Materials and Solar Cells*, vol. 141, pp. 210-217, 2015.

[33] P. de Bruyn, D. J. D. Moet and P. W. M. Blom, *Org. Electron.*, vol. 11, pp. 1419-1422, 2010.

[34] S. K. Hau, H. L. Yip and A. K. Y. Jen, *Polym. Rev.* , vol. 50, pp. 474-510, 2010.

[35] C. Tao, S. Ruan, X. Zhang, G. Xie, L. Shen, X. Kong, W. Dong, C. Liu and W. Chen, *Appl. Phys. Lett.* , vol. 93, p. 193307, 2008.

[36] Y. Sun, C. J. Takacs, S. R. Cowan, J. H. Seo, X. Gong, A. Roy and A. J. Heeger, *Adv. Mater.* , vol. 23, pp. 2226-2230, 2011.

[37] C. Y. Jiang, X. W. Sun, D. W. Zhao, A. K. K. Kyaw and Y. N. Li, *Sol. Energy Mater. Sol. Cells* , vol. 94, pp. 1618-1621, 2010.

[38] V. Shrotriya, G. Li, Y. Yao, C. W. Chu and Y. Yang, *Appl. Phys. Lett.* , vol. 88, p. 073508, 2006.

[39] M. A. Khilla, Z. M. Hanafi, B. S. Farag and A. A.-e. Saud, *Thermochim. Acta,* vol. 54, pp. 35-45, 1982.

[40] M. Vasilopoulou, L. C. Palilis, D. G. Georgiadou, P. Argitis, S. Kennou, L. Sygellou, I. Kostis, G. Papadimitropoulos, N. Konofaos, A. A. Iliadis and D. Davazoglou, *Appl. Phys. Lett.*, vol. 98, p. 123301, 2011.

[41] T. He and J. Yao, *J. Photochem. Photobiol.,* vol. 4, pp. 125-143, 2003.

[42] N. K. Elumalai, A. Saha, C. Vijila, R. Jose, Z. Jieb and S. Ramakrishna, *Phys. Chem. Chem. Phys.*, vol. 15, pp. 6831-6841 , 2013.

[43] J. Subbiah, P. M. Beaujuge, K. R. Choudhury, S. Ellinger, J. R. Reynolds and F. So, *Org. Electron.*, vol. 11, pp. 955-958, 2010.

[44] Z. Yin, Q. Zheng, S. C. Chen and D. Cai, *ACS Appl. Mater. Interfaces* , vol. 5, pp. 9015-9025, 2013.

[45] S. Chambon, L. Derue, M. Lahaye, B. Pavageau, L. Hirsch and G. Wantz, *Materials* , vol. 5, pp. 2521-2536, 2012.

[46] A. Ng, X. Liu, C. H. To, A. B. Djurišić, J. A. Zapien and W. K. Chan, *ACS Appl. Mater. Interfaces,* vol. 5, pp. 4247-4259, 2013.

[47] Y. H. Kim, C. Sachse, M. L. Machala, C. May, L. M. Meskamp and K. Leo, *Adv. Funct. Mater.*, vol. 21, no. 6, p. 1076–1081, 2011.

[48] Q. Wei, M. Mukaida, Y. Naitoh and T. Ishida, *Adv. Mater.,* vol. 25, no. 20, pp. 2831-2836, 2013.

[49] A. M. Nardes, M. Kemerink, M. M. d. Kok, E. Vinken, K. Maturova and R. A. J. Janssen, *Org. Elect.* , vol. 9, no. 5, pp. 727-734, 2008.

[50] A. Elschner, S. Kirchmeyer, W. Lovenich, U. Merker and K. Reuter, PEDOT: principles and applications of an intrinsically conductive polymer, CRC Press, 2010.

[51] M. Kemerink, S. Timpanaro, M. M. de Kok, E. A. Meulenkamp and F. Touwslager, *J. Phys. Chem. B*, vol. 108, pp. 18820-18825, 2004.

[52] C. Ionescu-Zanetti, A. Mechler, S. Carter and R. Lal, *Adv. Mater.* , vol. 16, pp. 385-389, 2004.

[53] S. Lattante, *Electronics*, vol. 3, pp. 132-164, 2014.

[54] P. L. T. Boudreault, A. Najari and M. Leclerc, *Chemistry of Materials*, vol. 23, no. 3, pp. 456-469, 2011.

[55] M. C. Scharber, D. Mühlbacher, M. Koppe, P. Denk, C. Waldauf, A. J. Heeger and C. J. Brabec, *Adv. Mater. 2006, 18, 789– 794*, vol. 18, pp. 789-794, 2006.

[56] M. Berggren, G. Gustafsson, O. Inganäs, M. R. Andersson, O. Wennerström and T. Hjertberg, *Appl. Phys. Lett.* , vol. 65, p. 1489, 1994.

[57] H. Chan, *Prog. Polym. Sci.*, vol. 23, pp. 1167-231, 1998.

[58] W. Cai, X. Gong and Y. Cao, *Sol. Energy Mater. Sol. Cells*, vol. 94, pp. 114-127, 2010.

[59] J. Cremer, P. Bäuerie, M. M. Wienk and R. Janssen, *Chem. Mater.*, vol. 18, pp. 5832-5834, 2006.

[60] H. Kang, G. Kim, J. Kim, S. Kwon, H. Kim and K. Lee, *Adv. Mater.*, vol. 28, no. 36, pp. 7821-7861, 2016.

[61] C. Tanase, E. Meijer, P. Blom and D. Leeuw, *Phys. Rev. Lett.*, vol. 91, no. 21, p. 216601–1 – 216601–4., 2003.

[62] Y. Liang, Z. Xu., J. Xia, S. T. Tsai, Y. Wu, G. Li, C. Ray and L. Yu, *Adv. Mater.*, vol. 22, p. E135–E138, 2010.

[63] P. W. M. Blom, V. D. Mihailetchi, L. J. A. Koster and D. E. Markov, *Adv. Mater.* , vol. 19, pp. 1551-1566, 2007.

[64] Z. He, B. Xiao, F. Liu, Y. Yang, S. Xiao, C. Wang, T. P. Russell and Y. Cao, *Nat. Photonics*, vol. 9, pp. 174-179, 2015.

[65] Y. Kim, H. R. Yeom, J. Y., Kim and C. Yang, *Energy Environ. Sci.*, vol. 6, pp. 1909-1916, 2013.

[66] W. Zhao, D. Qian, S. Zhang, S. Li, O. Inganäs, F. Gao and J. Hou, *Adv. Mater.* , vol. 28, pp. 4734-4739, 2016.

[67] P. Sonar, J. P. F. Lim and K. L. Chan, *Energy & Environmental Sci.*, vol. 4, pp. 1558-1574, 2011.

[68] V. D. Mihailetchi, H. X. Xie, B. de Boer, L. J. A. Koster and P. W. M. Blom, *Adv. Funct. Mater.* , vol. 16, pp. 699-708, 2006.

[69] Y. He and Y. Li, *Phys. Chem. Chem. Phys.*, vol. 13, pp. 1970-1983, 2011.

[70] A. Wadsworth, M. Moser, A. Marks, M. S. Little, N. Gasparini, C. J. Brabec, D. Baran and I. McCulloch, "Critical review of the molecular design progress in non-fullerene electron acceptors towards commercially viable organic solar cells," *Chem Soc Rev,* 2018.

[71] Z. Zheng, O. M. Awartani, B. Gautam, D. Liu, Y. Qin, W. Li, A. Bataller, K. Gundogdu, H. Ade and J. Hou, *Adv. Mater.*, vol. 29, p. 1604241, 2017.

[72] D. Baran, R. S. Ashraf, D. A. Hanifi, M. Abdelsamie, N. Gasparini, J. A. Röhr, S. Holliday, A. Wadsworth, S. Lockett, M. Neophytou, C. J. M. Emmott, J. Nelson, C. J. Brabec, A. Amassian, A. Salleo, T. Kirchartz, J. R. Durrant and I. McCulloch, *Nat. Mater.,* vol. 16, p. 363–369, 2017.

[73] D. W. Schubert and T. Dunkel, *Materials Research Innovations* , vol. 7, p. 314, 2003.

[74] A. G. Emslie, F. T. Bonner and L. G. Peck, *J. Appl. Phys.*, vol. 29, p. 858, 1958.

[75] D. Meyerhofer, *J. Appl. Phys.*, vol. 49, p. 3993, 1978.

[76] L. Wengeler, M. Schmitt, K. Peters, P. Scharfer and W. Schabel, *Chem. Engin. Proc.: Proc. Intensif.*, vol. 68, pp. 38-44, 2013.

[77] F. C. Krebs, *Sol. Ener. Mater. Sol. Cells*, vol. 93, no. 4, pp. 394-412, 2009.

[78] R. Søndergaard, M. Hösel, D. Angmo, T. T. Larsen-Olsen and F. C. Krebs, *Mater. Tod.*, vol. 15, no. 1-2, pp. 36-49, 2012.

[79] C. Winder and N. S. Sariciftci, *J. Mater. Chem.*, vol. 14, pp. 1077-1086, 2004.

CHAPTER 3

Organic Photovoltaics (OPV): Experimental section

3.1 Introduction

The main challenge of PSC technology for the commercialization is to overcome thermal instability of organic solar cells in order to produce devices with industrially scalable printing technologies (i.e. high throughput roll-to-roll process) since different heating steps at high temperature to dry the printed layers are usually required [1] Therefore, the thermal degradation is a critical aspect for the PSC production. In fact, each layer constituting the solar cell can affect the overall stability performance of the final device. [2, 3, 4]

According to these considerations, the aim of the research activity was the study of different materials (i.e. active layer materials, interlayer materials and metallic inks) and their properties for the realization of PSCs. The following aspects were considered:

- ✓ the optimization of device structure to achieve the best electrical performance;
- ✓ the impact of material thermal behavior on the device performance;
- ✓ the compatibility with printing techniques under different operating conditions.

3.2 Fullerene-based polymer solar cells

This section presents the results of the study carried out on polymer solar cells based on the blend PTB7-Th:[70]PCBM.

As discussed in Chapter 2, PTB7-Th is an analogue of PTB7 but with two 2-ethylhexyl-thienyl groups pendant off the benzodithiophene backbone unit. It is a highly efficient and low band-gap donor polymer (E_g ~ 1.6 eV).

This material has several advantages but, also, some important drawbacks. In fact, solar cells based on PTB7-like and fullerene are generally known to be thermal unstable due to deterioration of the blend morphology at high temperatures. [5, 6] Nevertheless, it was demonstrated that this type of polymer can be considered a promising material thanks to the possibility of processing under ambient conditions using roll-to-roll or compatible production methods. [7]

The approach of this work was to perform a systematic comparison of solar cells fabricated by means of different coating and printing techniques, i.e. spin-coating *vs*. screen printing and under various environmental conditions such as nitrogen *vs.* air, and, at the same time, to study their thermal stability.

3.2.1 Device preparation

PSC devices were fabricated using the inverted architecture because this configuration is more stable under ambient conditions and more suitable for large-scale printing process [8, 9, 10, 11]. In particular, it consists of:

ITO/ZnO/PTB7-Th:[70]PCBM (1:1.5 w/w) /MoO_x/Ag

The BHJ architecture and the energy diagram, showing the highest occupied molecular orbital (HOMO) and lowest unoccupied molecular orbital (LUMO) energy levels for different device components, are reported in Fig. 3.1.

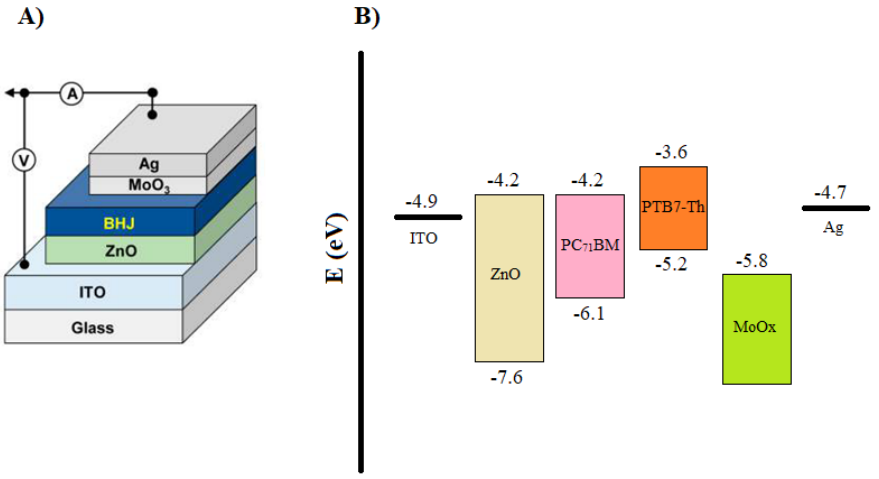

Fig. 3.1. A) Device architecture; B) Energy level diagram.

The materials used in this thesis are commercially available. PTB7-Th donor material (M_n > 25000 Da, PDI= 1.8-2.2) was purchased from Solarmer Materials Inc and the fullerene derivative [70]PCBM from Solenne B.V.

The devices were fabricated using the following methods. Firstly, pre-patterned ITO substrates were throughly cleaned as described in Chapter 2 and subjected to UV-Ozone treatment to remove further organic residues and to improve surface hydrophilicity. Then, a 40 nm ZnO layer (ETL), produced by sol-gel method, was spin-cast in air at 4000 rpm for 60 s onto the substrates, and was subsequently annealed on a hot plate in air for 5 minutes at 150°C. The active layer ([PTB7-Th] = 15 mg mL^{-1}) was then spin-cast in the glovebox and subjected to methanol wash. Finally, a top anode consisting of a MoO_x/Ag film (5/100 nm) was

deposited onto the active layer *via* thermal evaporation at a pressure roughly ~ 10^{-7} mbar in a vacuum evaporation chamber.

A set of four devices was fabricated for each type of studied sample. The device area was 0.2025 cm^2. All the devices were characterized by UV-VIS spectroscopy, J-V measurements under simulated AM1.5G solar irradiation (100 mW cm^{-2}) and quantum efficiency measurements (EQE).

3.2.2 Characterization

I) Optimization of inverted PSC

In order to optimize the device structure, the physical features of active layer, such as thickness and thermal annealing conditions, were studied.

It is known that the performances of PSC are highly sensitive to active layer (AL) thickness variations. [12] For this reason, the optimization process of AL thickness is an important step in order to achieve a good compromise between strong light absorption and efficient charge carrier collection. In particular, the optimal thickness strictly depends on the interference effects occurring in the thin film multilayer device [13] and can be also affected by the use of optical spacers. [14, 15] In the case of low thicknesses, electrical losses can be considered constant.

The UV-Vis absorption spectra of PTB7-Th:[70]PCBM blend layer with different thicknesses (*t*) are reported in Fig. 3.2.

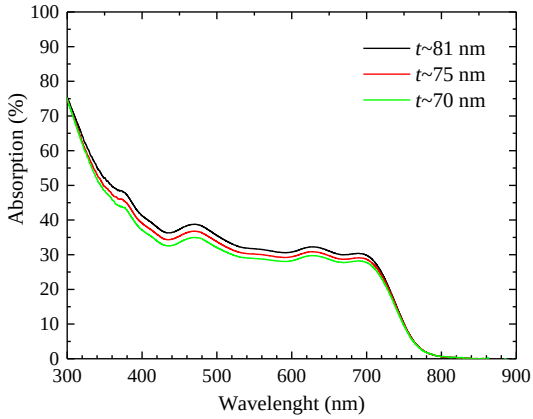

Fig. 3.2. Absorption spectra of PTB7-Th:[70]PCBM blend with different thicknesses.

The tests were performed by varying the spin speed obtaining thin film thicknesses included in a rather small range (70 nm <*t*< 81 nm).

The blend spectra show a broad absorption from 300 nm to 750 nm. The absorption between 550 nm and 750 nm is mainly due to the PTB7-Th, while its relatively weak absorption from 300 nm to 500 nm is compensated by the acceptor component [70]PCBM.

Fig. 3.3 shows the typical J-V characteristics under illuminated conditions and EQE curves of devices fabricated using the different thicknesses.

Tab. 3.1 summarizes the photovoltaics parameters for the devices.

A

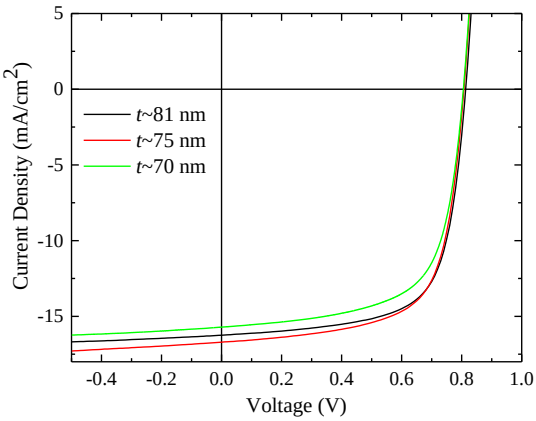

B

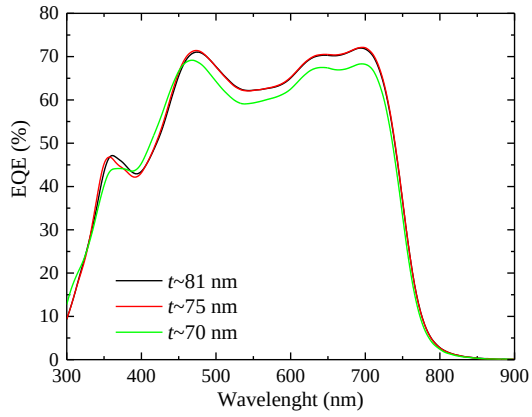

Fig. 3.3. Devices fabricated varying the active layer thickness: A) J-V light characteristics; B) EQE spectra.

Tab. 3.1. J-V light values of the devices realized varying the active layer thickness.

Blend Thickness (t)	**PCE (%)**	**FF (%)**	**J_{SC} (mA/cm^2)**	**V_{OC} (mV)**	**R_S (Ohm*cm^2)**	**R_{sh} (Ohm*cm^2)**
70 nm	8.42	65.7	15.9 (15.1)	805	4.3	7E2
75 nm	9.17	68.2	16.8 (15.9)	811	3.7	7.5E2
81 nm	9.09	68.5	16.2 (15.7)	813	3.9	9E2

The J_{SC} values in brackets were obtained by the EQE measurements.

As shown in Tab. 3.1, the best device performances were obtained by using an active layer of 75 nm exhibiting a J_{SC} values of 16.8 mA/cm^2, a high V_{OC} of 811 mV, and FF of about 68%, leading to a maximum PCE of 9.17 %.

Note that, the performance of PTB7-Th:[70]PCBM solar cells are strongly dependent on the processing conditions and on the blend morphology. Therefore, in order to increase the nanoscale phase separation, the addition of chemical additives in the blend solution, such as 1,8 diiodoctane (DIO), is request. [16]. It is known that these solvent additives are generally small molecules, which selectively dissolve the fullerene preventing aggregation and allow to obtain an optimal interpenetrating network-type morphology of the active layer. [17] At the same time, it has been demonstrated that some additive residues remain in the organic layer of the fabricated devices due to their low volatility and, thus, could be detrimental for the devices performance, i.e., limiting their lifetime and leading to photodegradation when exposed to simulated sunlight in ambient conditions. [18, 19] Therefore, the most favorable strategy, also used in the present thesis work, to tackle this problem is the *methanol treatment* that removes the residual additives and improves the morphological stability enhancing the efficiency of PSCs. [20, 21, 22, 23]

In order to evaluate the real contribution of the blend to the J_{SC}, it was measured the external quantum efficiency (EQE) (Fig. 3.8B) obtaining that the integrated EQE for these devices matches the measured short circuit current with a margin of about 5%. The maximum values of EQE are in the range 450-500 nm (~70%) and in the range 600-750 nm (achieving 72%).

In order to understand the influence of temperature on the active layer, the thermal tests were carried out under inert atmosphere.

The temperatures (T) of the tests were fixed at

- 80°C
- 100°C
- 140°C

In particular, T=80°C was chosen because it represents the operating temperature to test the device functioning for the outdoor applications since solar panels usually reach temperatures as high as 65-85°C. [24] In addition, higher temperatures were also evaluated with the purpose of determining the thermal stability threshold of the active layer to prevent fullerene aggregation.

The PV performances were checked after 5 minutes. The annealed devices were characterized and compared with the untreated ones (Fig. 3.4).

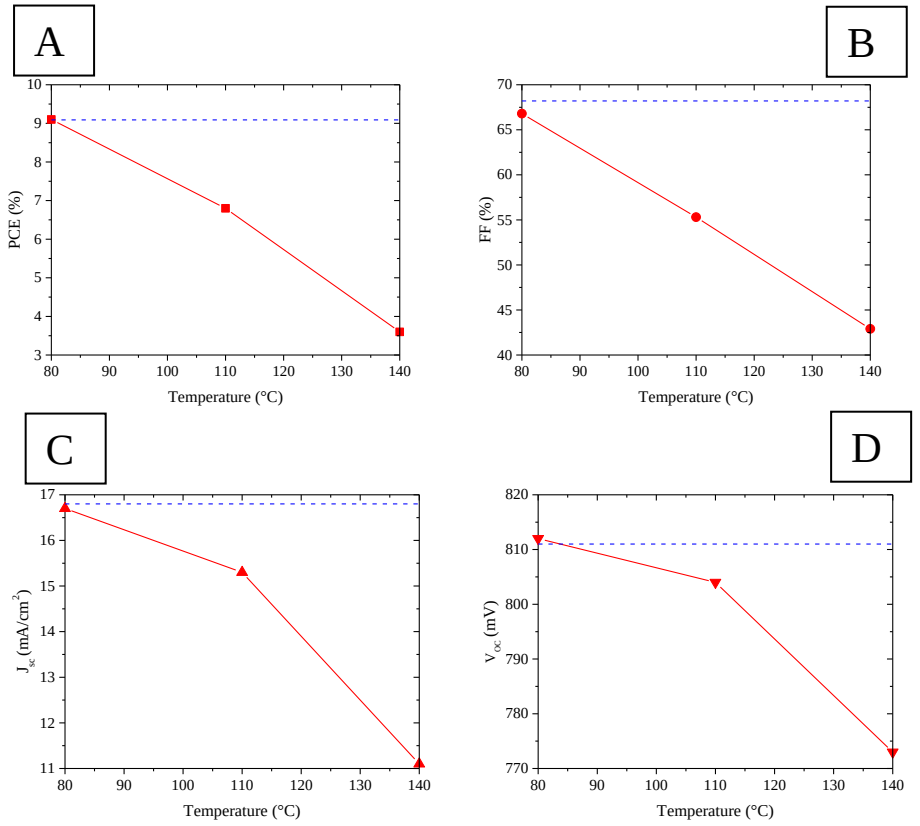

Fig. 3.4 Annealing temperature dependences of (A) PCE, (B) FF, (C) J_{SC} and (D) V_{OC} of the PTB7-Th:[70]PCBM bulk heterojunction photocells. Horizontal lines denote the relevant values of PCE (A), FF (B), J_{SC} (C) and V_{OC} (D) for the as prepared device with an active layer of 75 nm, not subjected at thermal annealing.

The performances of the device with the active layer annealed at 80°C, remain substantially unchanged. This means that the organic layer morphology can be considered thermal stable at this condition and, for this reason, this temperature was selected for the following working steps. On the contrary, higher temperatures induced a serious degradation for all PV parameters. It is known, in fact, that PTB7-like polymer and [70]PCBM deteriorate upon thermal annealing due to irreversible aggregation of fullerene [25] resulting in a variation of the charge percolation nanostructures.

II) Incorporation of solution-processed HTL

One of the key points of the present research activity was the substitution of the evaporated materials, such as hole transport layer (HTL) and metals, with solution-processed alternatives compatible with printing techniques. This is an important step for roll-to roll (R2R) production, to fabricate on large area and with low costs.

OPV devices were fabricated replacing MoO_x (HTL) in inverted configuration (ITO/ZnO/active layer/HTL/Ag) with solution-processed poly(3,4-ethylenedioxythiophene):polystyrene sulfonate, (PEDOT:PSS). As discussed in Chapter 2, this material combines several characteristics that are desirable for OPV applications, including good conductivity and high film transparency. In Fig. 3.5 is reported its reflectance and transmittance spectra (film deposited on a glass substrate).

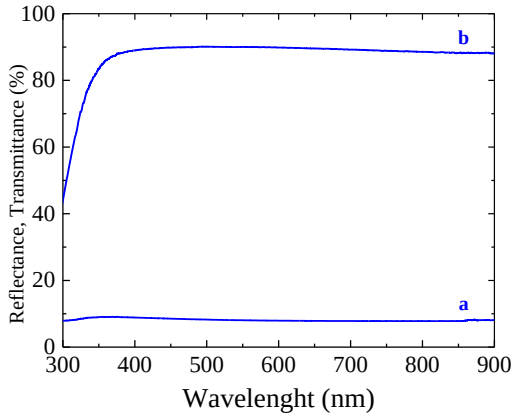

Fig. 3.5. Reflectance (a) and transmittance (b) spectra of PEDOT:PSS deposited on a glass substrate.

The optimal conditions for producing the PEDOT:PSS thin films were obtained by scanning their chemical and physical features such as composition, thickness and thermal annealing conditions. In particular, PEDOT:PSS solution was prepared by mixing PEDOT:PSS (Clevios P

VP Al4083) and additives such as isopropyl alcohol (IPA) and Zonyl FS-300 surfactant in order to increase the wettability on hydrophobic active layer surface (Fig. 3.6).

Fig. 3.6. A) The wettability of PEDOT:PSS on hydrophobic surface; B) The wettability of PEDOT:PSS with additives on hydrophobic surface.

For HTL fabrication, the compositions used are:

A) PEDOT:PSS mixed to isopropyl alcohol (IPA) (1:1) with 0.05 wt% Zonyl FS-300 (fluorosurfactant);
B) PEDOT:PSS mixed to IPA (1:1) with 0.11 wt% Zonyl FS-300
C) PEDOT:PSS mixed to IPA (1:1) with 0.22 wt% Zonyl FS-300
D) PEDOT:PSS mixed to IPA (1:2) with 0.22 wt% Zonyl FS-300

The thin films were obtained by spin coating technique with a spin speed of 5000 rpm for 60 s (t~52 nm) and annealed at T=80°C for 10 minutes in air, instead of the standard temperature of 120°C, in order to avoid fullerene aggregation in the underlying active layer.

The J–V characteristics under illumination of solar cells and the corresponding EQE curve using different PEDOT:PSS compositions are shown in Fig. 3.7.

The photovoltaic device parameters are further summarized in Tab. 3.2.

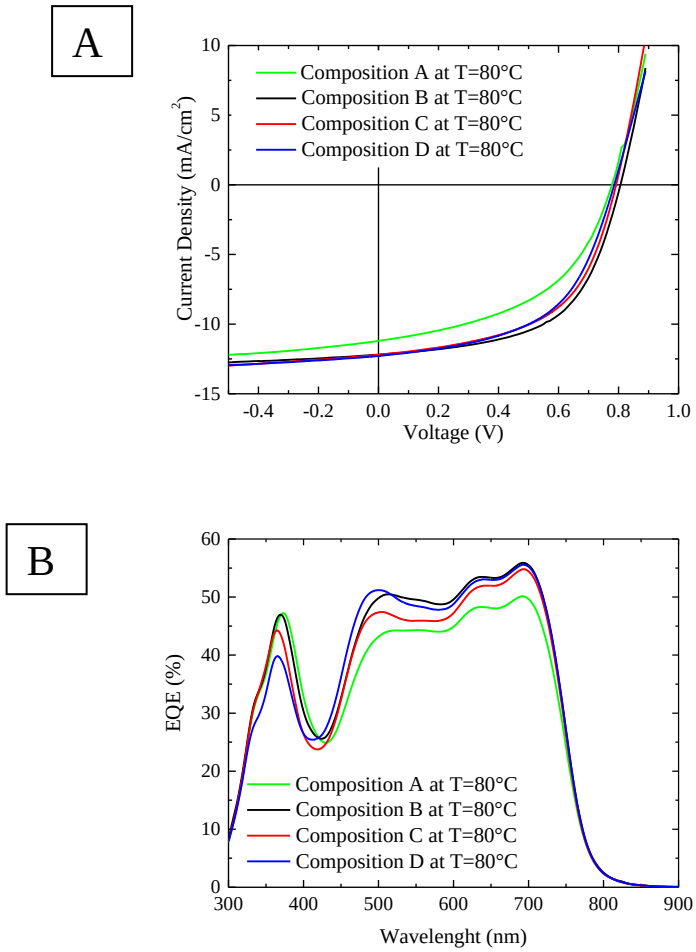

Fig. 3.7. Devices fabricated varying PEDOT:PSS composition: A) J-V light characteristics; B) EQE spectra.

Tab. 3.2. J-V light values of the devices realized varying PEDOT:PSS composition

Composition	PCE (%)	FF (%)	J_{SC} (mA/cm^2)	V_{OC} (mV)	R_S (Ω*cm^2)	R_{sh} (Ω*cm^2)
A	4.23	48.4	11.2 (10.5)	778	15	3E2
B	5.63	57.0	12.2 (11.6)	806	12	7.4E2
C	5.32	54.7	12.2 (11.1)	792	11	4.3E2
D	5.25	53.9	12.3 (11.5)	786	14	4.6E2

The J_{SC} values in brackets were obtained by the EQE measurements.

The introduction of solution-processed HTL, instead of evaporated MoO_x, led to significant but not drastic losses in the PCE (for the best PEDOT:PSS composition "B" the reduction is roughly 38%). The main parameters affected by solution processing were the FF and the J_{SC} while the V_{OC} slightly decay. It is reasonable to suppose that this is also due to the highly hygroscopic nature of PEDOT:PSS. In fact, oxygen and water could be absorbed during the device fabrication involving reactions at interfaces with electrodes that consequently affect the overall PV performance. [26]

These considerations about the reduction of J_{SC} values are also consistent with data analysis of EQE measurements.

After the optimization of the composition, the influence of PEDOT:PSS thickness on the device performances was studied. In order to prepare films with different thickness, 3 spin rates were chosen:

- 1000 rpm (*t*~ 66 nm)
- 3000 rpm (*t*~ 61 nm)
- 5000 rpm (*t*~ 52 nm)

Fig. 3.8 shows J–V light characteristics and EQE curves obtained from fabricated devices.

The corresponding PV values are reported in Table 3.3.

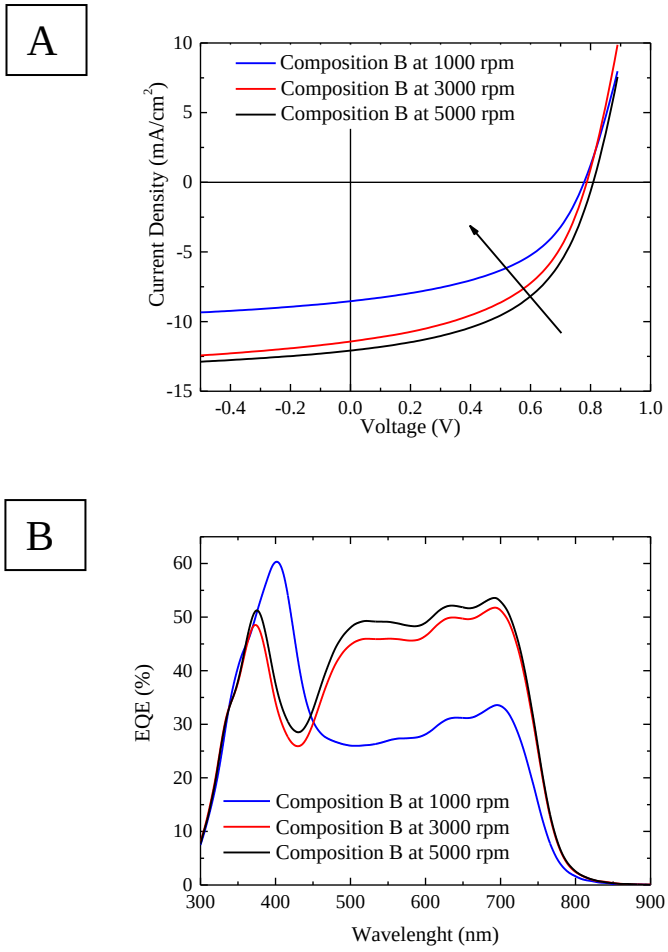

Fig. 3.8. Devices fabricated with different PEDOT:PSS thickness: A) J-V light characteristics; B) EQE spectra.

Tab. 3.3. J-V light values of the devices realized with different PEDOT:PSS thickness.

PEDOT:PSS Spin speed (rpm)	**PCE (%)**	**FF (%)**	**J_{SC} (mA/cm^2)**	**V_{OC} (mV)**	**R_S (Ω*cm^2)**	**R_{sh} (Ω*cm^2)**
1000	3.25	48.4	8.5 (7.6)	778	19	4.1E2
3000	4.41	49.0	11.4 (10.8)	787	14	3.5E2
5000	4.95	50.6	12.1 (11.4)	809	14	4.2E2

The J_{SC} values in brackets were obtained by the EQE measurements.

Various thicknesses of PEDOT:PSS were tested (from 52 to 66 nm) and the thinner layer achieved a sufficiently good electrical performance. In particular, it was confirmed that the overall reduction in PCE was dominated by the reduction in FF and J_{SC} with the V_{OC} only undergoing a relatively small reduction, while the PV parameters of devices based on thicker HTL layer significantly degraded.

In summary, the optimized conditions for solution-processed PEDOT:PSS layer were:

- ✓ Composition B: PEDOT:PSS/IPA (1:1)+ 0.11 wt% Zonyl FS-300
- ✓ 80°C for 10’ in air
- ✓ Spin speed: 5000 rpm (*t*~ 50 nm)

In general, the power conversion efficiency (PCE) of the devices so realized was around 5%.

III) Incorporation of screen-printed Ag back electrode

According to reported results, a comparative study of the photovoltaic behavior of PSCs (with solution-processed PEDOT:PSS as HTL) built up

using Ag back electrodes made via thermal evaporation under high vacuum (10^{-7} mbar) and by screen-printing using a commercially Ag paste (heat cured at T=80°C) was made.

The IV light and EQE curves are shown in Fig. 3.9 and the best data are summarized in Tab.3.4.

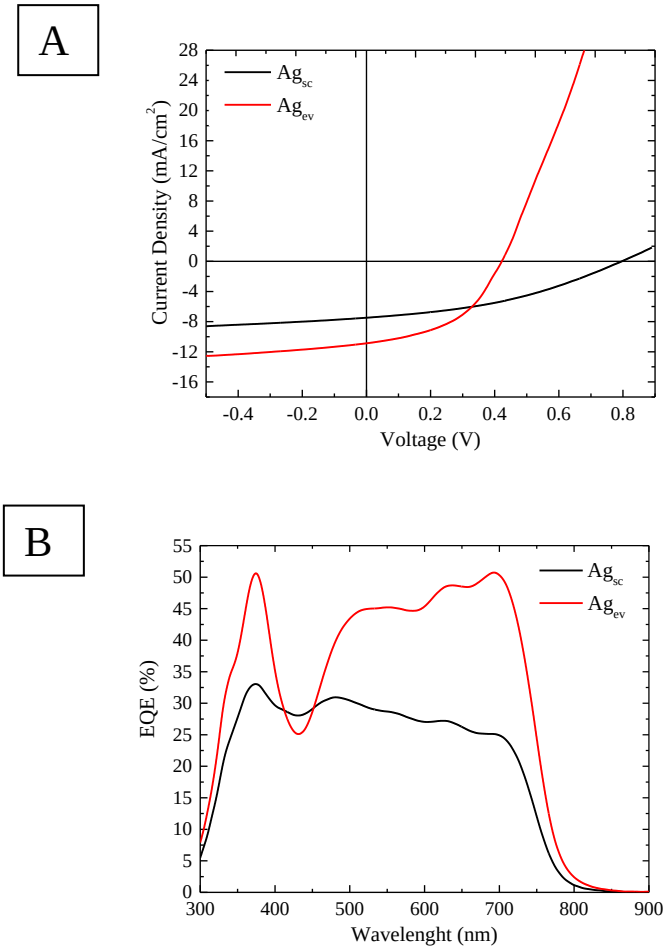

Fig. 3.9. Devices fabricated varying back electrode deposition technique (evaporation, ev, and screen printing, sc): A) J-V light characteristics; B) EQE spectra.

Tab.3.4. JV light values of the devices realized varying back electrode deposition technique (evaporation, ev, and screen printing, sc).

Back electrode deposition	**PCE (%)**	**FF (%)**	**J_{SC} (mA/cm^2)**	**V_{OC} (mV)**	**R_S ($\Omega*cm^2$)**	**R_{sh} ($\Omega*cm^2$)**
Ag_{ev}	4.26	47.6	11.8	762	16	3E2
Ag_{sc}	2.29	38.2	7.5	796	53	3.2E2

This study highlighted a reduction and rapid deterioration of the electrical performances for devices made with screen-printed Ag. Note that there was a considerable increase of R_S, whose value, as it is known, is associated with the general stack architecture and contact resistances. Therefore, a plausible explanation could be that the curing temperature (T=80°C) of Ag paste is too low and, therefore, the solvents, contained in this ink, are trapped in the layer and, then, leak in and partly dissolves the underlying active layer destroying the morphology of the bulk heterojunction.

3.3 Non Fullerene-based polymer solar cells

In the previous section, it was demonstrated that the thermal stability of fullerene-based solar cells is strictly related to the thermal behavior of the active layer. The main key factor in limiting the efficiency usually is the modification of the blend morphology. In fact, it is known that the thermal annealing at high temperature leads to reduction of interfacial area between donor and acceptor and, consequently, reduction of the

charge separation and charge collection efficiencies due to irreversible aggregation of fullerene. [25]

Other crucial aspects, that influenced the thermal behavior of investigated devices, were the stability of the adjacent layers, such as HTL and metal back electrode, and the interactions occurring at their interface.

These aspects played a fundamental role in dictating the low device performance and for these reasons, the present activity was subsequently focused on a more thermal stable and attractive active layer based a wide band gap donor polymer, PBDB-T, and small molecular compound, ITIC. Zhao et al. [27] demonstrated that PBDB-T:ITIC blend is a promising optical and electrical combination. In particular, the single component absorption spectra present a good complementarity ensuring, thus, an optimal coverage of the solar spectrum.

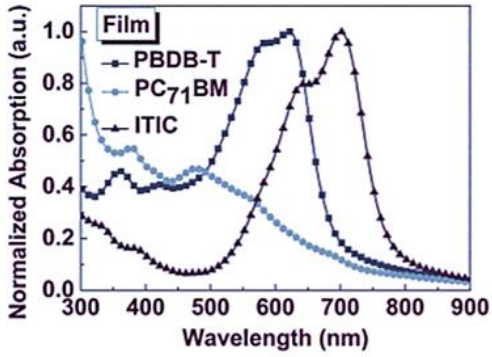

Fig. 3.10. Normalized absorption spectra of the PBDB-T, ITIC and [70]PCBM. [27]

It can see in the Fig. 3.10 that the PBDB-T film substantially overlaps that of the [70]PCBM in the visible range with the maximum value ~ 620 nm while it is complementary with that of ITIC. It means that a potential photon harvesting enhancement can occur leading to a significant improvement of J_{SC}.

PBDB-T:ITIC-based device showed an excellent electrical performance exceeding the PCE barrier of 11%. The authors investigated the effect of different annealing temperatures on the active layer and compared the so obtained PCE values to those of PBDB-T: [70]PCBM based PSCs.

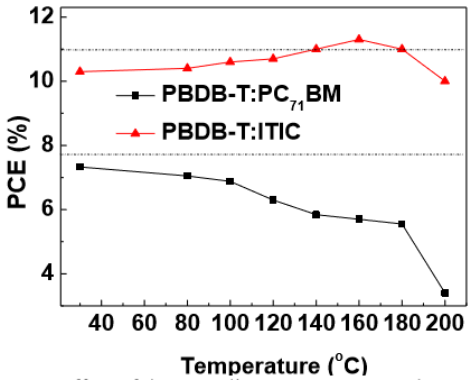

Fig. 3.11. Effect of the annealing temperature on the PCE of the PBDB-T:ITIC and PBDB-T:[70]PCBM based PSCs. [27]

As shown in Fig. 3.11, for the non fullerene-based solar cell the best performance was achieved when the active layer was annealed at 160°C for 30 minutes while a significant degradation occurred for PBDB-T:[70]PCBM based PSCs.

In addition, the impressive long-term stability was demonstrated. In fact, the PBDB-T:ITIC-based device, annealed under 100 °C for 250 h, still showed a PCE of 10.8%.

In general, the combination between wide bandgap polymer donor and narrow band gap non fullerene acceptors is particularly interesting because it potentially also provides an effective approach to improve the V_{OC} and to have a high value of J_{SC}. [28, 29, 30]

This section presents the results of the study carried out on polymer solar cells based on the blend PBDB-T:ITIC (1:1 w/w).

3.3.1 Device Preparation

The devices were realized with inverted configuration:

ITO/ZnO/ PBDB-T:ITIC (1:1 w/w) /MoO_x/Ag

The BHJ architecture and the energy diagram are reported in Fig. 3.12.

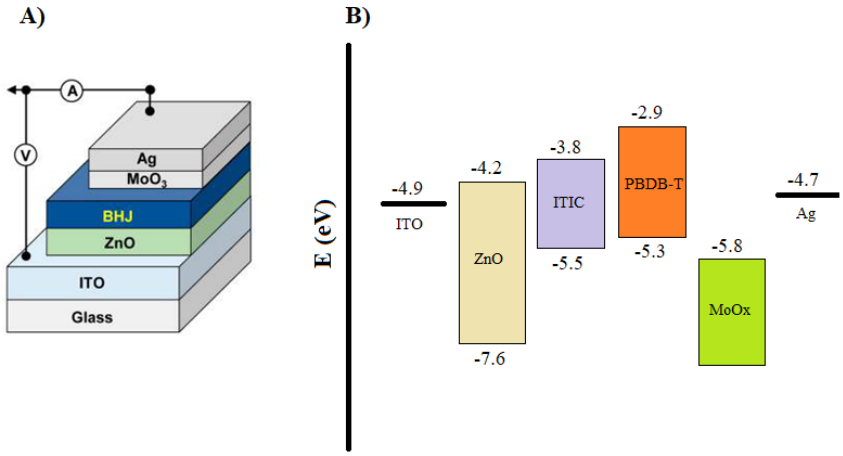

Fig. 3.12. A) Device architecture; B) Energy level diagram.

PBDB-T donor material (M_n > 100000 Da, PDI < 3) and ITIC acceptor were purchased from 1-Material.

The devices were fabricated as described in the Section 3.2.1. The active layer was spin coated under inert conditions using a chlorobenzene blend solution ([PBDB-T] = 10 mg/mL) with a weight ratio between PBDB-T:ITIC of 1:1, adding 0.5 vol% of 1,8 DIO and thermal annealed at 160°C for 30 minutes.

All the devices were characterized by UV-VIS spectroscopy, J-V measurements under simulated AM1.5G solar irradiation (100 mW cm^{-2}) and quantum efficiency measurements (EQE).

3.3.2 Characterization

I) Optimization of inverted PSC

In this study, a careful analysis of active layer characteristics was carried out focusing on the choice of a suitable layer thickness in order to optimize the device performance.

The UV-Vis absorption spectra of PBDB-T:ITIC thin films with different thicknesses coated on glass substrates are reported in Fig. 3.13.

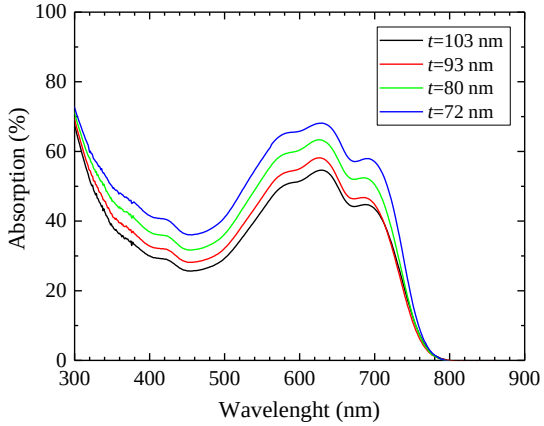

Fig.3.13. Absorption spectra of PBDB-T:ITIC blend with different thicknesses.

It is possible to observe a broad absorption from 300 nm to 750 nm. The polymer contribution is evident between 480 nm and 650 nm, while the absorption at longer wavelengths (from 600 nm to 750 nm) is due to the presence of ITIC.

Fig. 3.14 shows J–V characteristics under illuminated conditions and EQE curves obtained from devices with different active layer thickness.

The corresponding J-V parameters are reported in Tab. 3.5.

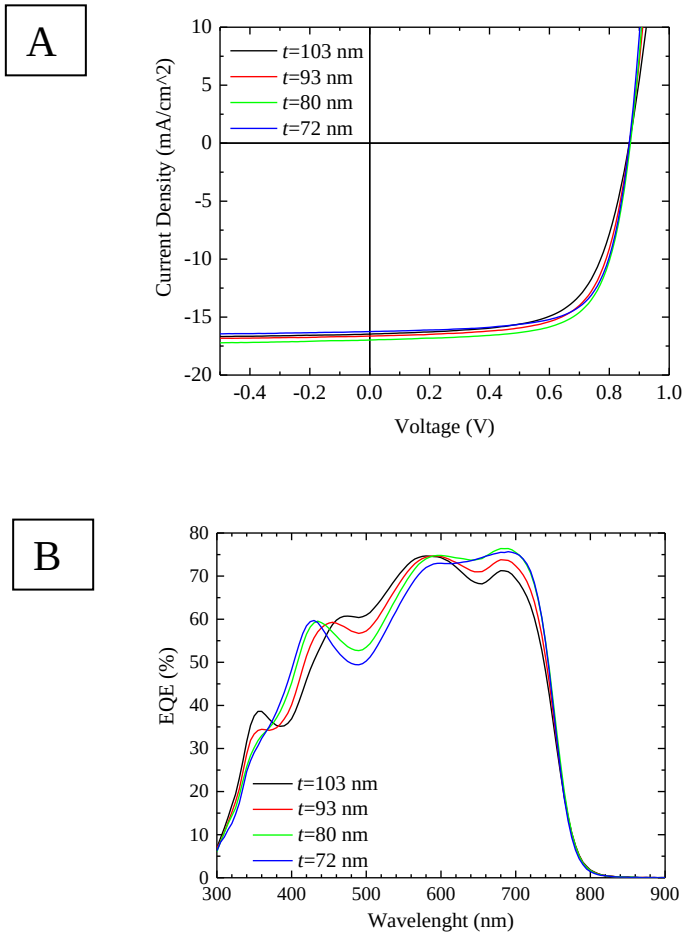

Fig. 3.14. Devices fabricated varying active layer thicknesses: A) J-V light characteristics; B) EQE spectra.

Tab. 3.5. J-V light values of the devices realized varying the active layer thickness.

Active layer Thickness (nm)	**PCE (%)**	**FF (%)**	**J_{SC} (mA/cm^2)**	**V_{OC} (mV)**	**R_S (Ohm*cm^2)**	**R_{sh} (Ohm*cm^2)**
t=72	10.0	70.2	16.5 (15.6)	866	4.5	1.3E3
t=80	10.2	69.2	17.0 (15.9)	870	4.3	1.3E3
t=93	9.9	68.2	16.8 (15.8)	867	5.4	1.4E3
t=103	9.4	65.2	16.7 (15.6)	867	6.7	1.3E3

The J_{SC} values in brackets were obtained by the EQE measurements.

The record PSC device (active layer thickness of 100 nm) reported in literature [27] was characterized by a PCE = 11.21%, V_{OC} = 899 V, J_{SC} =16.81 mA/cm^2 and FF=74.2 %.

The efficiency of PBDB-T:ITIC-based solar cells fabricated in this research activity achieved as best result a PCE~10.2 % with lower values of FF and V_{OC} while the J_{OC} was substantially the same. Note that these performances were obtained by devices with an active layer thickness of ~ 80 nm. These results are probably due to the different experiment conditions and material sources.

The EQE graph highlights a broad response to sunlight in the range of blend absorption with maximum value of 76.4% at 690 nm, comparable to state of art.

The reported performance was obtained by the BHJ solar cells fabricated in an inverted configuration with evaporated MoO_x as HTL and Ag as top electrode.

Generally, the use of Ag as anode is preferable, since air exposure allows the formation of silver oxide species (Ag_2O) characterized by a higher work function and, thus, an improvement of hole collection. [31]

According to the motivation of present work, that is, to realize efficient and stable inverted PSCs, an important issue is to study the impact of thermal annealing on the whole device.

As discussed in Chapter 2, it is known that the post-processing thermal annealing on the device is harmful for the electrical performance when MoO_x is used as the HTL due to evolution of the layer into an alloy of silver and molybdenum oxide after the diffusion of silver ions and oxygen inside the active layer. [32]

For this reason, various top electrode combinations were tested investigating the influence of another metal anode (Aluminium, Al, 100 nm) with different thicknesses of MoO_x as buffer layer (5 or 10 nm).

OPV devices have been fabricated using this inverted architecture:

- ITO/ZnO/ PBDB-T:ITIC (1:1 w/w) / MoO_x (5 nm)/Al
- ITO/ZnO/ PBDB-T:ITIC (1:1 w/w) / MoO_x (10 nm)/Al
- ITO/ZnO/ PBDB-T:ITIC (1:1 w/w) / MoO_x (5 nm)/Ag as control device

The J-V and EQE curves of so fabricated devices and of the control device are shown in Fig. 3.15. The electrical properties are reported in Tab. 3.6.

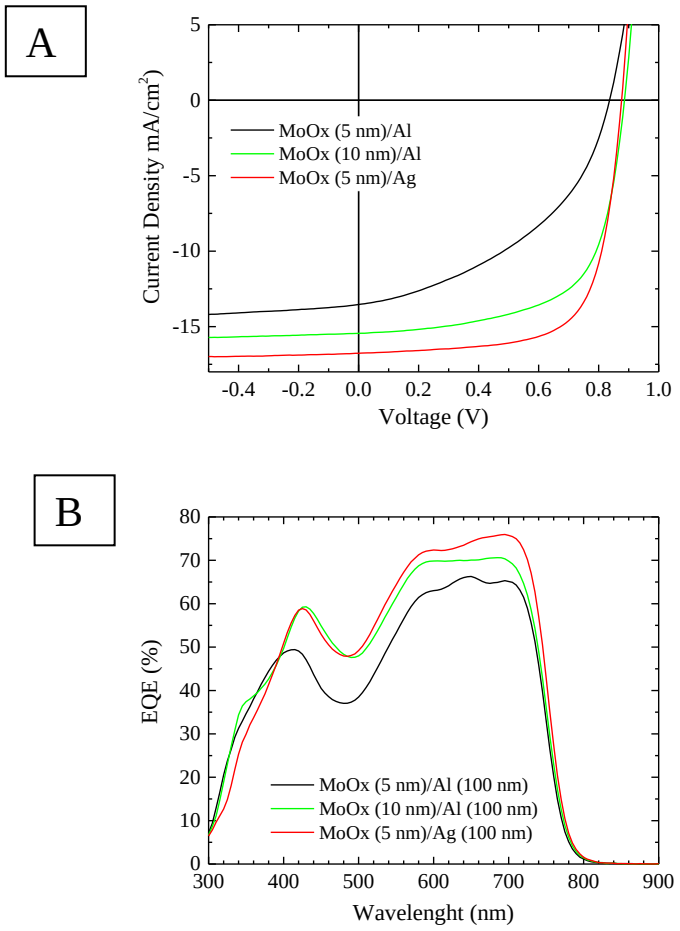

Fig. 3.15. Control device and devices fabricated varying the top electrode structures: A) J-V light characteristics; B) EQE spectra.

Tab. 3.6. J-V light values of the control device and of devices realized varying the top electrode structures.

Anode	**PCE (%)**	**FF (%)**	**J_{SC} (mA/cm^2)**	**V_{OC} (mV)**	**R_S (Ohm*cm^2)**	**R_{sh} (Ohm*cm^2)**
MoO_x (5 nm)/ Al	4.6	42.2	13.6 (13.2)	806	14	3.8E2
MoO_x(10 nm)/ Al	8.8	64.2	15.5 (14.9)	885	5.4	1.6E3
MoO_x(5 nm)/Ag	10.2	69.8	16.7 (15.6)	876	4.4	1.3E3

The J_{SC} values in brackets were obtained by the EQE measurements.

It can see that the device performance was largely dependent on the variation of MoO_x layer thickness, when it was combined to aluminium metal contact. In particular, the increase of the MoO_x thickness from 5 nm to 10 nm led to a significant enhancement of PV parameters with better values of series, R_S, and shunt (R_{sh}) resistances. Nevertheless, these results, especially in terms of J_{SC} and FF were lower than the performance of control cell.

This suggests that the optimization of MoO_x interlayers with a properly chosen metal electrode can reduce interfacial power losses improving, in this way, the device performance.

II) Incorporation of solution-processed HTL

The study of highly efficient (PBDB-T:ITIC)-based solar cells gave the opportunity to test the effect of incorporation of a solution-processed HTL layer such as PEDOT:PSS and to determine its role in contributing to device stability.

To this end, OPV devices were fabricated using this inverted architecture:

ITO/ZnO/ PBDB-T:ITIC (1:1 w/w) /PEDOT:PSS/Ag

where the PEDOT:PSS layer (*t*~55 nm) was spin-coated from previously optimized solution consisting of:

- PEDOT:PSS mixed to IPA (1:1) adding 0.11 wt% Zonyl FS-300 (fluorosurfactant)

Then, a thermal annealing on coated layer was carried out at 120°C for 10 minutes in air.

Fig. 3.16 shows the typical J-V characteristics under simulated AM1.5G solar irradiation (100 mW cm^{-2}) and EQE curves of the reference device based on evaporated MoO_x and PSC solar cells realized with solution-processed PEDOT:PSS.

Tab. 3.7 summarizes the photovoltaics parameters for the devices.

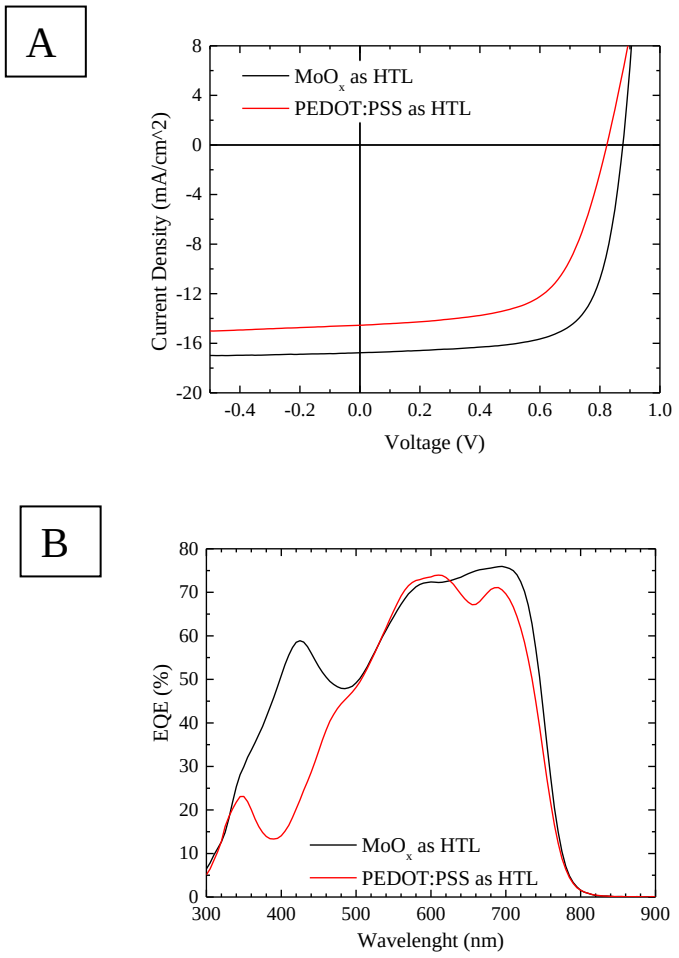

Fig. 3.16. Reference device with evaporated MoO_x as HTL compared to PSC solar cells with solution-processed PEDOT:PSS as HTL: A) J-V light characteristics; B) EQE spectra.

Tab. 3.7. J-V light values of the reference device with evaporated MoO_x as HTL compared to values of PSC solar cells with solution-processed PEDOT:PSS as HTL.

HTL layer	PCE (%)	FF (%)	J_{SC} (mA/cm^2)	V_{OC} (mV)	R_S (Ω*cm^2)	R_{sh} (Ω*cm^2)
MoO_x	10.2	69.8	16.7	876	4.4	1.3E3
PEDOT:PSS	7.3	60.6	14.4	831	9.5	1.1E3
After thermal annealing at 100°C for 44h						
PEDOT:PSS	7.1	60.8	14.2	823	9.5	1.5E3

The replacement of evaporated MoO_x layer with the solution-processed PEDOT:PSS resulted in lower electrical performance where the PCE decreased from 10.2 % to 7.3 % mainly due to a reduction for J_{SC} and FF values. However, note that the replacement did not induce drastic losses on the V_{OC}, nor did it considerably affect the overall resistance of the devices.

The EQE spectra indicated a substantial reduction in quantum efficiency at lower wavelengths between 300 nm and 500 nm while they highlighted a good response to sunlight at longer wavelengths with small changes in spectral shape.

According to these reasonable results, the solution-processed PEDOT:PSS-based devices were further tested in order to investigate their thermal and light stability.

The thermal test was based on monitoring the device performance after an annealing at 100°C for 44 hours in dark and under inert atmosphere.

As shown in Tab. 3.7, unexpectedly all the photovoltaic parameters remained constant at the end of experiment.

On the other hand, the light exposure caused rapid and progressive deterioration of electrical performance as shown in Fig. 3.17.

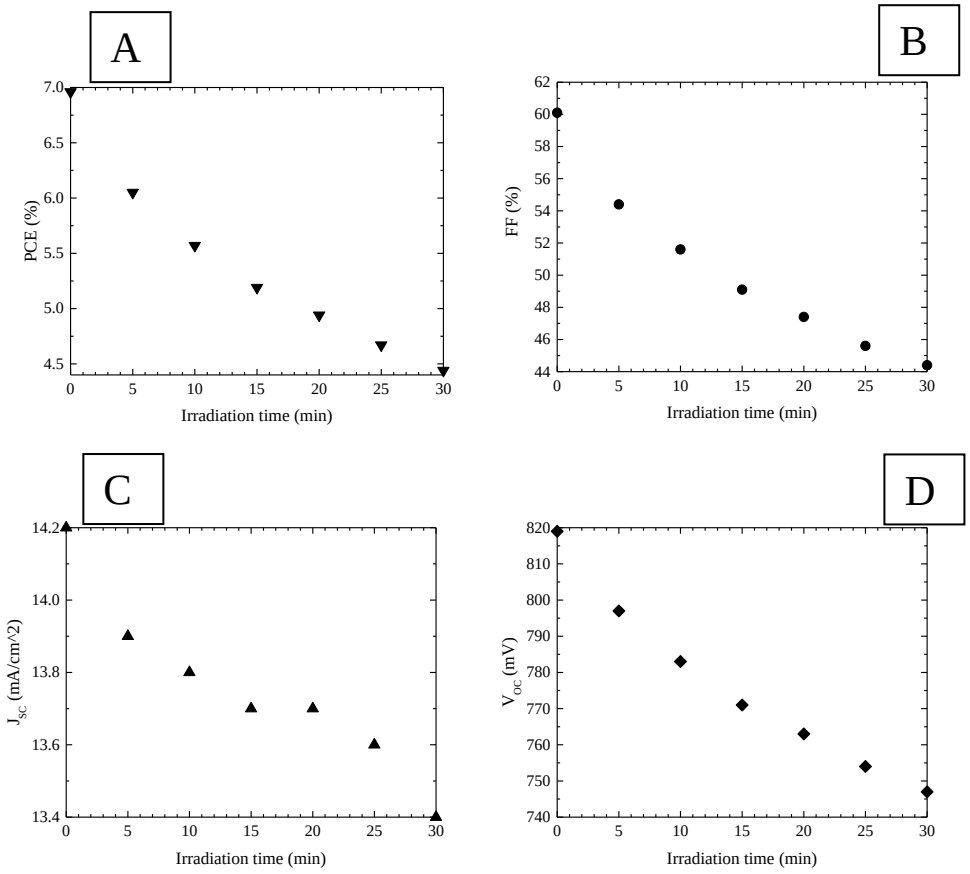

Fig. 3.17. Irradiation time (min) dependences of (A) PCE, (B) FF, (C) J_{SC} and (D) V_{OC} of the PBDB-T:ITIC bulk heterojunction solar cells.

The poor light stability with significant loss in device efficiency is a serious obstacle to overcome for the large-scale production under ambient conditions.

3.4 Ternary organic solar cells

The main limitation in the efficiency improvement for single-junction OSCs is that the absorption spectra of organic semiconductors are intrinsically narrow. Since J_{SC} is proportional to the number of absorbed photons and, thus, strongly depends on the absorption intensity and range of the active layer materials, it has been necessary to develop a useful

method to harvest much more photons in a simple and efficient way. Different strategies have been explored to tackle this issue such as the tandem and ternary polymer solar cells (Fig. 3.18).

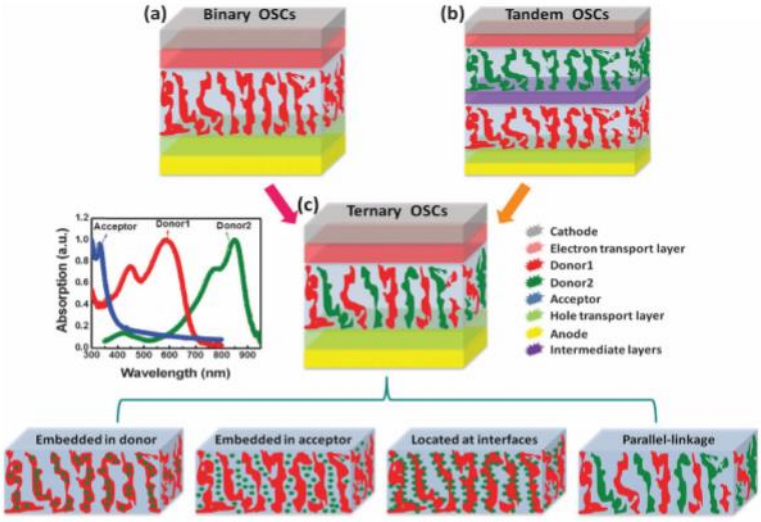

Fig. 3.18. The schematic configuration of the (a) conventional binary OSCs, (b) tandem OSCs, and (c) ternary OSCs with four possible active layer morphologies according to the location of the third component. [33]

The tandem solar cell consists of stacking two or more cells connected in series or parallel with complementary absorption spectra, which can harvest high and low energy photons, allowing also to reduce the thermalization loss of photonic energy. [34, 35, 36, 37, 38, 39]

However, this structure has some manufacturing limitations, such as the layer thickness of the sub-cells, the appropriate compatibility of different used materials and the fabrication costs.

On the other hand, ternary solar cell is a more promising strategy that combines the advantage to incorporate multiple organic materials like tandem solar cells and the simple processing conditions like single BHJ solar cells.

In the ternary organic solar cells, the active layer is made up of three components. Basically, the third component, such as polymer, a small molecule, a dye, or a nanoparticle, is put in the main donor:acceptor (D:A) matrix. [40, 41, 33, 42]

According to the type and the function of third component, the ternaries can be classified in three main groups:

- two donors/one acceptor (D1/D2/A); [43, 44, 45]
- one donor/two acceptors (D1/A1/A2); [46, 47, 48]
- donor/nonvolatile additive/acceptor (D/NA/A). [49, 50, 51]

The mechanism controlling the photovoltaic behavior in a ternary solar cell is sufficiently complex and it can be summarized in four fundamental principles dependent on the position of the third component in the bulk. They are:

- *charge transfer*: The correct location of the third component is related to the existing charge transport pathway of D/A system. Therefore, for the efficient charge transfer mechanism, it should be located at the interface between the donor and acceptor materials. For this reason, a careful design and selection of the third component are required to define an appropriate material size and orientation. Another important requirement is a suitable energy level alignment to avoid forming excitons and charge traps in the active layers. About this point, a cascade energy level alignment is an effective strategy to create additional pathways promoting, thus, the charge-transfer process, and, at the same time, to reduce the charge recombination in the ternary active layers. [39]
- *energy transfer*: this is an alternative and competitive process to charge transfer. Basically, the third component acts as energy

transfer agent (an energy donor or the energy acceptor). Since the radius of energy transfer (~10 nm) is limited, the energy donor should need have close contact with energy acceptor in order to guarantee an efficient process.

In general, two mechanisms, known as Förster and Dexter energy transfer, can happen, for which the crucial prerequisite is the overlap between the emission spectrum of a donor material and the absorption spectrum of the energy acceptor. [52]

- *parallel-linkage* and *alloy models*: These models are completely different and do not require a defined location and energy alignment.

  In particular, the ternary OSC acts as a parallel-linked tandem realizing an increased J_{SC} and a composition dependent V_{OC} tuned between the open circuit voltage values of reference binary devices. The mechanism has been explained by You et al. [53] employing two group of polymers and, in particular, fabricating a ternary cell with an active layer thickness of 100 nm and the two binary sub-cells of 50 nm. It has shown that the absorption profile of the ternary film is a linear combination of the spectra of the two binary sub-cells and the obtained J_{SC} values are very close to the sum of the two binary sub-cells while the V_{OC} lies between the values of the sub-cells. [54]

  Thompson et al. [39, 55] proposed another model, named as the *alloy model*. According to this, two electronically similar components in the ternary active layers (two donors or two acceptors) form an electronic alloy with the same frontier orbital (HOMO and LUMO) energies based on the average composition of these two components.

This model generally requires that the donors or acceptors of active layer have a good miscibility and compatibility.

Fig. 3.19 depicts the four fundamental principles of ternary solar cells.

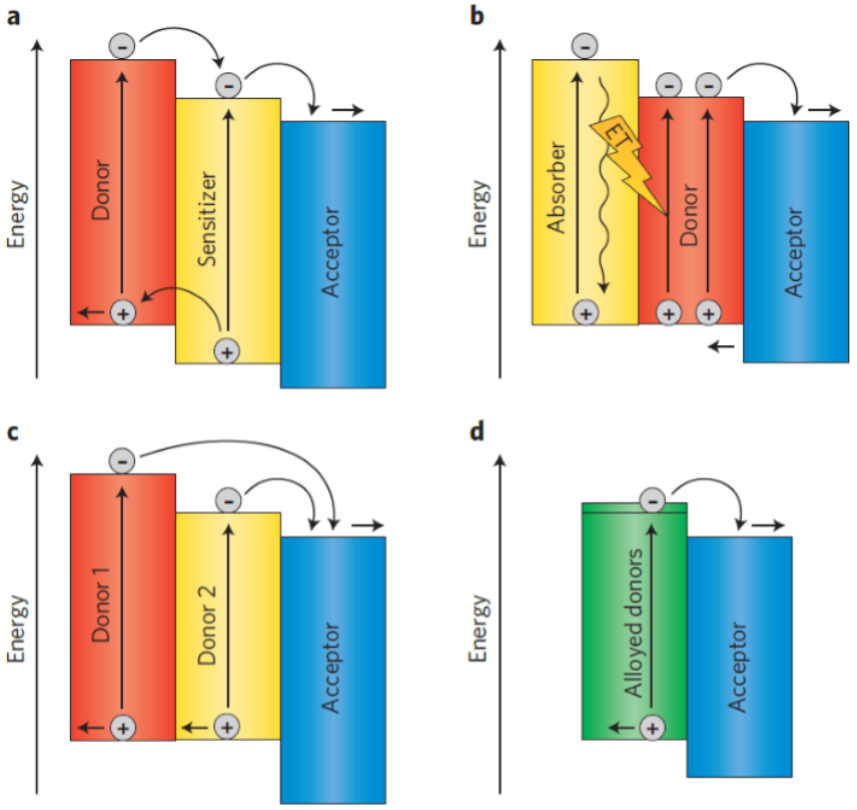

Fig. 3.19. Fundamental principles of ternary blend PSCs. a) Charge transfer mechanism; b) The energy transfer (ET) mechanism; c) Parallel-like model; d) Alloy-like model. [33]

In following section, ternary solar cells will be described considering both donor polymers and fullerene derivatives as third component in order to improve the performance of previously investigated binary system based on PBDB-T:ITIC.

As discussed, the presence of sensitizer potentially could offer multiple benefits and synergistic effects to fabricated devices such as an

enhancement of photon harvesting, a good energy level alignment, more efficiency of exciton dissociation, charge transport and extraction, a better stability and a good morphology.

3.4.1 D1:D2:A1 with PDTP-DFBT as third component

An effective method to broaden the absorption bandwidth of PBDB-T:ITIC based bulk heterojunction (BHJ) solar cells is to incorporate a near IR sensitizer into the host matrix. One of most promising donor polymer candidate as sensitizer is poly[2,7-(5,5-bis(3,7-dimethyl octyl)-5H-dithieno[3,2-b:20,30-d]pyran)-alt-4,7(5,6-difluoro-2,1,3 benzothiadiazole)], also known as PDTP-DFBT. It is characterized by a low band-gap of ~ 1.38 eV, a high hole mobility and deep HOMO level and has attracted a wide attention, in particular in the tandem systems [56], because its absorption characteristics up to 900 nm and suitable energy levels.

Herein, the performances of ternary solar cells, based on PBDB-T:ITIC as host matrix and PDTP-DFBT as third component, were investigated.

3.4.1.1 Device fabrication

All BHJ polymer solar cells were fabricated using spin coating as deposition method for active layer and the inverted configuration.

ITO/ZnO/ PBDB-T:PDTP-DFBT:ITIC (1:0.2:1 w/w) /MoO_x/Ag

Fig. 3.20 shows the chemical structure of PDTP-DFBT and the energy level diagram of ternary active layer.

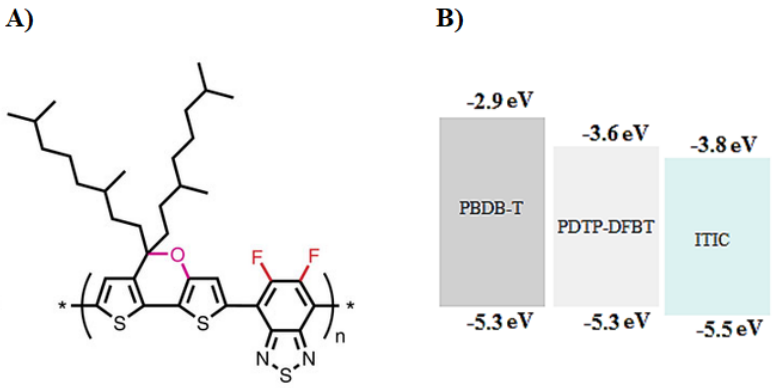

Fig. 3.20. A) Chemical structure of PDTP-DFBT; B) Energy-level diagram for PBDB-T, PDTP-DFBT and ITIC.

The materials used in this thesis are either commercially available. PDTP-DFBT donor material was purchased from 1-Material.

The devices were fabricated as described in the Section 3.2.1. The active layer that was spin coated under inert conditions using a chlorobenzene blend solution ([PBDB-T] = 10 mg mL^{-1}) with weight ratio of 1:0.2:1, adding 0.5 vol% of 1,8 DIO as additive and thermal annealed at 160°C for 30 minutes.

All the devices were characterized by UV-VIS spectroscopy, J-V measurements under simulated AM1.5G solar irradiation (100 mW cm^{-2}) and quantum efficiency measurements (EQE).

3.4.1.2 Characterization

Fig. 3.21, taken from literature [57], depicts the UV/vis absorption spectra of PDTP−DFBT solution and thin film. The polymer presents a small absorption peak around 400 nm and a main absorption range from ~600 to ~900 nm. This range at long wavelenghts is good to compensate that of PBDB-T:ITIC based film.

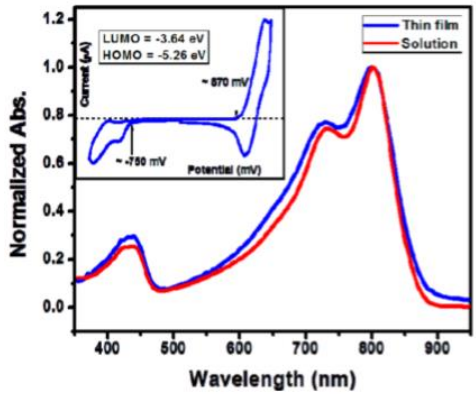

Fig. 3.21. Absorption spectra of PDTP−DFBT in chlorobenzene (∼0.1 mg/mL) and thin film casted from chlorobenzene; cyclic voltammetry of PDTP-DFBT thin film (inset). [57]

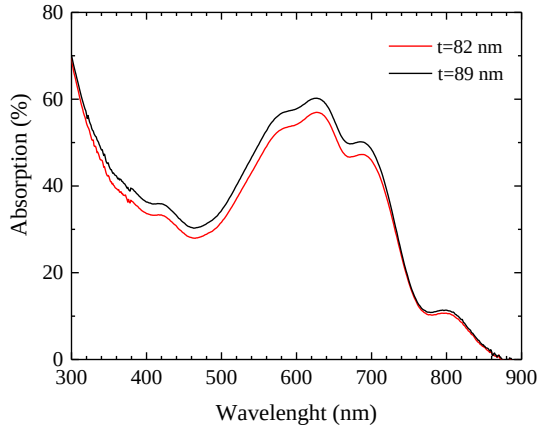

Fig. 3.22. Absorption spectra of PBDB-T:PDTP-DFBT:ITIC blend deposited on glass substrate with different thicknesses.

In order to evaluate the contribution of third component on the PBDB-T:ITIC absorption, optical analysis was performed by varying the spin speed obtaining thin film of different thicknesses such as *t*=82 nm and *t*= 89 nm. The incorporation of PDTP-DFBT amount in the host matrix led to a slight enhancement of absorption from 780 nm to 900 nm as reported in Fig. 3.22.

Fig. 3.23 displays J–V characteristics under illuminated conditions and EQE curves obtained from devices with different active layer thicknesses.

Tab. 3.8 summarizes the photovoltaics parameters for the devices.

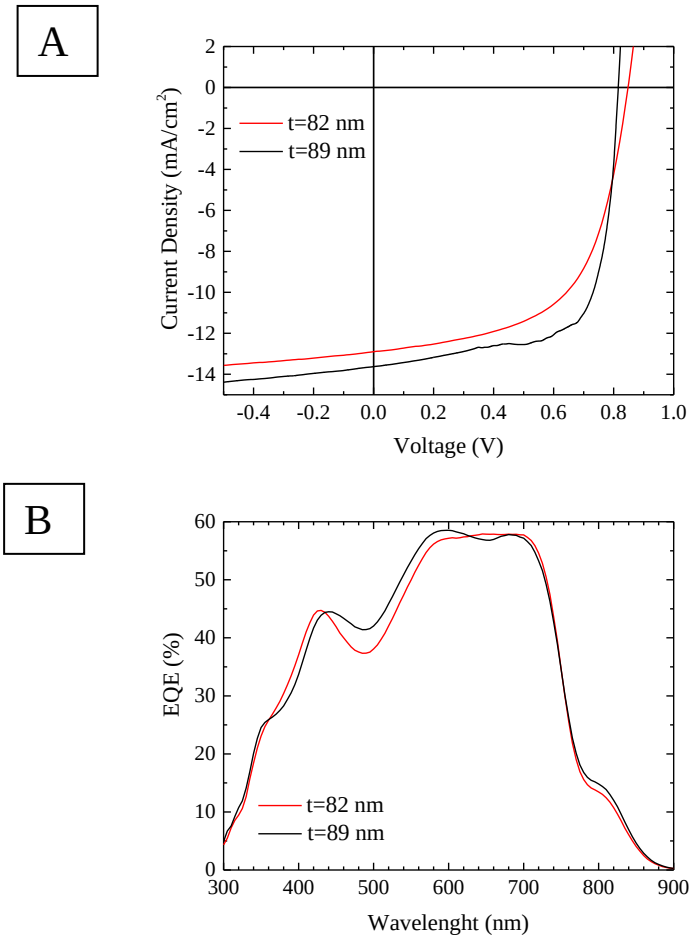

Fig. 3.23. Devices fabricated varying active layer thicknesses: A) J-V light characteristics; B) EQE spectra.

Tab. 3.8. J-V light values of the devices realized varying the active layer thickness.

Active layer thickness (nm)	**PCE (%)**	**FF (%)**	**J_{SC} (mA/cm^2)**	**V_{OC} (mV)**	**R_S ($Ohm*cm^2$)**	**R_{sh} ($Ohm*cm^2$)**
t=82 nm	6.5	58.8	13.0 (13.9)	847	9.5	5.6E2
t=89 nm	7.9	69.8	13.9 (12.7)	815	3.5	5.7 E2

The J_{SC} values in brackets were obtained by the EQE measurements.

The addition of sensitizer in the ternary system did not lead to significant improvements. The overall PCE was lower compared to previous reported binary solar cells. It can see a drop of all photovoltaic parameters and, even looking at the EQE spectrum, it emerges that the presence of PDTP-DFBT gave only a low contribution in the 750-900 nm region. This probably happened because there was not a favorable supramolecular assembly in the blend film for achieving an optimal morphology and, thus, to promote an efficient charge dissociation and transport.

3.4.2 D1:A1:A2 with [70]PCBM as third component

Since fullerene derivatives as acceptors have several advantages, i.e. the good isotropic electron transport capability, the strategy of ternary structure could favor an improvement or to involve a partially reduction of the deficiencies in the active layer to obtain better OSCs.

In the present work, ternary solar cells using one donor/two acceptors configuration with [70]PCBM as additional component were studied.

3.4.2.1 Device fabrication

The devices were fabricated in inverted architecture as described in the Section 3.2.1. The active layer consisted of PBDB-T as donor polymer, ITIC as first acceptor and the fullerene derivative as second acceptor material. The weight ratio of PBDB-T and [70]PCBM:ITIC acceptors was maintained at 1:1; the concentration of PBDB-T was 10 mg/mL. The weight ratio of [70]PCBM:ITIC acceptors was 0.5:0.5. Chlorobenzene was used as the host solvent and 1vol% 1,8 DIO was used as the solvent additive.

PBDB-T:[70]PCBM:ITIC active layer was formed by spin coating with different thicknesses and then annealed at various temperatures.

Binary control solar cells based on PBDB-T:ITIC blend were also fabricated as control cells.

Fig. 3.24 displays the energy levels of the materials (PBDB-T, [70]PCBM and ITIC) used in the ternary active layer.

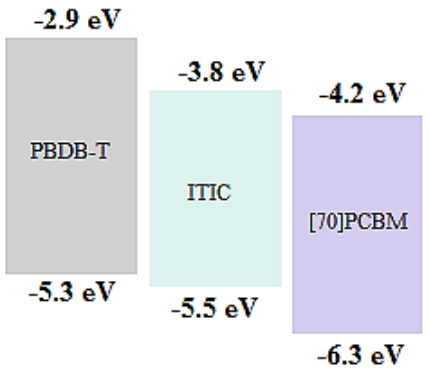

Fig. 3.24. Energy-level diagram for PBDB-T, [70]PCBM and ITIC.

It can see an ideal cascade like energy levels of ternary blend PSCs which can potentially facilitate charge transfer at the D/A interface owing to the bridging effect [58, 59], enhancing the V_{OC} and J_{SC} parameters.

3.4.2.2 Characterization

As previously shown in Fig. 3.10 [27], [70]PCBM is characterized by a weak visible absorption. On the contrary, ITIC exhibits strong absorption in the wavelength range of 500−850 nm complementary to that of PBDB-T.

The mixture of these three materials implicated a broad absorption over the entire visible spectrum. In particular, the presence of additional component into the ternary blends increased the absorption at low wavelenght but, at the time, a decrease of ITIC content led to a reduction of absorption peak from 650 nm to 800 nm.

The influence of fullerene derivative on ternary device performance was investigated by varying the blend thicknesses and the thermal annealing conditions.

The temperatures (T) of the active layer annealing process were fixed at 120°C and 140°C for 10 minutes under inert atmosphere.

Chosen temperatures were lower than the optimized one (T=160°C for 30 minutes) in order to avoid fullerene aggregation and consequent worsening of the blend morphology as discussed above.

Fig. 3.25 reports the absorption spectra of binary control PBDB-T:ITIC blend and the ternary blends containing fullerene derivative and ITIC as acceptors with weight ratio of 0.5:0.5 coated at different thicknesses and thermal annealing conditions.

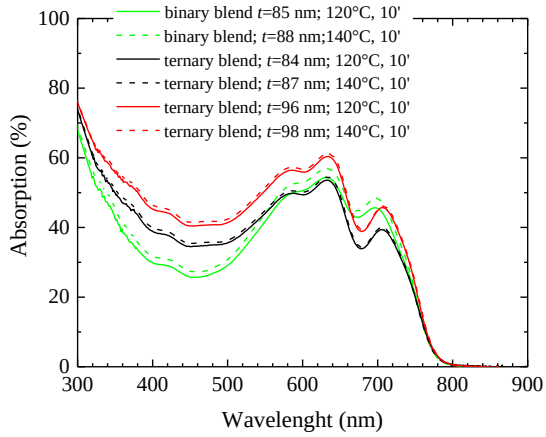

Fig. 3.25. Absorption spectra of binary control PBDB-T:ITIC-based blend and the ternary blends containing fullerene derivative and ITIC as acceptors with weight ratio of 0.5:0.5 deposited on glass substrate with different thicknesses and thermal annealing conditions.

The J-V characteristics and the corresponding EQE curves of binary control and ternary solar cells fabricated with different thicknesses and thermal annealing conditions are presented in Fig. 3.26.

The PV results are summarized in Tab. 3.9.

A

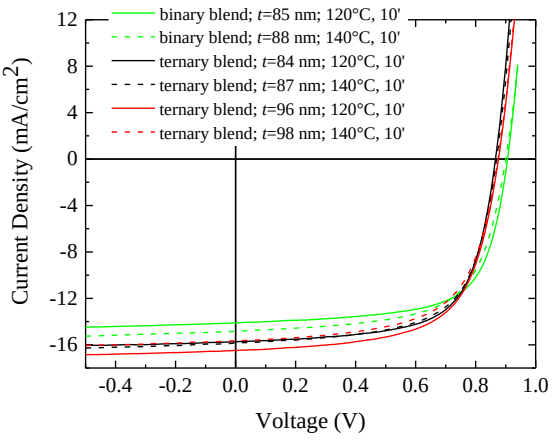

B

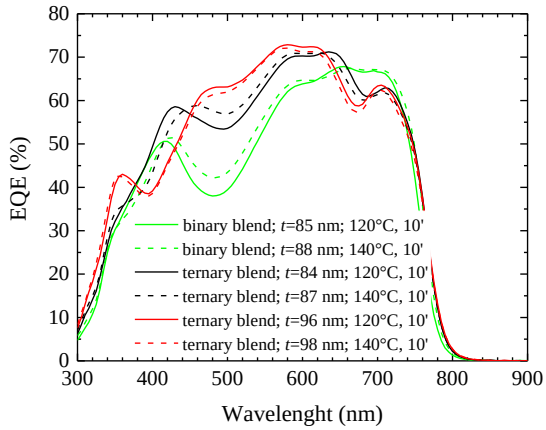

Fig. 3.26. Binary control PBDB-T:ITIC-based devices and the ternary solar cells containing fullerene derivative and ITIC as acceptors with weight ratio of 0.5:0.5 coated at different thicknesses and thermal annealing conditions: A) J-V light characteristics; B) EQE spectra.

Tab. 3.9. J-V light values of the Binary control PBDB-T:ITIC-based devices and the ternary solar cells containing fullerene derivative and ITIC as acceptors with weight ratio of 0.5:0.5coated at different thicknesses and thermal annealing conditions.

Active layer thickness	**PCE (%)**	**FF (%)**	**J_{SC} (mA/cm^2)**	**V_{OC} (mV)**	**R_S (Ohm*cm^2)**	**R_{Sh} (Ohm*cm^2)**
(**) *t*=85 nm (120°C)	8.7	67.7	14.3 (13.6)	905	5.2	7.6 E2
t=84 nm (120°C)	9.1	66.7	15.8 (15.2)	866	5.1	1.1 E3
t=87 nm (140C°)	9.0	64.7	16.0 (15.2)	869	4.9	6.4 E2
t=96 nm (120°C)	9.2	64.2	16.5 (15.5)	875	5.7	8.6E2
t=98 nm (140°C)	8.7	63.3	15.7 (15.2)	874	5.8	9.1E2

(**) Binary control solar cell.

The J_{SC} values in brackets were obtained by the EQE measurements.

Note that the PV performances reported for binary control device was lower than the best optimized device shown in the section 3.3.2. This was probably caused to the change of active layer processing conditions such as the use of larger amount (1 vol/vol%) of DIO as additive and lower annealing temperatures in shorter time.

As reported in Tab. 3.9, despite a slight decreased V_{OC}, it can see that the overall PCE of ternary solar cells is unchanged (~9%) and the main contribution of third component led to a satisfying improvement of J_{SC}.

The same observation is derived from EQE spectra where the incorporation of sensitizer produced a significant enhancement in the 400 nm-700 nm region thanks to a higher charge collection efficiency.

Therefore, it was found a good agreement between the J_{SC} values obtained from the J-V and EQE measurements.

It is necessary to carry out further tests in order to find a better match among a more suitable fullerene derivative acceptor, ITIC and the polymer donor for achieving higher efficiencies.

Bibliography of Chapter 3

[1] S. B. Dkhil, M. Pfannmöller, M. I. Saba, M. Gaceur, H. Heidari, C. Videlot-Ackermann, A. G. O. Margeat, J. Bisquert, G. Garcia-Belmonte, A. Mattoni, S. Bals and J. Ackermann, *Adv. Energy Mater.* , vol. 7, p. 1601486, 2017.

[2] M. Jørgensen, K. Norrman, S.-A. Gevorgyan, T. Tromholt, B. Andreasen and F. C. Krebs, *Adv. Mater.*, vol. 24, p. 580, 2012.

[3] P. Cheng and X. Zhan, *Chem. Soc. Rev.*, vol. 45, p. 2544, 2016.

[4] S. A. Gevorgyan, M. V. Madsen, B. Roth, M. Corazza, H. Hösel, M., R. R. Søndergaard, M. Jørgensen and F. C. Krebs, *Adv. Energy Mater.*, vol. 6, p. 1501208, 2016.

[5] H. C. Wong, Z. Li, C. H. Tan, H. Zhong, Z. Huang, H. Bronstein, I. McCulloch, J. T. Cabral and J. R. Durrant, *ACS Nano*, vol. 2, p. 1297, 2014.

[6] G. Wantz, L. Derue, O. Dautel, A. Rivaton, P. Hudhommed and C. Dagron-Lartigaue, *Polym. Int.* , vol. 63, p. 1346, 2014.

[7] N. Li and C. J. Brabec, *Energy Environ. Sci.*, vol. 2, pp. 2902-2909 , 2015.

[8] A. C. Arias, M. Granström, D. S. Thomas, K. Petritsch and R. H. Friend, *Phys. Rev. B* , vol. 60, p. 1854–1860, 1999.

[9] J. Yuan, X. Huang, H. Dong, J. Lu, T. Yang, Y. Li, A. Gallagher and W. Ma, *Org. Electron.* , vol. 14, p. 635–643, 2013.

[10] Z. He, C. Zhong, S. Su, M. Xu, H. Wu and Y. Cao, *Nat. Photonics* , vol. 6, p. 591–595, 2012.

[11] F. C. Krebs, S. A. Gevorgyan and J. Alstrup, *J. Mater. Chem.*, vol. 19, no. 30, p. 5442, 2009.

[12] Y. Liu, J. Zhao, Z. Li, C. Mu, W. Ma, H. Hu, K. Jiang, H. Lin, H.

Ade and H. Yan, *Nat. Commun.* , vol. 5, p. 5293, 2014.

[13] H. Hoppe, S. Shokhovets and G. Gobsch, *Phys. Status Solidi RRL*, vol. 1, p. R40, 2007.

[14] H. Hansel, H. Zettl, G. Krausch, R. Kissilev, M. Thelakkat and H.-W. Schmidt, *Adv. Mater.* , vol. 15, p. 2056, 2003.

[15] J. Gilot, I. Barbu, M. M. Wienk and R. A. J. Janssen, *Appl. Phys. Lett.* , vol. 91, p. 113520, 2007.

[16] F. Liu, W. Zhao, J. R. Tumbleston, C. Wang, Y. Gu, D. Wang, A. L. Briseno, H. Ade and T. P. Russell, *Adv. Energy Mater.,* vol. 4, no. 5, pp. 1-9, 2014.

[17] Y. Liang, Z. Xu, J. Xia, S. T. Tsai, Y. Wu, G. Li, C. Ray and L. Yu, *Adv. Funct. Mater.* , vol. 22, p. E135−E138, 2010.

[18] L. Ye, Y. Jing, X. Guo, H. Sun, S. Zhang, M. Zhang, L. Huo and J. Hou, *J. Phys. Chem. C* , vol. 117, p. 14920−14928, 2013.

[19] B. J. T. d. Villers, K. A. O'Hara, D. P. Ostrowski, P. H. Biddle, S. E. Shaheen, M. L. Chabinyc, D. C. Olson and N. Kopidakis, *Chem. Mater.,* vol. 28, no. 3, p. 876–884, 2016.

[20] H. Zhou, Y. Zhang, J. Seifter, S. D. Collins, C. Luo, G. C. Bazan, T. Q. Nguyen and A. Heeger, *Adv. Mater.,* vol. 25, pp. 1646-1652, 2013.

[21] Z. He, C. Zhong, X. Huang, W. Y. Wong, H. Wu, L. Chen, S. Su and Y. Cao, *Adv. Mater.* , vol. 23, p. 4636−4643, 2011.

[22] X. Liu, W. Wen and G. C. Bazan, *Adv. Mater.* , vol. 24, pp. 4505-4510, 2012.

[23] S. Guo, B. Cao, W. Wang, J. F. Moulin and P. Müller-Buschbaum, *ACS Appl. Mater. Interfaces,* vol. 7, p. 4641−4649, 2015.

[24] M. Reese, S. Gevorgyan, M. Jørgensen, E. Bundgaard, S. Kurtz, D. Ginley, D. Olson, M. Lloyd, P. Morvillo, E. Katz, A. Elschner, O. Haillant, T. Currier, V. Shrotriya, M. Hermenau, M. Riede, K. Kirov,

G. Trimmel, T. Rath, O. Inganäs and al., *Sol. Ener. Mater. Sol. Cells*, vol. 95, pp. 1253-1267, 2011.

[25] J. Guo, Y. Liang, J. Szarko, B. Lee, H. J. Son, B. S. Rolczynski and L. Chen, *J. Phys. Chem. B*, vol. 114, p. 742–748, 2010.

[26] M. Jorgensen, K. Norrman and F. Krebs, *Sol. Ener. Mater. Sol. Cells* , vol. 92, p. 686–714, 2008.

[27] W. Zhao, D. Qian, S. Zhang, S. Li, O. Inganäs, F. Gao and J. Hou, *Adv. Mater.* , vol. 28, pp. 4734-4739, 2016.

[28] Y. Lin, J. Wang, Z. G. Zhang, H. Bai, Y. Li, D. Zhu and X. Zhan, *Adv. Mater.* , vol. 27, p. 1170−1174. , 2015.

[29] Z. Li, K. Jiang, G. Yang, J. Y. L. Lai, T. Ma, J. Zhao, W. Ma and H. Yan, *Nat. Commun.*, vol. 7, p. 13094, 2016.

[30] P. Zhu, B. Fan, X. Du, X. Tang, N. Li, F. Liu, L. Ying, Z. Li, W. Zhong, C. J. Brabec, F. Huang and Y. Cao, *ACS Appl. Mater. Interfaces*, vol. 10, p. 22495−22503, 2018.

[31] J. B. Kim, C. S. Kim, Y. S. Kim and Y. -L. Loo, *Appl. Phys. Lett.* , vol. 95, p. 183301, 2009.

[32] S. Chambon, L. Derue, M. Lahaye, B. Pavageau, L. Hirsch and G. Wantz, *Materials*, vol. 5, pp. 2521-2536, 2012.

[33] L. Lu, M. A. Kelly, W. You and L. Yu, *Nat. Photonics*, vol. 9, pp. 491-500, 2015.

[34] Z. M. Beiley, M. G. Christoforo, P. Gratia, A. R. Bowring, P. Eberspacher, G. Y. Margulis, C. Cabanetos, P. M. Beaujuge, A. Salleo and M. D. McGehee, *Adv. Mater.*, vol. 25, pp. 7020-7026, 2013.

[35] T. Ameri, G. Dennler, C. Lungenschmied and C. J. Brabec, *Energy Environ. Sci.* , vol. 2, p. 347, 2009.

[36] H. P. Lu, A. N. Bartynski, M. J. Greaney, M. E. Thompson and R. L. Brutchey, *ACS Appl. Mater. Interfaces*, vol. 6, p. 18306–18311,

2014.

[37] O. Adebanjo, P. P. Maharjan, P. Adhikary, M. T. Wang, S. F. Yang and Q. Q. Qiao, *Energy Environ. Sci.*, vol. 6, p. 3150–3170, 2013.

[38] S. Sista, Z. Hong, L.-M. Chen and Y. Yang, *Energy & Environmental Science* , vol. 4, pp. 1606-1620, 2011.

[39] P. P. Khlyabich, B. Burkhart and B. C. Thompson, *J. Am. Chem. Soc.*, vol. 133, p. 14534–14537, 2011.

[40] M. Zhang, F. Zhang, Q. An, Q. Sun, J. Wang, L. Li, W. Wang and J. Zhang, *Sol. Energy Mater. Sol. Cells*, vol. 141, pp. 154-161, 2015.

[41] Y. G. Zhen, H. Tanaka, K. Harano, S. Okada, Y. Matsuo and E. Nakamura, *J. Am. Chem. Soc.*, vol. 137, pp. 2247-2252, 2015.

[42] B. H. Lessard, J. D. Dang, T. M. Grant, D. Gao, D. S. Seferos and T. P. Bender, *ACS Appl. Mater. Interfaces*, vol. 6, p. 15040–15051, 2014.

[43] H. C. Hesse, J. Weickert, C. Hundschell, X. Feng, K. Müllen, B. Nickel, A. J. Mozer and L. Schmidt-Mende, *Adv. Energy Mater.*, vol. 1, pp. 861-869, 2011.

[44] S. Honda, T. Nogami, H. Ohkita, H. Benten and S. Ito, *ACS Appl. Mater. Interfaces*, vol. 1, pp. 804-810, 2009.

[45] Q. An, F. Zhang, L. Li, Z. Zhuo, J. Zhang, W. Tang and F. Teng, *Phys. Chem. Chem. Phys.*, vol. 16, p. 16103–16109, 2014.

[46] S.-J. Ko, W. Lee, H. Choi, B. Walker, S. Yum, S. Kim, T. J. Shin, H. Y. Woo and J. Y. Kim, *Adv. Energy Mater.*, vol. 5, p. 1401687, 2015.

[47] T.-Y. Huang, D. Patra, Y.-S. Hsiao, S. H. Chang, C.-G. Wu, K.-C. Ho and C.-W. Chu, *J. Mater. Chem. A*, vol. 3, p. 10512–10518, 2015.

[48] W. L. Leong, S. R. Cowan and A. J. Heeger, *Adv. Energy Mater.*, vol. 1, pp. 517-522, 2011.

[49] Q. Wei, T. Nishizawa, K. Tajima and K. Hashimoto, *Adv. Mater.*, vol. 20, p. 2211–2216, 2008.

[50] Y.-J. Cheng, C.-H. Hsieh, P.-J. Li and C.-S. Hsu, *Adv. Funct. Mater.*, vol. 21, p. 1723–1732, 2011.

[51] F. Bonaccorso, N. Balis, M. M. Stylianakis, M. Savarese, C. Adamo, M. Gemmi, V. Pellegrini, E. Stratakis and E. Kymakis, *Adv. Funct. Mater.*, vol. 25, p. 3870–3880, 2015.

[52] Y. Wang, H. Ohkita, H. Benten and S. Ito, *Phys. Chem. Chem. Phys.* , vol. 17, p. 27217, 2015.

[53] L. Yang, H. Zhou, S. C. Price and W. You, *J. Am. Chem. Soc. 134, (2011).* , vol. 134, p. 5432–5435, 2011.

[54] N. Gasparini, Controlling charge carrier recombination in ternary organic solar cells, 2017.

[55] R. A. Street, D. Davies, P. P. Khlyabich, B. Burkhart and B. C. Thompson, *J. Am. Chem. Soc.*, vol. 135, p. 986−989, 2013.

[56] J. You, L. Dou, K. Yoshimura, T. Kato, K. Ohya, T. Moriarty, K. Emery, C.-C. Chen, J. Gao, G. Li and Y. Yang, *Nat. Comun.*, vol. 4, p. 1446, 2013.

[57] L. Dou, C. -C. Chen, K. Yoshimura, K. Ohya, W. -H. Chang, J. Gao, Y. Liu, E. Richard and Y. Yang, *Macromolecules 46, 9,* , vol. 46, no. 9, pp. 3384-3390, 2013.

[58] H. Kang, K.-H. .. Kim, T. E. Kang, C. -H. Cho, S. Park, S. C.Yoon and B. J. Kim, *ACS Appl. Mater. Interfaces*, vol. 5, p. 861, 2013.

[59] H. Cha, D. S. Chung, S. Y. Bae, M. -J. Lee, T. K. An, J. Hwang, K. H. Kim, Y. -H. Kim, D. H. Choi and C. E. Park, *Adv. Funct. Mater.*, vol. 23, p. 1556, 2013.

CHAPTER 4

Laminated flexible polymer solar cells (PSCs)

4.1 Introduction

As a part of the PhD project I spent three months at Linköpings Universitet (Sweden), working in the group of Biomolecular and Organic Electronics under supervision of Prof. Olle Inganäs. This chapter presents the results of activity carried out there.

As discussed in Chapter 3, the current research interest in the OPV field is the realization of all-solution processable, low cost, flexible and semitransparent polymer solar cells for the upscaling and to favor the industrialization in new and appealing applications, such as measurement of the indoor humidity and temperature or energy-generating color window glasses. [1]

In recent years, many efforts have been made to develop materials and production methods that are scalable with high throughput, such as roll-to-roll (R2R) printing under ambient atmosphere, replacing, for example, the expensive vacuum-based processing techniques.

The lamination process is a potentially useful method to satisfy these requirements thanks to its simplicity and low cost.

Its basic principle consists of the fabricating two parts of a PSC separately on flexible substrates (i.e. PET) and finishing the device by a lamination step. During this key step, the two stacks are forced together between the heated rollers with a definite pressure using, i.e, active layer or electrode as

adhesive creating, thus, an intimate contact at the interface, both mechanically and electronically (Fig. 4.1). [2]

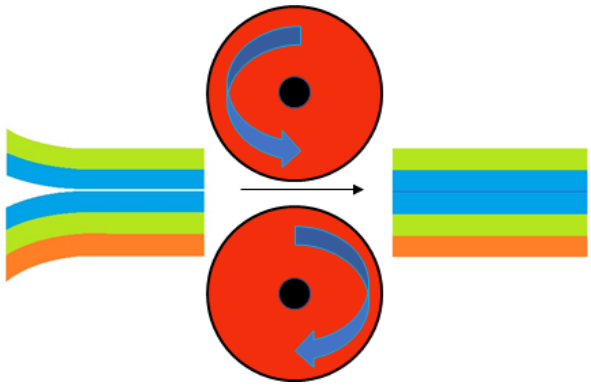

Fig. 4.1. Schematic of roll-to-roll lamination using the active layer as the adhesive.

Therefore, the lamination approach can play a crucial role in order to realize the ultimate goal of low-cost and semitransparent polymer solar cells. However, before the commercialization, it is necessary to overcome some processing limitations such as, the high temperatures and high pressures conditions, which unavoidably implicate a modification the active layer morphology and that can cause the degradation of the plastic PET substrate (for T> 140°C), associated also to the very low efficiency achieved so far, due to a variety of possible reasons. [3]

Up to now, several studies have been carried out on direct lamination of organic films to form planar and bulk heterojunction OPVs. [4, 5, 6, 7]

One of most promising donor polymer for upscaling synthesis and deposition methods for R2R printing methods is TQ1 (described in Chapter 2). It, paired with [70]PCBM, was already tested in well performing laminated solar cells. [8]

In this work, ternary non fullerene-based polymer solar cells and mini-modules, coated on flexible PEDOT:PSS electrodes and processed by scalable roll lamination method, were investigated. In particular the active

layer was based on TQ1 as donor polymer, IDTBR as first small molecule acceptor and IDFBR as second non fullerene acceptor.

4.2 Device fabrication

Laminated solar cells were realized in inverted configuration, according to the following structure:

PET/PEDOT:PSS/ETL/**Active layer** *to* **Active layer**/PEDOT:PSS/PET

The BHJ architecture and the energy level diagram of active layer (AL) materials are reported in Fig. 4.2.

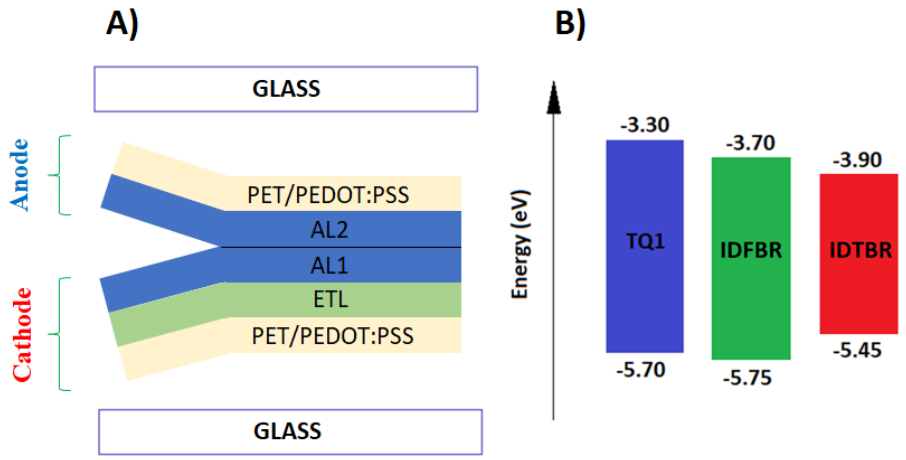

Fig. 4.2. A) Device architecture; B) Energy level diagram.

Most materials used in this work are commercially available. TQ1 was synthesized according to ref. [9], IDTBR and IDFBR were purchased from 1-Material; [70]PCBM (99%) was bought from Solenne BV and ZnO nanoparticles were bought from InfinityPV.

For device fabrication, all device steps were carried out in a glove box (<10 ppm O_2, H_2O) or in ambient conditions.

The PEDOT:PSS solution was prepared by mixing the PEDOT:PSS PH1000 (Heraeus) with 6 vol% ethylene glycol and 0.5 vol% Capstone FS-30 and, then, coated in ambient on polyethylene terephthalate (PET) substrates using a roll-to-roll slot-die coater. The thermal annealing process was performed at T=110°C for 10 minutes. Subsequently, the polyethylenimine (PEI) cathode layer (5-10 nm), obtained from isopropanol solution (1g/L), was slot-die coated or, as alternative ETL, ZnO nanoparticles were spin coated and annealed at T=120°C for 5 minutes. Then, the active layer (AL), consisting of TQ1, IDTBR and IDFBR, whose weight ratio was 1:0.7:0.3, was spin or blade coated both on the cathode stack PET/PEDOT:PSS/ETL and on top of the anode stack PET/PEDOT:PSS.

At this point, the two separated stacks were laminated together using a roll laminator (DH 360 Roll Laminator Graphic Solutions Scandinavia AB) at T= 120°C and with a force of ~30N between the lamination rollers in order to build the whole PSC.

Finally, all samples were encapsulated with glass lids and UV-curing adhesive (Delo glue).

J–V measurements were performed using Keithley 2400 Source Meter under AM1.5G illumination with a solar simulator (LSH7320 LED Solar Simulator, Newport).

UV–Vis was measured with a Lambda 950 UV-Vis (Perkin Elmer).

4.3 Characterization

4.3.1 Single laminated ternary PSCs

According to optical properties that a ternary solar cell needs to have in order to ensure a broad absorption and to allow enhanced solar harvesting,

an optical analysis of the three individual components and of blend layer was carried out. The normalized absorption spectra are reported in Fig. 4.3.

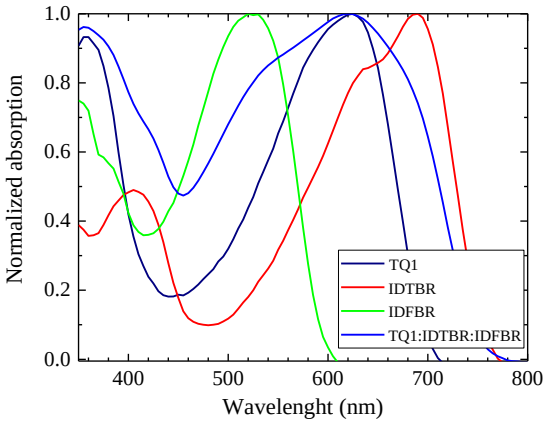

Fig. 4.3. Normalized absorption spectra of TQ1, IDTBR, IDFBR and blend active layer TQ1:IDTBR:IDFBR.

It can see that the three chosen compounds to build the ternary PSC exhibited a good complementarity in whole visible range. In particular, the host polymer donor showed a significant absorption from 450 nm to 700 nm while the absorption peak observed in the near IR range corresponds to the absorption bands of main small molecule acceptor, IDTBR, and the peak at around 400–600 nm belongs to the guest component, IDFBR.

Simultaneously, in the Fig. 4.3 is also presented a broad absorption profile of ternary film with maximum value at 620 nm and at 350 nm.

The optimal conditions for producing the active layer thin film were obtained by scanning the chemical and physical features. In particular:

- Solvent such as dichlorobenzene (DCB) and chlorobenzene (CB);
- Concentration such as 10 mg/mL and 25 mg/mL;
- Thickness varying spin speed (rpm).

Fig. 4.4 (A-C) shows the typical current density vs voltage (J-V) characteristics of the devices fabricated by varying solvent, concentration and spin speed under simulated AM1.5G solar irradiation (100 mW cm^{-2}). The Tab. 4.1 summarizes the PV parameters of so fabricated devices.

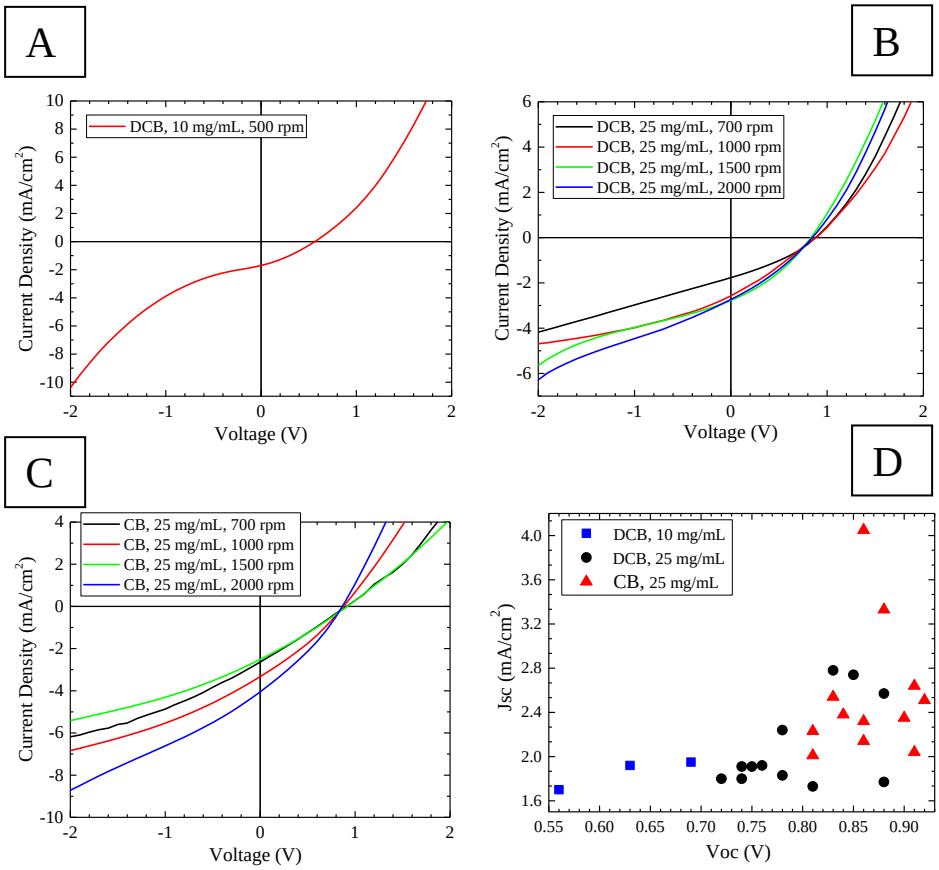

Fig. 4.4. The J-V characteristics of TQ1:IDTBR:IDFBR-based laminated devices fabricated by A) 10 mg/mL dichlorobenzene blend solution at 500 rpm; B) 25 mg/mL dichlorobenzene blend solution at different spin speed; C) 25 mg/mL chlorobenzene blend solution at different spin speed; D) J_{SC} vs V_{OC} for all fabricated devices.

Tab. 4.1. PV device parameters of TQ1:IDTBR:IDFBR-based laminated solar cells fabricated by varying solvent, concentration and spin speed under 1 sun illumination (100 mW cm^{-2}).

	Spin speed (rpm)	**PCE (%)**	**FF (%)**	**J_{SC} (mA/cm^2)**	**V_{OC} (V)**
10 mg/mL DCB	500	0.43	32	1.95	0.69
25 mg/mL DCB	700	0.51	33	1.77	0.88
	1000	0.63	28	2.57	0.88
	1500	0.77	33	2.78	0.83
	2000	0.71	30	2.74	0.85
25 mg/mL CB	700	0.63	26	2.64	0.91
	1000	0.88	30	3.33	0.88
	1500	0.63	27	2.51	0.92
	2000	1.06	30	4.05	0.86

Note that the shown J-V curves were recorded after applying a high reverse bias pulse to remove the short-circuiting (or shunting) behavior. [10] It is still unclear what causes the shunting problem, but it could be due to the contact between the top and the bottom electrodes, [11] or to a nonselective PEDOT:PSS anode or also correlated to the wet deposition of the top electrode. The common method to tackle it consists of applying a high reverse bias pulse. [8].

Fig. 4.4 D summarizes the J_{SC} values as a function of V_{OC} values for all fabricated ternary solar cells. Notably, there are three distinct regions

corresponding to the three prepared solutions and it can observe that the highest values were obtained for 25 mg/mL chlorobenzene solution.

In all analyzed cases, the performance of the laminated devices was very poor with identical and low FF, good V_{OC} values thanks to a deep HOMO level of TQ1 and an enhanced J_{SC} for the devices processed from 25 mg/mL chlorobenzene solution. Therefore, the low PCE values of laminated devices are primarily linked to the low FF values (~30%).

Many factors contribute to reduce and degrade the performance of devices such as the multistep manufacturing process and the ambient operating conditions. Ideally, the whole process should be performed under inert atmosphere in order to avoid the exposure to air and to the dust particles (micrometer size range). In fact, the latter could damage the mechanical adhesion and electrical contact of solar cells. [8]

4.3.2 Laminated Solar Mini-modules

As previously discussed, the lamination method combines the ease of processing to low costs and, for these reasons, it could be potentially applied to the module fabrication.

Photovoltaic modules represent an important step for the commercialization. They consist of monolithically connected solar cells to obtain the desired output voltage and output current for a specified application.

Motivated by this purpose, an attempt of building a series connected mini-modules was performed where the top electrode of the first sub-cell is monolithically connected to the bottom electrode of the next sub-cell and so on. Thereby, the output voltage of the module is directly proportional to

the number of cells connected in series while the output current is dependent on the active area.

In the fabrication process, the blend layer was deposited both by spin coating and by blade coating. The first technique allows to obtain better and more reproducible results, but it is not suitable for large-scale production and involves the use of a large solution volume. Latter is a simple technique that allows to minimize the amount of blend solution but the low speed could lead to the aggregation or crystallization at high concentration of materials during the coating process.

Fig. 4.5 displays the J-V characteristics and photograph of the solar mini-modules depositing the active layer through spin or blade coating from 25 mg/mL dichlorobenzene or chlorobenzene solution. A summary of the photovoltaic parameters of the reference single cells and mini-modules is reported in Tab. 4.2.

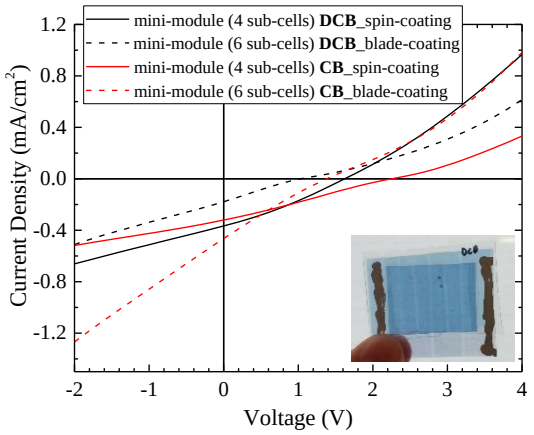

Fig. 4.5. J-V characteristics and photograph (as insert) of the solar mini-modules fabricated by using spin or blade coating for the active layer deposition from 25 mg/mL dichlorobenzene or chlorobenzene solution.

Tab. 4.2. Photovoltaic device parameters of single solar cells (SC) and mini-modules (MM) fabricated by using spin or blade coating for the active layer deposition from 25 mg/mL dichlorobenzene or chlorobenzene solution.

		Deposition	**N°cell**	**PCE (%)**	**FF (%)**	**J_{SC} (mA/cm^2)**	**V_{OC} (V)**
25 mg/mL DCB	SC	Spin-coating	1	0.22	21	1.86	0.56
	MM		4	0.18	29	0.37	1.62
	SC	Blade-coating	1	0.03	26	0.64	0.20
	MM		6	0.06	23	0.24	1.10
25 mg/mL CB	SC	Spin-coating	1	0.23	24	1.63	0.60
	MM		4	0.18	25	0.32	2.25
	SC	Blade-coating	1	0.05	25	0.85	0.26
	MM		6	0.15	23	0.46	1.38

In both the cases examined, the mini-modules did not work. The electrical parameters were very low. Notably, the V_{OC} lacked the voltage of approximately 1-2 sub-cells. The module J_{SC} was lower compared to the J_{SC} of a single cell.

It is known that in the series connected-modules the lowest J_{SC} limits the overall current of module. The possible current variations can be caused by internal or external factors. Internal variations depend on large difference of thickness in the active layer or defects, while external variations can be due to different illumination conditions (i.e. shadowing effect).

Another important limitation on the functioning of a photovoltaic module is commonly related to the losses due to the resistance of the interconnecting area.
In addition to these reasons, the poor performance of the ternary blend should be considered.

4.3.3 Single laminated binary PSCs

In order to understand the limiting factors inside the active layer, the role of IDFBR was investigated by fabricating laminated binary solar cells based on TQ1 and IDFBR. In particular, bulk and planar heterojunctions (BHJ and PHJ, respectively) were realized.
Laminated BHJ binary solar cells were prepared by depositing the active layer through spin coating method from 25 mg/mL xylene blend solution and by testing the influence of different ETLs such as ZnO or polyethylenimine (PEI) on device performance.
Fig. 4.6 show the comparison of absorption spectra of binary and ternary blend thin films and the J-V characteristics of laminated BHJ solar cells using different buffer layers (ETLs) and by varying their thicknesses.
Tab. 4.3 summarizes the photovoltaic parameters for the BHJ solar cells.

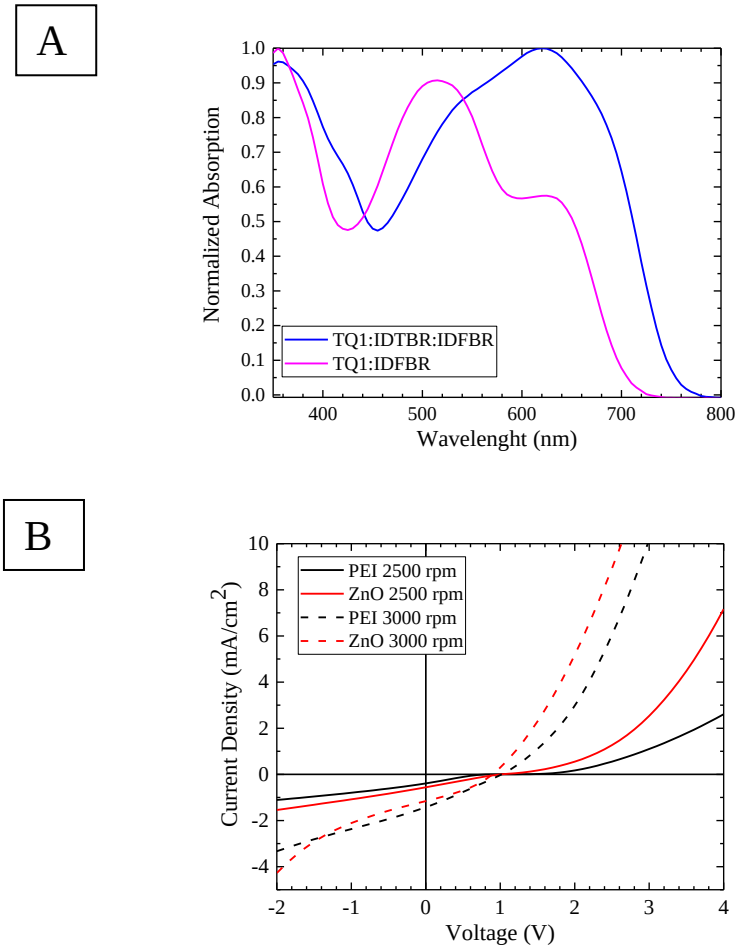

Fig. 4.6. A) Absorption spectra of binary and ternary blend thin films; B) The J-V characteristics of laminated BHJ solar cells fabricated by varying ETL layer and thickness.

Tab. 4.3. Photovoltaic device parameters of laminated BHJ solar cells fabricated by varying ETL layer and thickness.

ETL	PCE (%)	FF (%)	J_{SC} (mA/cm^2)	V_{OC} (V)
PEI 2500 rpm	0.08	20	0.47	0.85
PEI 3000 rpm	0.13	23	0.56	1.01
ZnO 2500 rpm	0.38	26	1.42	1.02
ZnO 3000 rpm	0.35	34	1.16	0.90

Note that the J-V curves recorded by device fabricated with PEI as ETL showed undesirable S-kinks in the fourth quadrant with inflection point located at V_{OC}, resulting in very low PCE because of a significant reduction of fill factor (FF), even if the open circuit voltage (V_{OC}) presented a high value (~ 1V). Moreover, it is possible to observe that the replacement of PEI with ZnO layer led to the suppression of S-kinks in the J-V characteristics showing an improvement of J_{SC} value and an unchanged V_{OC}.

The S-shaped phenomenon is still unclear but several explanations have been hypothesized. In particular, the main reason could be the existence of energy barriers at the electrodes [12, 13, 14] or it could be due to misalignment of electrode work functions. [15, 16, 17]

In this regard, two types of barriers can be distinguished: the *extraction* and *injection* barriers. The former implies that charges cannot leave the device due to a poor conductivity and/or a high energy barrier of interlayer and, in order to tackle this issue, the buffer layer should be more conductive and

thinner, or completely replacing it. On the other hand, the latter is related to misalignment of selective contact work function with active layer energy levels. [18]

In order to obtain more information about the type of barrier, planar heterojunction (PHJ) solar cells characterized by different ETL interlayers and by varying their thicknesses were built.

The J-V characteristics of laminated PHJ solar cells using different buffer layer (ETL) and by varying their thickness are depicted in Fig. 4.7.

Tab. 4.4 shows the photovoltaic parameters for the PHJ solar cells.

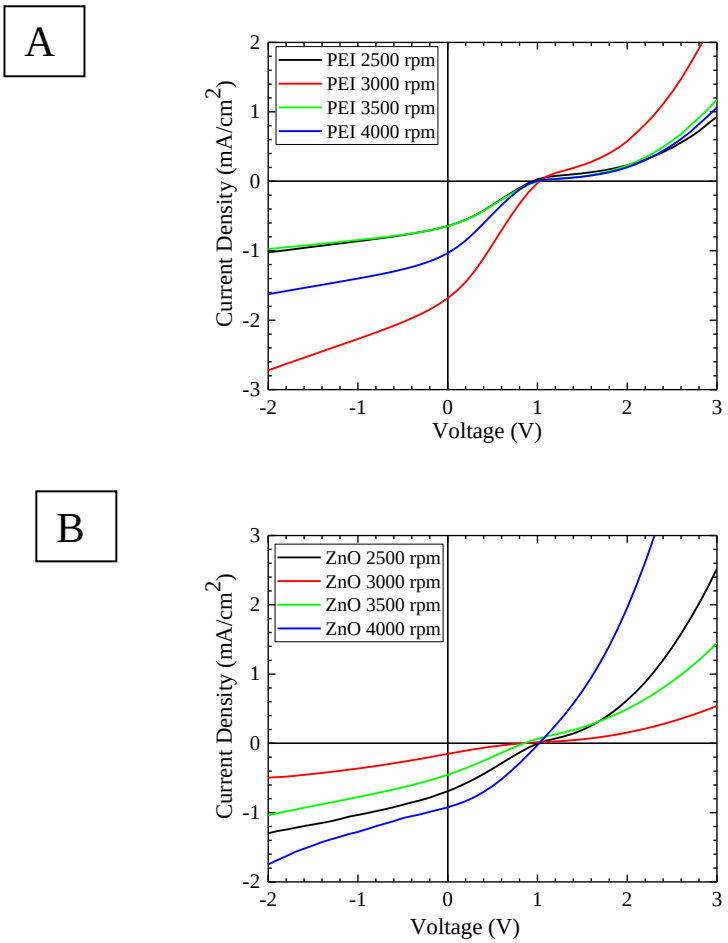

Fig. 4.7. The J-V characteristics of laminated PHJ solar cells fabricated by varying ETL layer and thickness. A) PEI as ETL layer; B) ZnO as ETL layer.

Tab. 4.4. Photovoltaic device parameters of laminated PHJ solar cells fabricated by varying ETL layer and thickness.

ETL	Spin Speed (rpm)	PCE (%)	FF (%)	J_{SC} (mA/cm^2)	V_{OC} (V)
PEI	2500	0.17	28	0.64	0.95
	3000	0.45	26	1.68	1.03
	3500	0.17	27	0.65	1.00
	4000	0.24	24	1.03	0.99
ZnO	2500	0.17	28	0.62	1.00
	3000	0.03	20	0.15	0.83
	3500	0.10	26	0.45	0.85
	4000	0.31	33	0.92	1.02

Once again, it can see that the incorporation of PEI as an ETL interlayer had the effect of creating a barrier inside the device and that the variation of thicknesses did not involve changes on S-shaped J-V curves. On the contrary, the S-kink suppression occurred for thinner layers when ZnO is used as ETL.

It is not easy to make a correct evaluation of the type of barrier, multiple factors and deeper characterizations should be considered. For instance, a direct method, useful for this purpose, could be to take into account the variation of thickness. [19] In particular, it has been shown that the donor or acceptor layer thickness can be correlated to injection barriers; on the

other hand, the interlayer (HTL or ETL) thickness can be associated to the extraction barrier.

According to this method and the reported data, it is reasonable to suppose that the performance of laminated binary solar cells may have been affected by an extraction barrier where the ETL layer thickness represents a limitation of the probabilities for charge carriers to cross the interface barrier. [18]

Summarizing, although both the ternary and the binary blends are optically promising thanks to an optimal match among materials absorption spectra, the devices were characterized by poor performance probably due to recombination phenomena or traps in the different layers or their interfaces. For a more fruitful understanding, further electrical and morphological investigations should be performed.

Bibliography of Chapter 4

[1] J. Huang, G. Li and Y. Yang, *Adv. Mater.* , vol. 20, p. 415–419 , 2008.

[2] J. Ouyang and Y. Yang, *Adv. Mater.* , vol. 18, p. 2141, 2006.

[3] Y. Yuan, Y. Bi and J. Huang, *Appl. Phys. Lett.* , vol. 98, p. 063306, 2011.

[4] M. Nakamura, C. Yang, E. Zhou, K. Tajima and K. Hashimoto, *ACS Appl. Mater. Interfaces,* vol. 1, p. 2703, 2009.

[5] M. Nakamura, C. H. Yang, K. Tajima and K. Hashimoto, *Sol. Energy Mater. Sol. Cells,* vol. 93, p. 1681, 2009.

[6] M. Granström, K. Petritsch, A. C. Arias, A. Lux, M. R. Andersson and R. H. Friend, *Nature* , vol. 395, pp. 257-260, 1998.

[7] J. B. Kim, Z. -L. Guan, E. P. S. Lee, M. F. Toney, A. Kahn and Y. -L. Loo, *Org. Electron. Phys. Mater. Appl.* , vol. 12, p. 1963–1972, 2011.

[8] J. Bergqvist, T. Österberg, A. Melianas, L. E. Aguirre, Z. Tang, W. Cai, Z. Ma, M. Kemerink, D. Gedefaw, M. R. Andersson and O. Inganäs, *npj Flex. Electr.* , vol. 2, no. 4, pp. 1-8, 2018.

[9] E. Wang, L. Hou, Z. Wang, S. Hellström, F. Zhang, O. Inganäs and M. R. Andersson, *Adv. Mater.,* vol. 22, p. 5240–5244, 2010.

[10] Z. Tang, A. Elfwing, A. Melianas, J. Bergqvist, Q. Bao and O. Inganäs, *J. Mater. Chem. A 3, (2015).,* vol. 3, p. 24289–24296, 2015.

[11] Y. Galagan, T. M. Eggenhuisen, M. J. J. Coenen, A. F. K. V. Biezemans, W. J. H. Verhees, S. C. Veenstra, W. A. Groen, R. Andriessen and R. A. J. Janssen, *J. Mater. Chem. A,* vol. 3, p. 20567–20578, 2015.

[12] W. Tress, K. Leo and M. Riede, *Advanced Functional Materials* , vol. 21, p. 2140–2149, 2011.

[13] W. Tress, A. Petrich, M. Hummert, M. Hein, K. Leo and M. Riede, *Applied Physics Letters 98 (2011)* , vol. 98, p. 063301, 2011.

[14] W. Tress, S. Pfuetzner, K. Leo and M. Riede, *Journal of Photonics for Energy* , vol. 1, p. 011114, 2011.

[15] J. Wang, X. Ren, S. Shi, C. Leung and P. Chan, *Organic Electronics*, vol. 12, p. 880–885, 2011.

[16] B. Ecker, H.-J. Egelhaaf, R. Steim, J. Parisi and E. v. Hauff, *Journal of Physical Chemistry C* , vol. 116, p. 16333–16337, 2012.

[17] A. Kumar, S. Sista and Y. Yang, *Journal of Applied Physics* , vol. 105, p. 094512, 2009.

[18] W. Tress and O. Inganäs, *Solar Energy Materials & Solar Cells*, vol. 117, p. 599–603, 2013.

[19] W. Tress, "Device physics of organic solar cells, Dissertation," TU Dresden, 2011.

CHAPTER 5

Hybrid Nanomaterials

5.1 Introduction

Nanoscience has gained a considerable resonance in the last decades attracting attention both from academia and industry. It is commonly defined as follows:

"Nanoscience is the study of phenomena and manipulation of material at atomic, molecular and macromolecular scales, where properties differ significantly from those at a larger scale". [1]

In fact, unlike macroscopic materials, nanostructured materials have a high percentage of surface atoms which strongly influence the overall properties. Therefore, their reactivity, structures, electronic states will be different compared to the bulk materials.

The great potentialities of nanomaterials can be useful for a widespread field of applications ranging from electronic devices, optics and photonics to biosensors, drug delivery, advanced catalysis, photovoltaics and energy conversion/ storage.

There are two approaches in the field of nanotechnology:

top-down approach (top-to-bottom): devices are fabricated from macroscopic materials through careful control of miniaturization processes at the atomic level;

bottom-up approach: materials and devices are built *via* self-assembly of small building blocks in a fast and simple way, exploiting molecular recognition principles (supramolecular chemistry).

According to the ‘bottom-up’ concept, the block copolymers (BCPs) represent an interesting type of materials due to their ability to self-assemble into highly ordered and thermodynamically stable nanostructures with controlled shapes and domain sizes.

In particular, the possibility to control the phase separation, designing precise molecular architecture makes the BCPs as ideal tools for the fabrication of hybrid nanomaterials for solar cells where the domain sizes can be conveniently tuned on the length scale as the diffusion length of an exciton.

Hybrid photovoltaics (PV) are part of third generation solar cells. In general, in hybrid solar cells an organic and an inorganic semiconductor material are combined in the active layer of the photovoltaic device.

The second part of the present thesis was focused on the study of block copolymers in order to create tailored organic nanostructures where the precise incorporation of inorganic semiconductor nanoparticles (NPs) is driven by the structuration of the matrix (structure-guiding host nanocomposites). [2] The BCP approach is an effective way to prevent self-aggregation of the nanoparticles, maximizing, at the same time, the surface area at the interface between the carriers of opposite charge in order to promote efficient exciton dissociation and charge transport processes.

5.2 Block copolymer architecture and general principles

As mentioned above, block copolymers (BCPs) have attracted a great interest in the field of nanotechnology [3, 4, 5, 6, 7, 8, 9, 10, 11] because of the capability to create self-assembly nanostructures having periodicity at nanometric scale.

Block copolymers are macromolecules consisting of two or more homopolymer subunits (blocks) covalently bonded together to form

structures with linear architecture (di-, tri-, multiblock copolymers) o no linear (mixed arm, starblock, or graft copolymers) (Fig. 5.1).

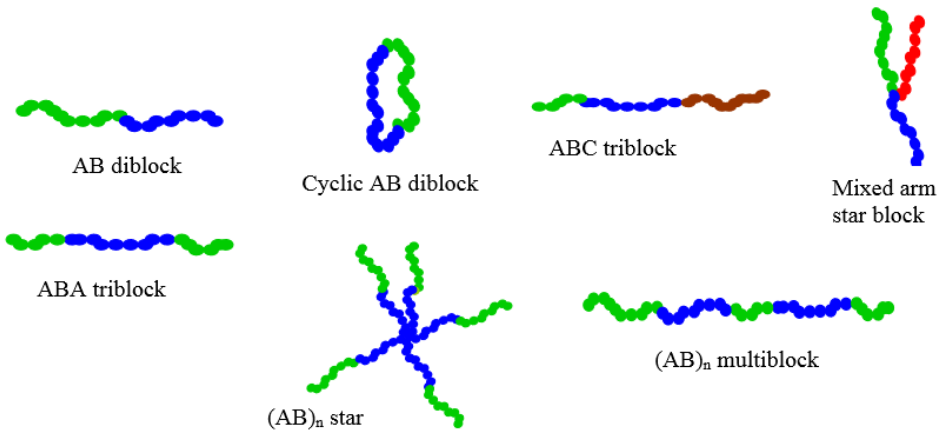

Fig. 5.1. Linear or not linear architectures of block copolymers.

The thermodynamic incompatibility of polymeric blocks determines the phase separation where the different macromolecules are spontaneously segregated in different microdomains (Fig. 5.2). These microdomains are highly ordered in a periodic arrangement whose sizes are directly dependent on the lengths and, therefore, on the molecular masses of the polymer chains. [12]

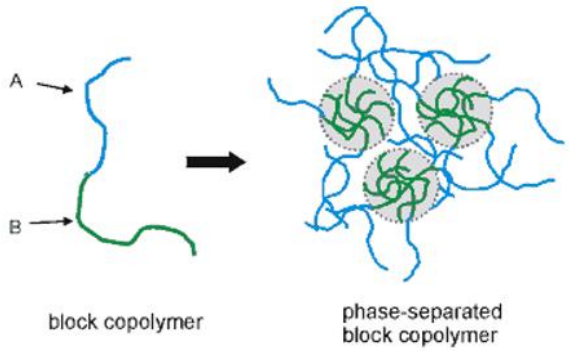

Fig. 5.2. Scheme of phase separated BCP.

This phenomenon is called "self-assembly" [13] and is due to the competition between the tendency to phase separation and the chemical connectivity between the polymeric chains forming, thus, periodic structures in order to minimize the contact between dissimilar blocks and, consequently, the free energy of the system.
The resulting morphologies are typified by a pattern of chemically distinct domains of periodicity in the 10-100 nm range.

5.3 Morfologies

The simplest architecture is the linear AB diblock copolymer which is the result of the covalent linkage of two homopolymers.
The common periodic morphologies are depicted in Fig. 5.3 A.

A

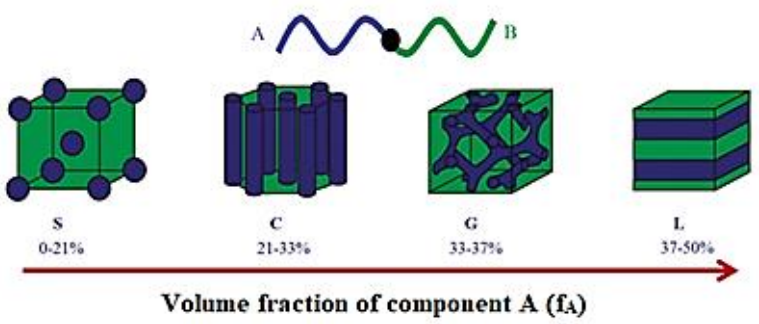

B

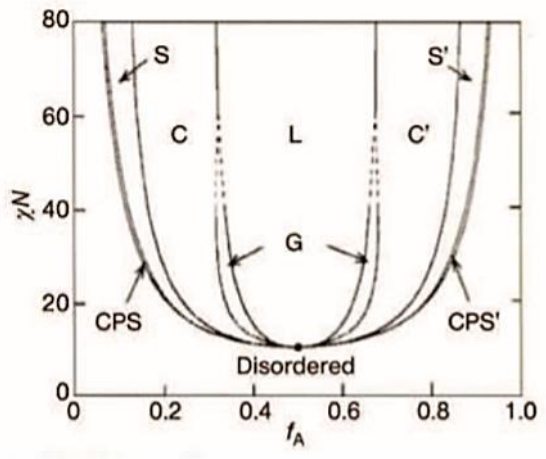

Fig. 5.3. A) Equilibrium morphologies from diblock copolymers (BCP) self-assembly. B) Theoretical phase diagram for linear AB diblock copolymers. Four equilibrium morphologies are predicted: spherical (S), cylindrical (C), gyroid (G), and lamellar (L), depending on the composition f_A and combination parameter χ N. χ is the Flory-Huggins interaction parameter and N is the degree of polymerization. [14]

The fundamental variables, useful to define resulting morphology and, thus, the self-assembly dynamics of BCP materials, are:

- the block volume fractions (f_A and f_B, where $f_A + f_B = 1$) dependent on the relative length of the blocks. [15, 16] In particular, f_A is given by the ratio between N_A and N, where N_A is the number of A monomers per molecule and N is the degree of polymerization.
- the polymer-polymer interaction parameter, known as Flory-Huggins χ, where the χ value quantifies the relative incompatibility between the polymer blocks and is inversely related to the temperature of the system. [17]

The possible morphologies are bodycentered cubic A spheres in a B matrix (spheres, S), hexagonally packed A cylinders in a B matrix (cylinders, C), bicontinuous gyroid (gyroid, G), and lamellae (L) and they are strictly

dependent on the total block length, the composition of the blocks and the strength of interaction between the blocks.

These four theoretical equilibrium morphologies can be mapped out on a phase diagram, as reported in Fig. 5.3 B [18]. It shows the relationship of $\chi.N$ versus f. Note that the phase segregation only takes place when the product χN exceeds some critical values; this event is known as *order-disorder transition* (ODT).

In particular, at low concentrations of A monomer, where $f_A << f_B$, the A blocks form spherical microdomains in a matrix of B (S). Increasing the volume fraction to $f_A < f_B$ leads to an increase in the connectivity of the microdomains, triggering the spheres to coalesce into cylinders that arrange on a hexagonal lattice (C). A roughly equal amount of both A and B blocks ($f_A \sim f_B$) will result in the formation of alternating layered sheets, or lamellae, of the A and B blocks (L). Any further increase in f_A ($f_A > f_B$), will cause the phases to invert, which means that the B block forms the microdomains in the matrix of A.

Therefore, by tuning the relative amount of A and the properties of each block (length and, consequently, the molecular masses), it is possible to control the dimensions of the microdomains and to create useful structures similar to those of crystalline materials, with the strong difference that the dimensions of the repetitive units and the periodicity are not of the order of angstrom, as in the crystals, but of nanometers.

For these reasons, the block copolymers represent an extremely versatile class of materials for a wide variety of applications.

5.4 Orientation of block copolymer morphologies on long range scale

The most practical applications of self-assembled block copolymers generally rely on thin film preparation to create a surface pattern on appropriate substrate for the realization of functional nanoscale devices.
However, the formation of equilibrium morphologies in diblock copolymers thin films depends on a delicate balance of many variables such as molecular weights, polydispersity, composition, the selectivity of the solvent for one block, surface interfacial interactions, and the interplay between structure periodicity and film thickness (optimal values usually are in the nanometric range).
All these variables can cause significant deviations from the predicted phases in the bulk state. Therefore, in order to achieve a perfectly ordered morphology, it is necessary a spatial and orientational control of BCP nanodomains. A long-range alignment of nanostructures can be obtained using different strategies, that can be classified into three different approaches. [19]

- Control of orientation by applying external fields, such as electric [20, 21], magnetic, thermal [22], mechanical [23, 24] and solvent evaporation [25, 18, 26].
- Modulation of substrate and surface interactions as a result of: preferential interaction of one block with the surface, neutralization of attractions to the substrate or to the surface [27, 28], epitaxial crystallization of domains onto a crystalline substrate, directional eutectic crystallization of a BC solvent, graphoepitaxy and 2-D geometric confinements.

- Induction of large-area ordering by facilitating the self-assembly, generally of thin films, using templates either topographically or chemically nanopatterned [29, 30].

The main methods used in the present work thesis will be described in the following sections.

5.4.1 Thermal annealing process

Thermal annealing is very simple and convenient process to favor the long-range orientation of BCP microdomains. It may anneal defects present in the samples reducing the interfacial tension between the two blocks and increasing the polymer mobility. The latter one is a relevant aspect especially for block copolymers containing a glassy block at room temperature such as polystyrene (PS). [31]

The treatment consists of controlled heating at a certain temperature (above the glass transition temperature (Tg) of the constituent blocks), preferably in an inert atmosphere or under vacuum, for a specific time.

Hashimoto et al. first applied zone annealing on BCPs thin films in order to create "defect free" samples with long-range order. [32, 33, 34]

Two different methods have been developed for orienting diblock copolymer:

- the Hot Zone Annealing (HZA): the sample is zone annealed above the order-disorder transition temperature T_{ODT}. The main drawback is that, for polymers with high molecular weights, the T_{ODT} usually has high value and it is not always accessible;
- the Cold Zone Annealing (CZA): this technique can be very efficient in enhancing the ordering kinetics in a BCP thin film using as maximum temperature a value larger than Tg but lower than T_{ODT}. [35]

5.4.2 Solvent vapor annealing (SVA)

Another approach to produce a long-range ordered film in amorphous and crystalline block copolymers is the solvent vapor annealing (SVA).

In this procedure, the order is produced by exposure the block copolymer film to vapors of one or more solvents in a sealed vessel.

Basically, the as-prepared BCP thin films are characterized by nonequilibrium, disorganized, and undefined structures. In order to control of the orientation of the microdomains in the microstructure of the BCPs, the mobility of the polymer chains has to be sufficient to allow for structural reorganization. In SVA process, the exposure and the subsequent solvent evaporation guarantee the proper polymer chains mobility forming more well-organized nanostructures.

Turturro *et al* [25] reported the first observation of lamellar and cylindrical microdomains in thin films perpendicular to the surface as a result of solvent evaporation and further investigated in more detail by Kim and Libera for a similar triblock copolymer. [18, 26]

They demonstrated that a perpendicular orientation of cylinders can be obtained for sufficiently high solvent evaporation rates. The choice of the solvent for SVA is critical, in particular, it should be a good solvent for both blocks, and that one block only is below its glass transition temperature at room temperature. It was noted that as the solvent evaporates, a concentration gradient front propagates through the film and the system passes through a disorder-order transition. The structure formed can be trapped if one block goes through its glass transition. A schematic representation of the proposed mechanism is reported in Fig. 5.4.

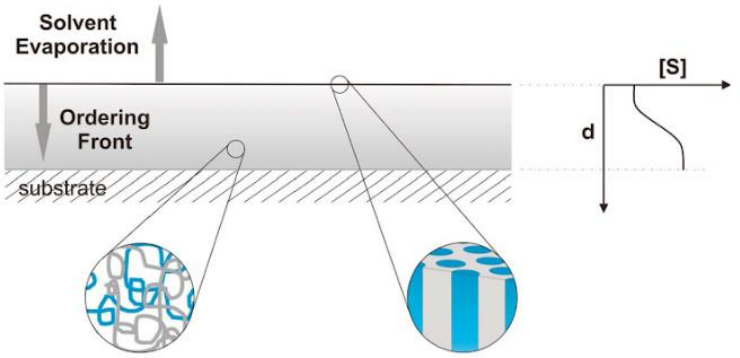

Fig. 5.4. Schematic of the solvent evaporation in a diblock copolymer thin film [36]. The diffusion produces a gradient in the concentration of the solvent, [S], as a function of depth, d, which induces an ordering front from the film surface to the substrate.

When there is the decrease in the solvent concentration, the BCP undergoes a transition from the disordered to the ordered state and, as the diffusion of the solvent produces a gradient of concentration along the thickness of the thin film, the ordering front rapidly propagates from the air surface to the substrate. The consequent decrease of Tg below room temperature, for at least one block, locks in the structures, which, due to the high directionality of the solvent gradient, are highly oriented normal to the surface. This behavior has been reported so far for films with thickness less than one-half micron, as for instance in the case of PS-PB systems, [25, 36] poly(styrene)-b-poly(ethylene oxide) (PS-b-PEO) [37, 38] poly(styrene)-b-poly(ferrocenyldimethylsilane) (PS-b-PFS). [39] However this mechanism holds to any BCPs having the Tg of one block above room temperature.

If both blocks are glassy, as in poly(styrene)-b-poly(methyl methacrylate) (PS-b-PMMA) diblocks, this effect is not observed. [18] [26]

5.4.3 Specific surface interactions

The alignment pathways in the microstructure of the BCP thin films can be obtained through the control of interactions between the BCP and the substrate. [19, 40]

The simplest interaction of a BCP film deposited on a substrate is the *preferential wetting* of one block at an interface to minimize interfacial and surface energies. As a consequence, a parallel orientation of microdomains, lamellae and cylinders is often induced at the interface and this orientation tends to propagate throughout the entire film. [41, 42, 43, 44, 45, 46, 47, 48, 49, 50] [51, 52, 53] The microstructure can be altered by variation of the film thickness on the substrate and preferential interactions of blocks with the substrate. [51, 52] Symmetric boundary conditions are established when one of the blocks preferentially interacts with both the substrate and the air surface, [47] while asymmetric conditions pertain when one block is preferentially wetted by the substrate and the other block by the superstrate. The control of orientation of the microdomains can also be achieved by confining a BCP between two surfaces; that is, adding a superstrate to a BCP film supported on a substrate. [54, 55, 56, 57] Strong or weak interactions of BCPs with the surfaces can be created by coating the surface walls with a homopolymer or a random copolymer, respectively, containing the same chemical species as the confined BCP. [56] In the case of a neutral surface, for example, by using a random copolymer, the lamellar microdomains rearrange themselves so that the direction of periodicity is parallel to the substrate. [56] [58, 59, 60] Moreover, decreasing the confined film thickness – that is, creating a large incompatibility strain of the natural domain period of the BC and the film thickness – induces a heterogeneous in - plane structure where both parallel

and perpendicular lamellae are located near the confining substrate. [57] Various theoretical studies have predicted the structural behavior of BCP thin films in a confined geometry [61, 62, 63, 64, 65, 66, 67, 68, 69, 70] and are basically consistent with experimental results.

5.5 Applications of block copolymers

Over the last few years, the block copolymers have gained a considerable importance for their potential applications in advanced technologies, such as information storage, drug delivery, photonic crystals, etc. (Fig. 5.5)
The scientific and industrial interest derives from the BCPs ability to self-assemble, in bulk or in thin films, into ordered nanostructures, with sizes in the nanometric range. By tuning the molecular weight, chemical structure, molecular architecture, and composition of block copolymers, the characteristics of these nanostructures can be manipulated.

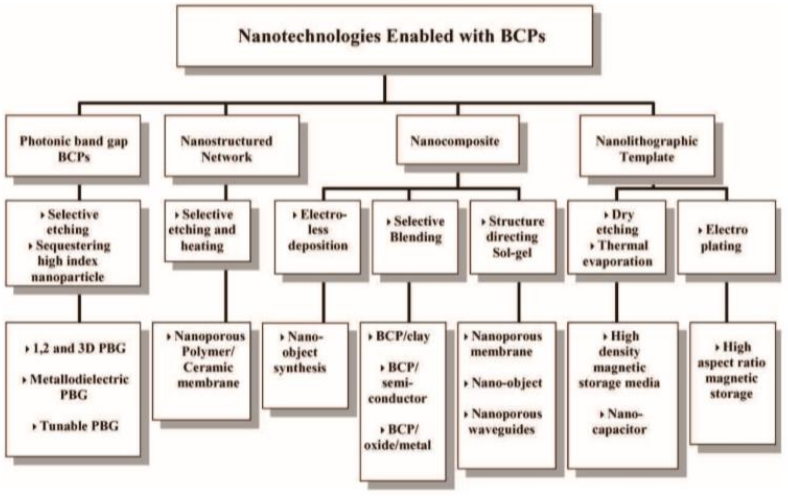

Fig. 5.5. Schematic representation of nanotechnologies enabled with BCPs. [3]

The promising role of ordered BCP morphology for photovoltaic applications was demonstrated in ref [71] by Cohen et al., where CdS nanoparticles (NPs) were included in both a microphase-separated and non-

microphase-separated triblock copolymer consisting of a polynorbornene block with pendent hole-transporting carbazole groups, a short mid-block capable of binding semiconductor NPs, and a polynorbornene block functionalized with electron-transporting groups. It was shown that the selective inclusion of CdS NPs in the middle block domains of the microphase separated morphology enhances the performance of the photovoltaic device. Furthermore, it was also demonstrated that energy transfer from carbazole moieties present in one block of the BCP could be transferred to CdS NPs sequestered in the middle block, indicating that the nanostructured polymeric substrate can be successfully used to tune energy-transfer processes. [71, 72]

Moreover, lamellar-forming poly(styrene)-b-poly(methyl methacrylate) (PS-b-PMMA) copolymer was successfully used to selectively sequester and confine different surface-functionalized inorganic nanoparticles and nanorods (NRs) in lamellar PMMA domains, such as poly(methyl methacrylate) (PMMA)grafted magnetite (FeO_4) NPs [73] and gold NRs modified with a poly(ethylene glycol) (PEG) brush. [74]

The following sections will focus mainly on two specific nanotechnological strategies enabled with BCPs thin films to pursue the purpose of thesis: the use of BCPs as tool to obtain composites with selective inclusion of *n*-type ZnO NPs into a specific polymer block and, at same time, the fabrication of nanoporous templates, through the selective removal of sacrificial polymer block from self-assembled matrix, to favor the incorporation of *p*-type CdSe NPs.

5.5.1 Block copolymer-based nanocomposites

The nanocomposites are a class of composite materials constituted by a polymer matrix and nanoparticles, called *nanofillers*.

The term nanoparticle usually is referred to a particle formed by atomic or molecular aggregates with a diameter on the scale of nanometers.

Generally, the composites are not characterized by any significant interaction at the interface between the polymer and the filler limiting, thus, the performance of the resulting material.

On the other hand, in the nanocomposites the nanoparticles will be characterized by extremely large surface/volume ratios and it means that there will be a strong enhancement in surface effects with subsequent advantages in terms of unique electronic, optical and catalytic properties; this phenomenon is known as *nanoeffect*. [75, 76]

Many methods for the fabrication of nanomaterials have been proposed, mainly to meet the demand of microelectronic industries, ranging from milling techniques to non-traditional photolithographic and chemical methods, with a strong prevalence of methods based on template synthesis.

Effective fabrication of a two-dimensional array of nanoparticles on solid substrates has been demonstrated by the utilization of block copolymers (BCPs) in a self-assembled arrangement. [2]

Nanodomains of self-assembled BCPs may act as hosts for sequestering nanofillers producing nanocomposites with different morphologies [2] (Fig 5.6). The size and shape of the NPs containing nanodomains may be conveniently tuned by changing the molecular weights and compositions of the BCPs. [77, 78]

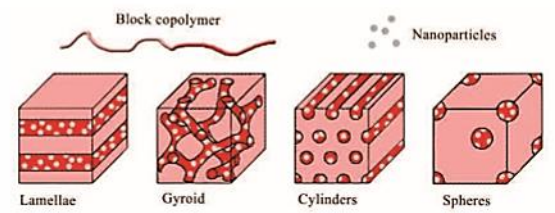

Fig. 5.6. Nanodomains generated from BCPs (lamellae, gyroid, cylinders or spheres) may act as hosts for sequestering guest nanoparticles (NPs), to obtain nanocomposites where the distribution of the NPs is guided by the ordering of the BCP matrix.

Usually, two synthetic approaches are used for the preparation of nanocomposites based on BCP matrix:

a) *ex*-situ synthesis of nanoparticles that are surface-tailored in order to allow preferential sequestering within a target domain of the BCP matrix;

b) *in*-situ synthesis of inorganic particles within a BCP domain that is preloaded with a suitable precursor, generally a salt of a metal.

The employment of nanostructures from block copolymers is one of the most promising ways to locate nanoparticles in a controlled way on solid substrates. The key for the engineering of these materials is the ability to control the final morphology of BCP nanostructures and to achieve a selective infiltration of nanoparticles in the target nanodomains. The possible outlooks linked to the development of such materials depend strictly on the kind of new proprieties that could emerge from the presence of long-range order of the nanoparticles, taking advantage of both the physical properties of the polymeric matrix and the nanospecific characteristics of the added component.

5.5.2 Block copolymer-based nanoporous materials

Another simple, flexible and highly versatile approach to fabricate hybrid nanocomposites is represented by the possibility to create nanoporous matrices where the semiconductor nanoparticles are selectively backfilled. In this regard, diblock copolymers are promising and useful materials. [79] In fact, by using BCP-based nanostructures, one polymeric component can be selectively removed (etched) and, thus, a large variety of nanoporous organic materials can be obtained (Fig. 5.7).

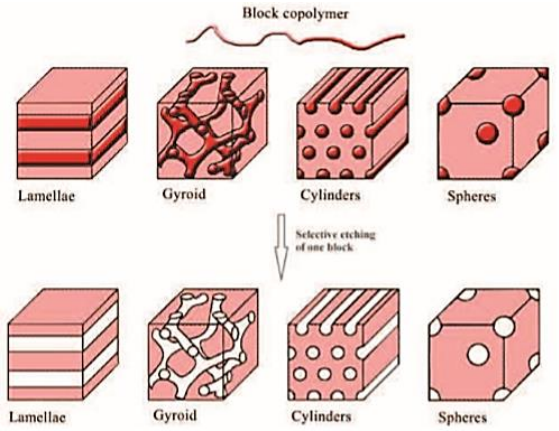

Fig. 5.7. Nanoporous materials can be generated by selective removal of one component (etching) from a self-assembled block copolymer. The resulting porous material will exhibit the pore size and pore topology of their parent structures.

There are two key requirements for preparing nanoporous materials from ordered block copolymers:

a) the etchable polymeric block must be physically accessible to the solvent, reagent, process utilized for degradation;

b) the matrix material must be able to support the resultant nanoporous structure.

Significant examples of BCP-based nanoporous materials were reported by Hashimoto et al. [80]. They studied a blend constituted by a poly(styrene)-b-poly(isoprene) (PS-b-PI) copolymer and an homopolymer (polystyrene). The role of the homopolymer was of tuning the volume fraction of polystyrene, thus obtaining the desired microstructure, that is the gyroid phase.

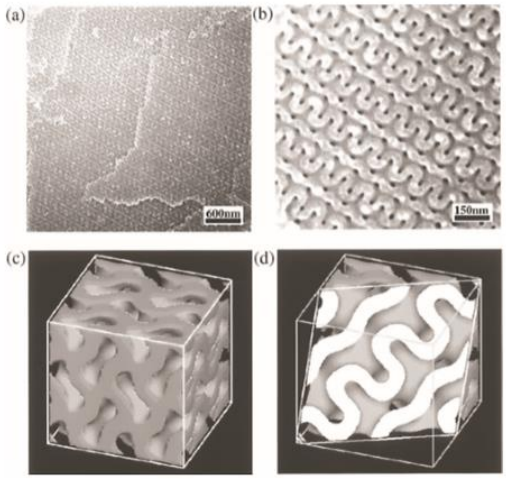

Fig. 5.8. Nanoporous membrane from an etched BCP gyroid structure. SEM micrographs showing a bicontinuous nanochannel in the matrix of PS with two different magnifications (parts a and b) and computer graphics of the double gyroid network (c) a three-dimensional view and (d) a two-dimensional intersection cut along the [211] direction. [80]

Then, the ozonolysis treatment was applied to remove the polyisoprene domains from the obtained nanostructure leading to the formation of a three-dimensionally porous continuous material. (Fig. 5.8) The symmetry of the precursor material was nearly identical to the resultant porous material.

Another literature example [81] concerns the control of the feature pores size by varying BCP molecular weight, as shown in Fig. 5.9.

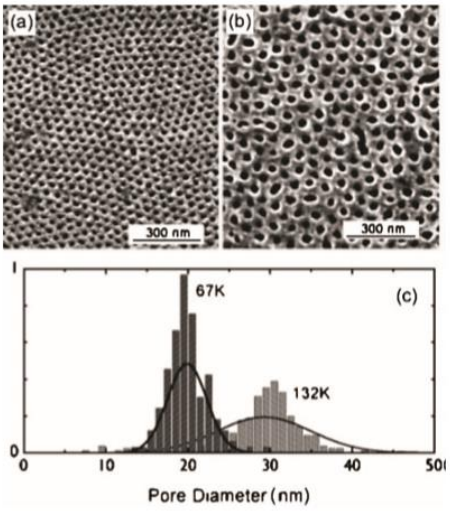

Fig. 5.9. SEM image of nanoporous PS materials resulting after the selectively removal of PMMA phase from a 67 kg mol^{-1} (a) and 132 kg mol^{-1} (b) PS-b-PMMA thin film. (c) pore diameter histograms. [81]

In particular, it was investigated the effect of block copolymer molecular weight on the porous structure resulting from the selective etching of a cylinder-forming PMMA phase in an ordered BCP matrix based on poly(styrene)-b-poly(methyl methacrylate) (PS-b-PMMA). Using a block copolymer of higher molecular weight (from 67 kg mol^{-1} to 132 kg mol^{-1}), it was shown a variation in the pores dimension of about 10 nm (Fig. 5.9c). The ability to control and to manipulate the design and synthesis of nanoporous materials allows to use BCPs as host matrix for the selective inclusion of NPs in specific nanodomains according to well-defined geometries. Different strategies have been investigated to introduce the NPs into nanoporous template in a facile way.

Spin coating inorganic nanoparticles is an attractive approach for generating functional features in the nanomaterials.

Darling et al. [82] demonstrated a novel route for the infiltration of magnetic FePt nanoparticles on vacuum ultraviolet etched PMMA half-cylinder domains in PS-b-PMMA system (Fig. 5.10). The etched PMMA domains provided a porous matrix for the selective incorporation of functionalized FePt nanoparticles.

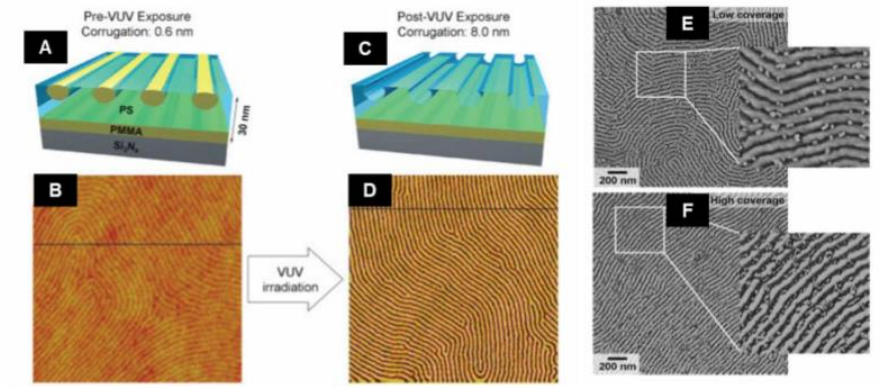

Fig. 5.10. A) and C) schematic representations of PS-b-PMMA films before and after vacuum ultraviolet (VUV) irradiation for selective etching of the surface PMMA half-cylinders; B) and D) are corresponding AFM images. Following spin-coating method for selective inclusion of FePt nanoparticles into photochemically altered PMMA domains: low coverage (E) and high coverage (F) areas of nanoparticle clusters into PMMA nanochannels. [82]

5.6 Materials

5.6.1 BCP samples

In this PhD thesis block copolymers samples were employed as templating agent for the subsequent addition of the inorganic material. In particular, two type of block copolymers with lamellar morphology were used. They are poly(styrene)-b-poly(methyl methacrylate) (PS-b-PMMA) and poly(styrene)-b-poly(4-vinylpiridine) (PS-b-P4VP). Both samples were purchased from the Polymer Source Inc.

5.6.1.1 PS-b-PMMA

The BCP sample presents amorphous blocks of polystyrene (PS) and polymethylmethacrylate (PMMA). The main characteristics are reported in Tab. 5.1.

Tab. 5.1. Number average molecular weight (M_n) and polydispersity index of the molecular masses (PDI = M_w/M_n).

BCP	**M_n (PS-b-PMMA) (kDa)[a]**	**M_w/M_n[a]**	**f_{PS} (%)**	**Morphology**
PS-b-PMMA	25.0/26.0	1.06	52	Lamellar

[a)] Obtained by SEC analysis

The chemical structure is depicted in Fig. 5.11:

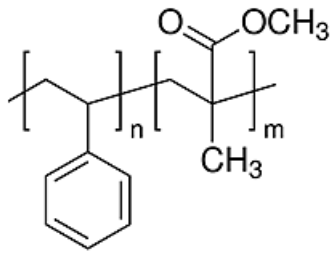

Fig. 5.11. Structure of the diblock copolymer PS-b-PMMA.

Poly(styrene)-b-poly(methylmethacrylate) is prepared by living anionic polymerization. Living anionic polymerization was early described and illustrated by Szwarc and co-workers in 1956. [83] Their initial work was based on the polymerization of styrene and dienes. The polymerization proceeds through the highly reactive carbanion chain end, usually created by an alkyl lithium initiator such as sec-BuLi or n-BuLi. Due to the high reactivity of the chain end with other compounds, extremely stringent conditions must be met in order to avoid unwanted side reactions. In some

cases, such as the polymerization of acrylates, the reactions must be carried out at very low temperatures (−78 °C) in order to avoid terminating side reactions such as intrachain cyclization or “backbiting”, caused by the reaction of the anionic center with a carbonyl group on the monomer. Living anionic polymerization, especially alkyllithium initiated polymerizations, provides convenient and reliable procedures for synthesis of well-defined block copolymers with controlled molecular weight, narrow molecular weight distribution and low degrees of compositional heterogeneity. Poly(styrene)-b-poly(methylmethacrylate) is generally synthesized in THF at –78 °C using sec. BuLi initiator in the presence of LiCl. Polystyrene macroanions were end capped with a unit of diphenyl ethylene (DPE) before adding methylmethacrylate (MMA) monomer. The molecular weight and polydispersity index (PDI) of the block copolymer were characterized by size exclusion chromatography (SEC). The polymer is soluble in THF, $CHCl_3$, toluene, dioxane.

5.6.1.2 PS-b-P4VP

PS-b-P4VP is an amorphous and amphiphilic diblock copolymer. The main characteristics are reported in Tab. 5.2.

Tab. 5.2. Number average molecular weight (M_n) and polydispersity index of the molecular masses (PDI = M_w/M_n).

BCP	**M_n (PS-b-P4VP) (kDa)[a]**	**M_w/M_n[a]**	**f_{PS} (%)**	**Morphology**
PS-b-P4VP	22.5/29.0	1.2	61	Lamellar

[a)] Obtained by SEC analysis

The chemical structure is displayed in Fig. 5.12:

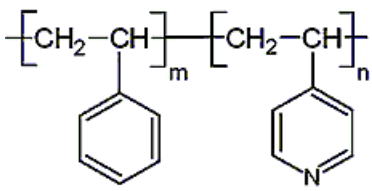

Fig. 5.12. Structure of the diblock copolymer PS-b-P4VP.

Generally, poly(styrene)-b-poly(4-vinylpiridine) is prepared by living anionic polymerization in THF or THF–DMF solvent mixtures at –78°C. Polystyrene macroanions were end capped with a unit of diphenyl ethylene (DPE) before adding 4-vinylpyridine (4VP) monomer. Copolymer PDI is determined by SEC.

The polymer is soluble in DMF, $CHCl_3$ but also in THF depending on its chemical composition.

5.6.2 Nanoparticles (NPs)

Semiconductor nanoparticles, also known as quantum dots, are a promising alternative to traditional semiconductors as the light harvesting element in a photovoltaic device, due to several advantageous properties for the conversion of solar light into energy.

The quantum dots exhibit the so-called quantum confinement. This effect is essentially due to a change of electronic and optical properties when the material is of sufficiently small size, typically 10 nanometers or less. As the size decreases a blue shift of the bandgap appears. If the size approaches a critical quantum measurement, called the exciton Bohr radius, the particle becomes more like an atom, its energy levels becoming discrete rather than forming continuous bands (Fig. 5.13). As result of the quantum confinement, due to the increasing in the bandgap, the onset of the optical

absorption and the maximum of the emission spectra are shifted to higher energies with decreasing the size of the nanoparticles. [84, 85, 86]

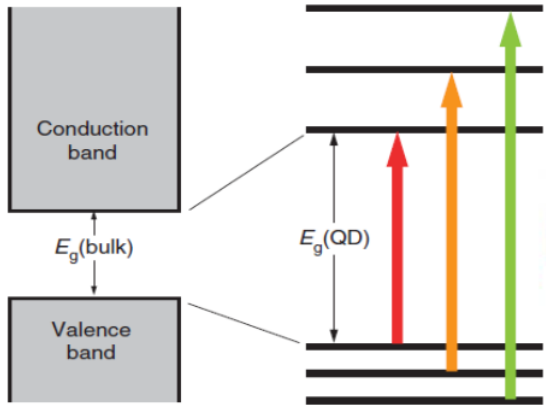

Fig. 5.13. Schematic representation of the discrete energy level diagram of a quantum dot compared to band energy diagram of a bulk semiconductor.

In the present PhD activity, the used inorganic components were the zinc oxide (ZnO) NPs covered with a mixture of *n*-hexadecylamine (HDA) and *tert*-butylphosphonic acid (TBPA) as *n*-type semiconductor and the cadmium selenide (CdSe) NPs capped by *2*-mercaptoethanol as *p*-type semiconductor material. These functional groups were selected to favor the selective inclusion in nanodomains of the BCP-based nanocomposites, due to the chemical affinity.

5.6.2.1 ZnO nanoparticles

ZnO is an attractive material for short wavelength optoelectronic applications owing to its wide band gap 3.37 eV, large bond strength, and large exciton binding energy (60 meV) at room temperature. As a wide band gap material, ZnO is used in solid state blue to ultraviolet (UV) optoelectronics, including laser developments. In addition, due to its non-centrosymmetric crystallographic phase, ZnO shows the piezoelectric

property, which is highly useful for the fabrication of devices, such as electromagnetic coupled sensors and actuators. [87]

Crystalline ZnO has a wurtzite (B4) crystal structure at ambient conditions. The ZnO wurtzite structure has a hexagonal unit cell and belongs to the space group of $P6_3mc$. Fig. 5.14 clearly shows that the structure is composed of two interpenetrating hexagonal closed packed (hcp) sublattices, in which each consist of one type of atom (Zn or O) displaced with respect to each other along the threefold *c*-axis. It can be simply explained schematically as a number of alternating planes stacked layer-by-layer along the *c*-axis direction and composed of tetrahedrally coordinated Zn^{2+} and O^{2-}. The tetrahedral coordination of ZnO gives rise to the non-centrosymmetric structure. In wurtzite hexagonal ZnO, each anion is surrounded by four cations at the corners of the tetrahedron, which shows the tetrahedral coordination and hence exhibits the sp^3 covalent-bonding. The detailed properties of ZnO are presented in Tab. 5.3.

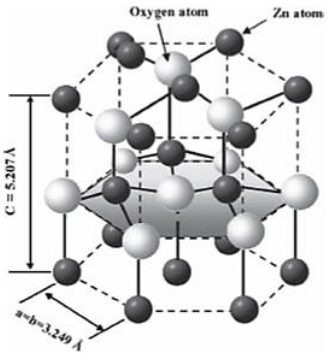

Fig. 5.14 The hexagonal wurtzite structure model of ZnO. The tetrahedral coordination of Zn-O is shown. O atoms are shown as larger white spheres while the Zn atoms are smaller dark grey spheres.

Tab. 5.3. Physical properties of wurtzite ZnO.

Properties	**ZnO**
Lattice parameters at 300 K	
a_0 (nm)	0.325
c_0 (nm)	0.521
c_0/a_0	1.602 (1.633*)
Density (g/cm^3)	5.606
Stable phase at 300 K	Wurtzite
Melting point (°C)	1975
Thermal conductivity (Wcm^{-1}K^{-1})	0.6, 1-1.2
Refractive index (n_D)	2.008
Band gap (RT)	3.370 eV
Exciton binding energy (meV)	60
Electron effective mass	0.24
Electron Hall mobility at 300 K (cm^2/Vs)	200
Hole effective mass	0.59
Hole Hall mobility at 300 K (cm^2/Vs)	5-50

*The value in parenthesis reflects the ideal ratio c_0/a_0 for a perfectly ideal hexagonal packing of O species.

In the present thesis and in the collaboration with CNR (National Research Centre) of Bari (Italy), ZnO nanocrystals were synthetized by the thermal decomposition of zinc acetate ($ZnAc_2$) in a high-temperature coordinating mixture of a long-chain alkylamine (*n*-hexadecylamine, HDA) and *tert*-butylphosphonic acid (TBPA). The variation of the TBPA/$ZnAc_2$ molar ratio allows the tuning of the nanocrystal size in the range 2-7 nm. In this method, the addition of the phosphonic acid is important in relation to its effectiveness in directing ZnO crystal growth in the quantum confinement regime. The role of the surface in the emission properties of the

nanoparticles and the stability of amine/TBPA-coated ZnO nanocrystals are also important.

ZnO nanocrystals were directly grown in alkylamine by slowly heating the reaction mixture to high temperatures according to the following procedure: a mixture of $ZnAc_2$, HDA, and TBPA, with TBPA/$ZnAc_2$ molar ratio fixed equal to ~0.6, was degassed under vacuum for 1 h at 110°C under vigorous stirring. Then, the reaction vessel was slowly heated up to 300 °C under nitrogen flow to induce the decomposition of $ZnAc_2$. Heating was stopped when the solution became cloudy and the temperature was dropped down to 80°C. The NPs were collected from the reaction mixture in air by addition of methanol (non solvent) to the reaction mixture at 50°C. The resulting precipitate was isolated by centrifugation and was washed twice with methanol to remove residual surfactants. The surfactant (i.e., HDA/TBPA) coated ZnO nanoparticles was, then, easily dissolved in toluene to give optically clear solutions.

5.6.2.2 CdSe nanoparticles

The cadmium selenide (CdSe) presents three crystalline forms: sphalerite, wurtzite and rock salt.

The structure of the sphalerite is unstable and turns into wurtzite through a thermal transition that starts at T ~130 °C and is completed at T ~700°C. The salt rock form, on the other hand, is observed only at high pressures.

The most stable structure under standard conditions is the wurtzite type. It belongs to the space group $P6_3mc$ and is characterized by a hexagonal unit cell consisting of Se^{2-} and Cd^{2+}. In particular, each anion is surrounded by four cations, arranged at the vertices of a tetrahedron and vice versa (Fig. 5.15).

Tab. 5.4 summarizes some characteristic parameters of the crystalline structure.

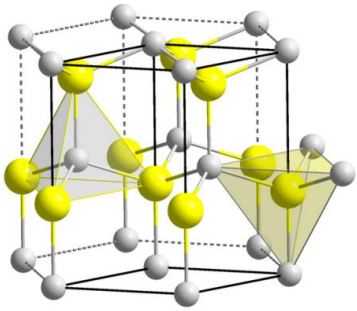

Fig. 5.15 The hexagonal wurtzite structure model of CdSe. The tetrahedral coordination of Zn-O is shown. Cd atoms are shown as larger yellow spheres while the Se atoms are smaller grey spheres.

Tab. 5.4. Physical properties of wurtzite CdSe.

Properties	**CdSe**
Lattice parameters at 300 K	
a_0 (nm)	0.431
c_0 (nm)	0.702
c_0/a_0	0.163
Density (g/cm^3)	5.81
Stable phase at 300 K	Wurtzite
Melting point (°C)	1268
Thermal conductivity (Wcm^{-1}K^{-1})	0.09
Refractive index (n_D)	2.5
Band gap (RT)	1.714 eV
Exciton binding energy (meV)	15
Electron effective mass	$m_n = 0.12\ m_0$
Hole Hall mobility at 300 K (cm^2/Vs)	40

The synthesis of Cadmium Selenide nanocrystals (CdSe) was based on thermal decomposition of organometallic precursors at high temperatures in the presence of three different coordinating agents: triottylphosphine

oxide (TOPO), *tert*-butylphosphonic acid (TBPA) and *n*-hexadecylamine (HDA). Subsequently, a process of exchange of ligands with *2*-mercaptoethanol (ME) was carried out to functionalize, in this way, the surface of the nanoparticles. Finally, the NPs were suspended in two different organic solvents such as dimethylsulfoxide (DMSO) and dimethylformamide (DMF).

5.7Methods

5.7.1 Structural and thermal analyses

5.7.1.1 Wide angle X-ray scattering (WAXS)

X-rays diffraction patterns of the analyzed samples were obtained by a Philips automatic powder diffractometer, using the Cu Kα (nickel-filtered) radiation. The diffraction patterns were registered scanning continuously the diffraction angle 2θ at a rate of 0.1°(Δ2θ)/10s (Δt).

5.7.1.2 Thermal analysis

Thermal analysis was performed by differential scanning calorimetry (DSC), in order to detect the glass transition temperature. DSC Mettler-822 calorimeter was used with the intra cooler system. Few milligrams of the sample were thermally scanned, under nitrogen flow, in an appropriate temperature range. The sample was first heated to a temperature above its melting point, then quenched and finally heated once again until melting. From the DSC curves of the thermal cycle, the temperature of first heating, crystallization and second heating were obtained. The sample was heated at a constant rate of 10°C/min.

5.7.2 Morphological analysis

5.7.2.1 Transmission electron microscopy (TEM)

The transmission electron microscope (TEM) is a very powerful tool for material science.

It works on the same basic principles as the optical microscope with the key difference that it uses electrons instead of light. Because the wavelength of electrons is much smaller (0.03 Å) than that of light (λ> 1000 Å), an optimal resolution, higher of many orders of magnitude than that from a light microscope, is obtained for TEM images.

A schematic representation of a transmission electron microscope TEM is shown in Fig. 5.16.

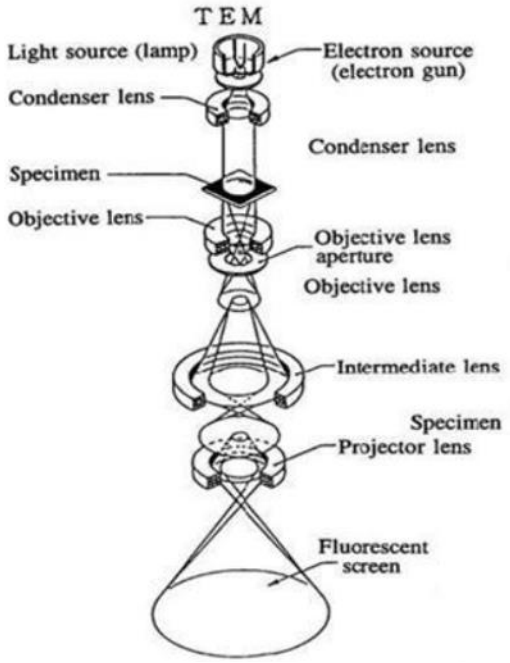

Fig. 5.16. Schematic Representation of a transmission electron microscope (TEM).

During TEM analysis, the electrons are generated by an emission gun using a high electrostatic field, which results in high source brightness and a coherent beam with a small energy spread. The electron beam is accelerated up to 200 keV and travels through a complex series of electromagnetic lens that allow to adjust the path of the deflected electrons in direction of the main axis of the electron beam under high-vacuum. The interaction between the electrons and the thin specimen produces the scattering or transmission events. The image is reconstructed in the image plane of the objective lens onto the fluorescent viewing screen, an electron sensitive film or a CCD camera. In this way, it is possible to obtain all the structural information of the sample.

The thickness of the sample plays a key role. In fact, it should be ultra-thin (from 5 to 500 nm) since the electrons have to be efficiently transmitted through the specimen.

In this PhD activity, thin films of samples were backed with a carbon film, floated off on water with the help of a poly(acrylic acid) backing, mounted on copper grids and analysed by TEM. Grids (200 mesh copper grips purchased from Aldrich) underwent to a staining process with RuO_4 in order to increase the overall contrast among the areas in the sample characterized by different density or thickness. This process consists in exposing the grids to vapors originated from an aqueous solution of RuO_4. The preparation of the solution of RuO_4 consists of dissolving in a flask at room temperature 1g of sodium periodate ($NaIO_4$) in 25 mL of distilled water. The solution changes from transparent to whitish and is placed in a water/ice bath to lower the solution temperature to 1-5°C. Once that this temperature is reached 0.15 g of ruthenium oxide (RuO_4) are added to the solution. Finally, the flask containing the solution is removed from the water/ice bath and stirred avoiding light exposure for about 3-4 hours. TEM

images have been obtained by a Philips EM 208S microscope operating at a voltage of 100kV (point resolution of 0.3 nm) available at C.I.S.M.E. (Centro Interdipartimentale di Servizio per la Microscopia Elettronica) and by using FEI TECNAI G2 microscope operating at a voltage of 200 kV available at Chemical Sciences Department of the University of Naples "Federico II".

5.7.2.2 Atomic Force Microscopy (AFM)

Atomic Force microscopy (AFM) is one of the most versatile forms of microscopy for the characterization of physical properties such as morphology, [88] electrical, [89] mechanical, [90] magnetic, [91, 92] electrochemical, [93] and many other properties at the nanoscale. AFM uniquely offers higher resolution imaging capabilities owing to piconewton force sensitivity and nanometer positional accuracy. [94, 95]

In the AFM, the sample surface is scanned with a probe consisting of a sharp nanometer-sized probe situated at the end of a cantilever. The latter one is typically silicon or silicon nitride with a tip radius of curvature on the order of nanometers. When the tip is brought into proximity of a sample surface, forces between the tip and the sample lead to a deflection of the cantilever according to Hooke's law.

In Fig. 5.17 the AFM representation is reported. Typically, a laser beam focused on the cantilever is reflected onto a four-quadrant photodetector with the pairs of sectors arranged to detect bending deflection, bending oscillation, and torsion of the cantilever. Additionally, a piezoelectric scanner controls sub-nanometer movements in the x, y, and z dimensions, then images are compiled line-by-line as the sample is raster scanned

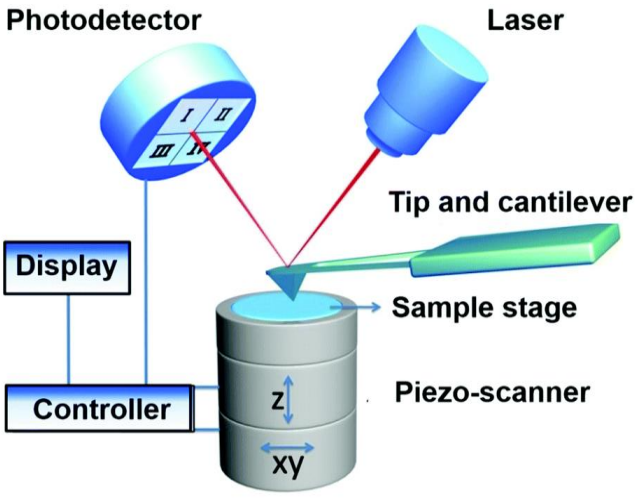

Fig. 5.17. Schematic Representation of an Atomic Force microscopy (AFM). [96]

The AFM analysis can be operated in a number of modes, depending on the application. In general, possible imaging modes are divided into static (also called contact) modes and a variety of dynamic (non-contact or "tapping") modes where the cantilever is vibrated. The AFM images reported in this PhD thesis were obtained at room temperature by a Bruker MultiMode 8 microscope and were performed in tapping mode.

Silicon probes having a tip nominal radius of curvature of 8 nm, with a force constant of 42 N/m were used. The resonance frequency was about 320 kHz with a scan rate of 1 Hz s^{-1}. The sample line was 256 or 512. In tapping mode, the tip of the cantilever does not contact the sample surface. The cantilever is instead oscillated at a frequency slightly above its resonant frequency where the amplitude of oscillation is typically a few nanometers (<10 nm). The van der Waals forces, which are strongest from 1 nm to 10 nm above the surface, or any other long-range force which extends above the surface acts to decrease the resonance frequency of the cantilever. This decrease in resonant frequency combined with the feedback loop system maintains a constant oscillation amplitude or

frequency by adjusting the average tip-to-sample distance. Measuring the tip-to-sample distance at each (x, y) data point allows the scanning software to construct a topographic image of the sample surface. Non-contact mode AFM does not suffer from tip or sample degradation effects that are sometimes observed after taking numerous scans with contact AFM. This makes non-contact AFM preferable to contact AFM for measuring soft samples.

Bibliography of Chapter 5

[1] "The Royal Society & The Royal Academy of Engineering," 2004. [Online]. Available: http://www.nanotec.org.uk/report/Nano%20report%202004%20fin.pdf.

[2] M. R. Bockstaller, R. A. Mickiewicz and E. L. Thomas, *Adv. Mater.* , vol. 17, p. 1331, 2005.

[3] C. Park, J. Yoon and E. L. Thomas, *Polymer* , vol. 44, p. 6725, 2003.

[4] G. Krausch and M. R., *Adv. Mater.*, vol. 14, p. 1579, 2002.

[5] H. I. W., *Angew. Chem.*, vol. 42, p. 1692, Int. Ed. 2003.

[6] M. Lazzari and M. A. Lopez-Quintela, *Adv. Mater.*, vol. 15, p. 1583, 2003.

[7] W. Lu and A. M. Sastry, *IEEE Trans. Semicond*, vol. 20, p. 421, 2007.

[8] C. J. Hawker and T. P. Russell, *MRS Bull.*, vol. 30, p. 952, 2005.

[9] H. Kim and W. D. J. Hinsberg, *Vac. Sci. Technol., A* , vol. 26, p. 1369, 2008.

[10] S. B. Darling, *Prog. Polym. Sci.* , vol. 32, p. 1152, 2007.

[11] W. van Zoelen and t. B. G., *Soft Matter*, vol. 5, p. 1568, 2009.

[12] T. Hashimoto, M. Shibayama and H. Kawai, *Macromolecule*, vol. 13, p. 1237, 1980.

[13] J. H. Bruning and P. S. P.-O. Eng., *Proc. Soc. Photo-Opt. Eng*, vol. 6520, p. 6520041, 2007.

[14] F. S. Bates and G. Fredrickson, *Phys. Today* , vol. 52, p. 32, 1999.

[15] F. S. Bates and G. H. Fredrickson, *Annu. Rev. Phys. Chem.*, vol. 41, p. 525, 1990.

[16] L. Leibler, *Macromolecules* , vol. 13, p. 1602, 1980.

[17] T. P. Lodge, *Macrom. Chem. and Phys.*, vol. 204, pp. 265-273, 2003.

[18] G. Kim and M. Libera, *Macromolecules;*, vol. 31, p. 2569, 1998.

[19] M. Lazzari and C. D. Rosa, Advanced nanomaterials, Chapter 4, K. E. Geckeler and H. Nishide eds, Wiley-VCH, 2009.

[20] T. T. Albrecht, R. Steiner, J. D. Rouchey, C. M. Stafford, E. Huang, M. Bal, M. T. Tuominen, C. J. Hawker and T. P. Russell, *Adv. Mater.*, vol. 12, p. 787, 2000.

[21] T. T. Albrecht, J. D. Rouchey, T. P. Russell and R. Kolb, *Macromolecules 2002, 35, 8106.* , vol. 35, p. 8106, 2002.

[22] J. Hahm and S. J. Sibener, *J. Chem. Phys.* , vol. 114, p. 4730, 2001.

[23] C. Daniel, I. W. Hamley, W. Mingvanish and C. Booth, *Macromolecules*, vol. 33, p. 2163, 2000.

[24] I. W. Hamley, *Curr. Opin. Colloid Interface Sci.*, vol. 5, p. 342, 2000.

[25] A. Turturro, E. Gattiglia, P. Vacca and G. T. Viola, *Polymer* , vol. 21, p. 3987, 1995.

[26] G. Kim and M. Libera, *Macromolecules*, vol. 31, p. 2670, 1998.

[27] E. Huang, S. Pruzinsky, T. P. Russell, J. Mays and C. J. Hawker, *Macromolecules* , vol. 32, p. 5299, 1999.

[28] E. Huang, T. P. Russell, C. Harrison, P. M. Chaikin, R. A. Register, C. J. Hawker and J. Mays, *Macromolecules* , vol. 31, p. 7641, 1998.

[29] R. D. Peters, X. M. Yang, Q. Wang, J. J. D. Pablo and P. F. Nealey, *J. Vac. Sci. Tech. B* , vol. 18, p. 3530, 2000.

[30] S. O. Kim, H. H. Solak, M. P. Stoykovich, N. J. Ferrier, J. J. D. Pablo and P. F. Nealey, *Nature* , vol. 424, p. 411, 2003.

[31] A. Sepe, E. T. Hoppe, S. Jaksch, D. Magerl, Q. Zhong, J. Perlich, D. Posselt, D. M. Smilgies and C. M. Papadakis, *J. Phys.: Condens. Matter* , vol. 23, p. 254213, 2011.

[32] T. Hashimoto, J. Bodycomb, Y. Funaki and K. Kimishima, *Macromolecules* , vol. 32, pp. 952-954, 1999.

[33] J. Bodycomb, Y. Funaki, K. Kimishima and T. Hashimoto, *Macromolecules* , vol. 32, pp. 2075-2077, 1992.

[34] K. Mita, H. Tanaka, K. Saijo, T. Mikihito and T. Hashimoto, *Macromolecules* , vol. 40, p. 5923, 2007.

[35] B. C. Berry, A. W. Bosse, J. F. Douglas, R. L. Jones and A. Karim, *Nano Lett.*, vol. 7, no. 9, pp. 2789-2794, 2007.

[36] S. H. Kim, M. J. Misner, T. Xu, M. Kimura and T. P. Russell, *Adv. Mater.*, vol. 16, p. 226, 2004.

[37] M. Kimura, M. J. Mister, T. Xu, H. S. Kim and T. P. Russell, *Langmuir*, vol. 19, p. 9910, 2003.

[38] Z. Lin, D. H. Kim, X. Wu, L. Boosahda, D. Stone, L. L. Rose and T. P. Russell, *Adv. Mater.*, vol. 14, p. 1373, 2002.

[39] K. Temple, K. Kulbaba, K. N. Power-Billard, I. Manners, K. A. Leach, T. Xu, R. T. P. and C. J. Hawcker, *Adv. Mater.*, vol. 15, p. 297, 2003.

[40] M. Lazzari and C. D. Rosa, Block Copolymers in Nanoscience, Wiley-VCH, Verlag GmbH & Co. Weinheim, 2006.

[41] M. J. Fasolka and A. M. Mayes, *Annu. Rev. Mater. Res.*, vol. 31, p. 323, 2001.

[42] M. W. Matsen, *Curr. Opin. Colloid Interf. Sci.*, vol. 3, p. 40, 1998.

[43] C. S. Henkee, E. L. Thomas and L. J. Fetters, *J. Mater. Sci.*, vol. 23, p. 1685, 1988.

[44] G. Coulon, V. R. D. V., T. P. Russell and P. F. Green, *Macromolecules*, vol. 22, p. 2581, 1989.

[45] S. H. Anastasiadis, T. P. Russell, S. K. Satija, M. C. F. and ., *Phys. Rev. Lett.,* vol. 62, p. 1852, 1989.

[46] T. P. Russell, G. Coulon, V. R. Deline and M. D. C., *Macromolecules,* vol. 22, p. 4600, 1989.

[47] S. H. Anastasiadis, T. P. Russell, S. K. Satija and C. F. Majkrzak, *J. Chem. Phys.,* vol. 92, p. 5677, 1990.

[48] T. P. Russell, A. Menelle, S. H. Anastasiadis, S. K. Satija and C. F. Majkrzak, *Macromolecules,* vol. 24, p. 6269, 1991.

[49] B. Collin, D. Chatenay, G. Coulon, D. Ausserre and Y. Gallot, *Macromolecules,* vol. 25, p. 1621, 1992.

[50] G. Coulon, J. Dailant, B. Collin, J. J. Benattar and Y. Gallot, *Macromolecules,* vol. 26, p. 1582, 1993.

[51] A. M. Mayes, T. P. Russell, P. Bassereau, S. M. Baker and S. G. S., *Macromolecules,* vol. 27, p. 749, 1994.

[52] V. Carvalho and E. L. Thomas, *Phys. Rev. Lett.,* vol. 73, p. 3321, 1994.

[53] S. Joly, D. Ausserre, G. Brotons and Y. Gallot, *Eur. Phys. J. E* ., vol. 8, p. 355, 2002.

[54] P. Lambooy, R. T. P., G. J. Kellogg, A. M. Mayes, P. D. Gallagher and S. S. K., *Phys. Rev. Lett.,* vol. 72, p. 2899, 1994.

[55] N. Koneripalli, M. Singh, R. Levicky, F. S. Bates, P. D. Gallagher and S. S. K., *Macromolecules,* vol. 28, p. 2897, 1995.

[56] G. J. Kellogg, D. G. Walton, M. A. M., P. Lambooy, T. P. Russell, P. D. Gallagher and S. K. Satija, *Phys. Rev. Lett.,* vol. 76, p. 2503, 1996.

[57] N. Koneripalli, R. Levicky, F. S. Bates, J. Ankner, H. Kaiser and S. S. K., *Langmuir,* vol. 12, p. 6681, 1996.

[58] I. In, Y. H. La, S. M. Park, P. F. Nealey and P. Gopalan, *Langmuir* , vol. 22, p. 7855, 2006.

[59] S. Ji, C. C. Liu, J. G. Son, K. Gotrik, G. S. W. Craig, P. Gopalan, F. J. Himpsel, K. Char and P. F. Nealey, *Macromolecules,* vol. 41, p. 9098, 2008.

[60] S. H. Kim, M. J. Misner and T. P. Russell, *Adv. Mater.* , vol. 20, p. 4851, 2008.

[61] M. S. Turner, *Phys. Rev. Lett.* , vol. 69, p. 1788, 1992.

[62] K. R. Shull, *Macromolecules* , vol. 25, p. 2122, 1992.

[63] G. R. Pickett, T. A. Witten and S. R. Nagel, *Macromolecules* , vol. 26, p. 3194, 1993.

[64] M. Kikuchi and K. Binder, *J. Chem. Phys.* , vol. 101, p. 3367, 1994.

[65] G. Brown and A. Chakrabarti, *J. Chem. Phys.;,* vol. 102, p. 1440, 1995.

[66] G. T. Pickett and A. C. Balazs, *Macromolecules,* vol. 30, p. 3097, 1997.

[67] M. W. Matsen, *J. Chem. Phys.* , vol. 106, p. 7781, 1997.

[68] W. H. Tang and T. A. Witten, *Macromolecules* , vol. 31, p. 3130, 1998.

[69] T. Geisinger, M. Muller and K. Binder, *J. Chem. Phys.* , vol. 111, p. 5251, 1999.

[70] A. L. Frischknecht, J. G. Curro and L. J. D. Frink, *J. Chem. Phys.* , vol. 117, p. 10398, 2002.

[71] J. A. Gratt and R. E. Cohen, *J. Appl. Polym. Sci.* , vol. 88, p. 177−182. , 2003.

[72] J. A. Gratt and R. E. Cohen, *J. Appl. Polym. Sci.,* vol. 91, p. 3362−3368., 2004.

[73] C. Xu, K. Ohno, V. Ladmiral, D. E. Milkie, J. M. Kikkawa and R. J. Composto, *Macromolecules* , vol. 42, p. 1219−1228, 2009.

[74] R. D. Deshmukh, Y. Liu and R. J. Composto, *Nano Lett.* , vol. 7, p. 3662−3668, 2007.

[75] R. A. V. Ramanan Krishnamoorti, Polymer Nanocomposites: Synthesis, Characterization, and Modeling, American Chemical Society: Washington, D.C, 2002.

[76] H. D. Wagner and R. Vaia, *Materials Today,* vol. 7, pp. 38-42, 2004.

[77] K. Hatada, T. Kitayama and O. Vogl, Macromolecular Design of Polymeric Materials, New York: Marcel Dekker eds,, 1997.

[78] N. Hadjichristidis, M. Pitzikalis, S. Pispas and H. Iatrou, *Chem. Rev.*, vol. 101, p. 3747, 2001.

[79] M. A. Hillmyer, *Adv. Polym. Sci. ,* vol. 190, p. 137, 2005.

[80] T. Hashimoto, K. Tsutsumi and Y. Funaki, *Langmuir 1997, 13, 6869,* vol. 13, p. 6869, 1997.

[81] K. W. Guarini, C. T. Black and S. H. I. Yeung, *Adv. Mater. ,* vol. 14, p. 1290, 2002.

[82] S. B. Darling, N. A. Yufa, A. L. Cisse, S. D. Bader and S. J. Sibener, *Adv. Mater.,* vol. 17, pp. 2446-2450, 2005.

[83] M. Szwarc, M. Levy and R. Milkovich, *J .Am. Chem. Soc. ,* vol. 78, p. 2656, 1956.

[84] S. Kim, B. Fisher, H. J. Eisler and M. Bawendi, *J. Amer. Chem. Soc.,* vol. 125, no. 38, pp. 11466-11467, 2003.

[85] L. Qu and X. Peng, *J. Amer. Chem. Soc.,* vol. 124, no. 9, pp. 2049-2055, 2002.

[86] R. E. Bailey, A. M. Smith and S. Nie, *Physica ,* vol. E 25, pp. 1-12, 2004.

[87] S. C. Minne, S. R. Manalis and C. F. Quate, *Appl. Phys. Lett.,* vol. 67, p. 3918, 1995.

[88] H. Hoppe, M. Niggemann, C. Winder, J. Kraut, R. Hiesgen, A. Hinsch, D. Meissner and N. S. Sariciftci, *Adv. Funct. Mater.,* vol. 14, p. 1005, 2004.

[89] D. J. Wold and C. D. Frisbie, *J. Am. Chem. Soc.* , vol. 123, p. 5549, 2001.

[90] S. Guo and B. B. Akhremitchev, *Langmuir,* vol. 24, p. 880, 2008.

[91] L. Fu, X. Liu, Y. Zhang, V. P. Dravid and C. A. Mirkin, *Nano Lett.* , vol. 3, p. 757, 2003.

[92] J. M. Kinsella and A. Ivanisevic, *Langmuir,* vol. 23, p. 3886, 2007.

[93] Y. Li, B. W. Maynor and J. Liu, *J. Am. Chem. Soc.* , vol. 123, p. 2105, 2001.

[94] A. Alessandrini and P. Facci, *Meas Sci Technol,* vol. 16, p. R65, 2005.

[95] G. Zavala, *Colloid. Polym. Sci.* , vol. 286, p. 85, 2008.

[96] Y. Shan and H. Wang, *Chem. Soc. Rev.*, vol. 44, pp. 3617-3638, 2015.

CHAPTER 6

Hybrid Nanomaterials: Experimental Section

6.1 Introduction

Over the last years, hybrid photovoltaics (PV) have attracted significant interest thanks to the possibility to form efficient heterojunction combining inorganic semiconductors and organic compounds taking, in this way, advantages of both materials.

In particular, the typical features of an inorganic semiconductor are the high carrier mobility and the more environmentally stability and tunability of absorption spectra. On the other hand, the presence of the organic component in hybrid solar cells leads to other important advantages in terms of cost efficiency, scalable wet processing, the variety of organic materials, light weight, and flexibility.

Therefore, a good combination of different components, having the aforementioned properties, and well-designed hybrid structures are aspects of prime importance for the realization of highly efficient solar cells.

In this regard, the energy-level alignment at the interfaces between two materials plays a critical role for optimal hybrid systems.

The commonly used structures are the p-n junction [1, 2] and type-II heterojunction [3]. Type-II heterojunction presents a reduced band gap in spatial which allows to obtain a more efficient absorption of the sunlight, although the donor and acceptor materials have wide bandgaps. [3, 4, 5] The typical photovoltaic applications for these structures are dye-sensitized

solar cells (DSSC), [6, 7] quantum dot-sensitized solar cell (QDSSC), [8, 9] core/shell nanowire solar cells, [10, 11] and so on.

Basically, heterostructures consist of bringing two different semiconductors into physical contact and their behavior strictly depends on the alignment of the energy bands of materials at the interface. Band alignment can be classified as type-I (straddling gap), type-II (staggered gap) and type-III (broken gap). [5] The former two types are more frequently used in PV field (Fig. 6.1). Concerning the type-I heterostructure, the semiconductor 1 (sem1) have a narrower band gap than the band gap of semiconductor 2 (sem2). In particular, the conduction and valence band edges of sem1 are located between the energy bands of sem2 (Fig. 6.1a). This band structure causes electrons and holes to simultaneously accumulate in the sem1 and, thus, the carrier recombination is enhanced. The more common applications are lasers, light emitting diodes, etc.

The type-II heterostructure is based on a staggered band offset formed at interface, and the lowest energy positions for electrons and holes are located in different materials, respectively (Fig. 6.1b). This means that type-II heterostructures can easily promote the charge separation and is potential for photovoltaic applications. [5, 12]

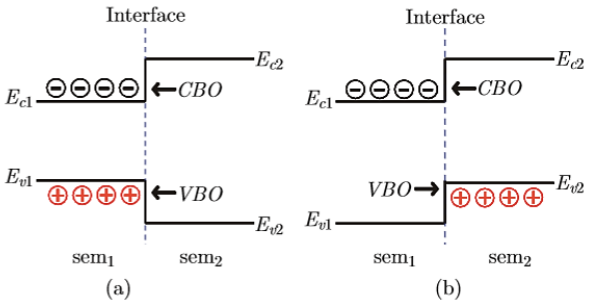

Fig. 6.1. Energy band diagrams for type-I (a) and -II heterostructures (b). [5]

This kind of structures is mainly based on II-VI and III-V binary semiconductors, such as ZnO/ZnS, [13] ZnO/ZnSe, [14] ZnO/ZnTe, [4] CdSe/CdTe, [15] and GaN/GaP, [3]. Among them, ZnO-based heterostructures attracted more attentions due to its abundant resources and facilitating growth. [5, 16]

This study aims to realize highly efficient solar cells exploiting self-assembly of block copolymers (BCPs) to make active layer based on well-ordered polymeric morphology hosting *n*- and *p*-type semiconductor nanoparticles in different domains. Herein, type II-heterojunction is formed by ZnO/CdSe nanoparticles which potentially will accelerate the separation of photo excited electron–hole pairs and improve the efficiency of solar cells.

6.2 Nanocomposites based on lamellar PS-b-PMMA and ZnO nanoparticles

This section describes the preparation of hybrid nanocomposites through the confinement of the *n*-type semiconductor nanoparticles in the vertical BCP nanodomains.

In a recent paper [17] we demonstrated a simple method to fabricate ordered arrays of ZnO nanoparticles covered with *n*-hexadecylamine (HDA) by using poly(styrene)-b-poly(methyl methacrylate) copolymer (PS-b-PMMA) as template for controlling the distribution of them and to form, thus, a continuous path of charge carriers with promising electrical properties. In particular, the presence of surface functionalization favors the chemical affinity of the nanoparticles with the PS domains of PS-b-PMMA.

The PS-b-PMMA block copolymer with a volume fraction of the PS blocks equal to 0.52 was selected in order to obtain a lamellar phase-separated morphology. Thin films of pure BCP and of the BCP-based nanocomposites were prepared by spin coating toluene solutions containing 1 wt % PS-b-PMMA and 0.1 wt % ZnO NPs on ITO supports. The TEM image of a thin film (~70 nm thick) of the neat BCP annealed at 150 °C for 6 h in vacuo and stained with RuO_4 is shown in Fig. 6.2.

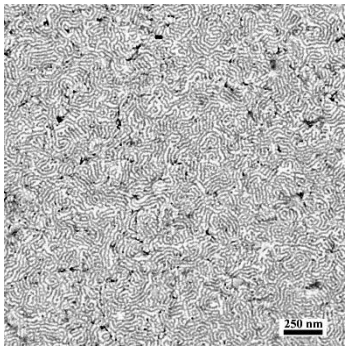

Fig. 6.2. Bright-field TEM images of thin films (~70 nm thick) annealed at 150 °C in vacuo for 6 h of the neat PS-b-PMMA (BCP0) stained with RuO_4.

The dark regions correspond to the stained PS lamellar microdomains, whereas the lighter regions to the PMMA domains. Note that there is a disordered lamellar morphology with lamellar domains oriented perpendicular to the substrate.

The vertical orientation of lamellae is in agreement with previous results [18, 19] demonstrating that the use of ITO support combined with thermal annealing treatments facilitates the vertically oriented morphology of the lamellar BCP domains. The average lamellar thicknesses are ~14 ± 2 and ~18 ± 2 nm for PS and PMMA, respectively.

TEM images of the nanocomposite thin films based on BCP and ZnO stained with RuO_4 and without staining are reported in Fig. 6.3 (A, B), respectively.

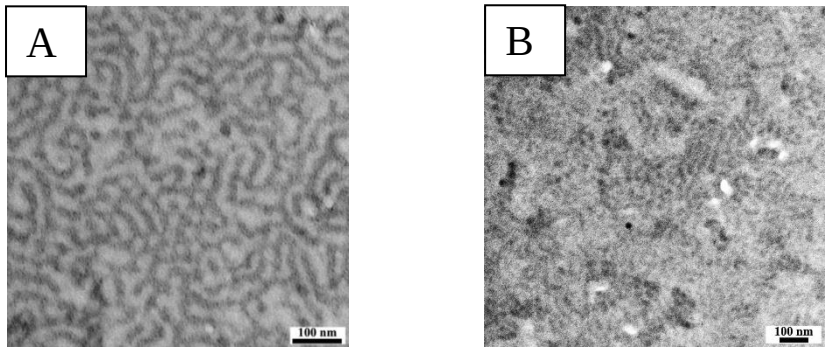

Fig. 6.3. Bright-field TEM images of thin films (~70 nm thick) annealed at 150 °C in vacuo for 6 h of the PS-b-PMMA/ZnO nanocomposite BCP-ZnO on ITO substrates: A) stained with RuO_4 and B) without staining

These images also show a disordered lamellar morphology with the vertical orientation of the lamellar domains, and a slight increase of the average lamellar thickness is observed (~16 ± 3 nm for PS and ~20 ± 3 nm for PMMA). In particular, the Fig. 6.3 A of the nanocomposite film stained with RuO_4 shows dark stained PS lamellar domains alternating with bright not-stained PMMA lamellae. In the case of the image of Fig. 6.3 B obtained without performing any staining procedure, the dark regions correspond to the microdomains containing ZnO NPs. The achieved high contrast between the two different BCP lamellar nanodomains confirms that the ZnO NPs are selectively included only in the PS blocks of the BCP, due to the chemical affinity of the surface-coated ZnO NPs.

In this process it was seen that the thermal annealing at a temperature above the BCP glass transition temperature (150 °C) plays a key role in order to favor the migration of the ZnO NPs in the PS lamellar domains and simultaneously leads to the formation of the desired vertical morphology of the lamellar BCP domains.

Therefore, the electric properties of the discussed hybrid nanocomposites were tested by current−voltage (I-V) measurements confirming the

presence of continuous path of charge carriers in the BCP films, when the ZnO NPs content is above a threshold concentration c* (see Appendix).

6.3 Preparation of the nanoporous PS-b-PMMA thin films

Regarding the realization of type-II heterostructures between *p*- and *n*-type semiconductor nanoparticles, in the second step, attempts to fabricate nanocomposites based on PS-b-PMMA and *p*-type CdSe nanoparticles were performed. The adopted approach is based on the following steps:

1. Selective removal of the sacrificial polymer block (i.e. PMMA);

2. Backfilling of the porous structure with inorganic material (i.e. dipping of porous template into NPs suspension and its successive withdrawal normal to the solution surface as shown in Fig. 6.4 [20]).

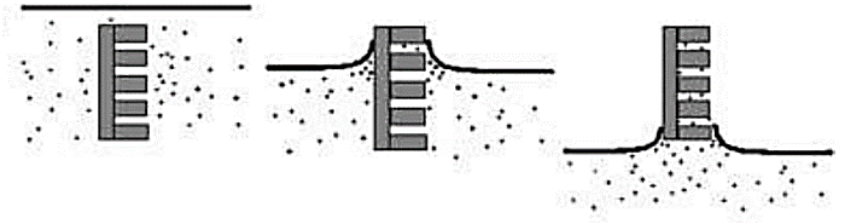

Fig. 6.4. Schematic representation of process for depositing nanoparticles into nanoporous template by withdrawal of the template from a solution. [20]

In particular, this section focuses on the selective degradation of PMMA blocks from a self-assembled block copolymer structure employing UV irradiation. It is known that the exposure of PS-b-PMMA block copolymer to UV light decomposes PMMA phase into oligomers, that can then be removed from the matrix through dissolution in acetic acid, and simultaneously crosslinks the PS blocks. [21]

Thin films of PS-b-PMMA were prepared by spin coating dilute toluene solutions containing 1 wt% PS-b-PMMA on ITO substrates. Different tests were carried out by varying both the UV exposure and acetic acid washing times in order to optimize the full removal process of PMMA blocks. All samples were analyzed by scanning electron microscopy (SEM). The SEM images are reported in Fig. 6.5.

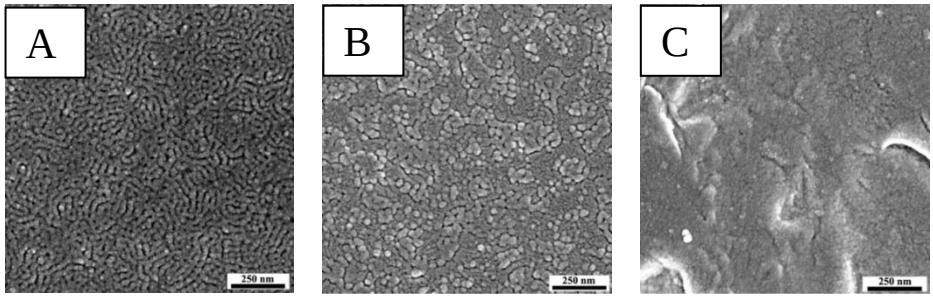

Fig. 6.5. SEM images of a thin film of PS-*b*-PMMA subjected to selective removal of PMMA blocks by exposure to UV radiations and acetic acid washing. A) 1 h (UV) and 30 minutes (acetic acid); B) 3 h (UV) and 1 h (acetic acid); C) 6 h (UV) and 1h (acetic acid).

SEM analysis shows that the exposure to UV radiation for 1 h followed by an acetic acid washing for 30 minutes (Fig. 6.5 A) is enough to obtain the desired nanoporous template and does not alter the initial lamellar morphology. This thin film was also characterized by TEM analysis (Fig. 6.6)

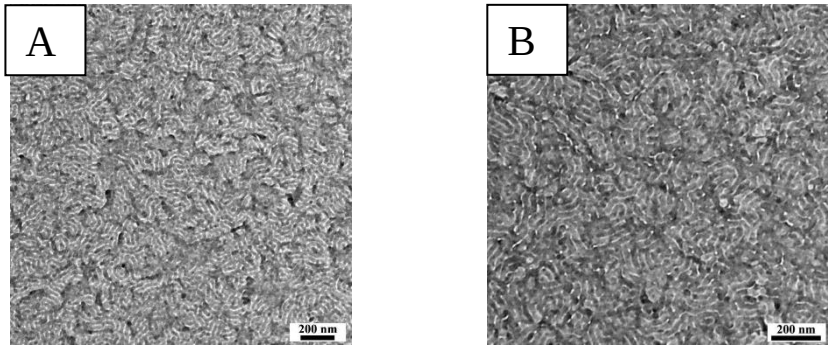

Fig. 6.6. TEM bright-field images of a thin film of PS-*b*-PMMA submitted to selective removal of PMMA block by exposure to UV radiations (1h) and acetic

acid washing (30 minutes). A) staining process with RuO_4; B) without staining process with RuO_4. PS domains are dark both in A and B.

TEM micrograph (Fig. 6.6 B) of the etched film without any chemical staining highlights a pronounced contrast between the two different BCP nanodomains as in the case of the stained film (Fig. 6.6 A). It demonstrates that the PMMA blocks were effectively removed and nanochannels were created allowing, thus, the free transmission of the electron beam. The average size of PS domains (20 ± 3 nm) is greater than that those left free by PMMA upon removal (7.4 ± 2 nm) probably due to a swelling effect with acetic acid or to a not completed removal of PMMA blocks.

Nevertheless, the resultant morphology from PMMA removal was not reproducible. In fact, in repeated trials disordered morphologies were also obtained where the lamellae were randomly oriented both parallel and perpendicular to the ITO surface. This scarce reproducibility is due to unbalanced interactions of the polymer blocks at the interface with air and ITO support as discussed in paragraph 5.4.3.

One of the commonly used strategy for the surface neutralization, preventing, thus, the preferential wettability of the substrate with respect to the PS and/or PMMA blocks, is the "grafting to" approach, consisting in the chemical linking of a functional random copolymer to the substrate. [22]

In collaboration with research group of Prof. M. Laus, University of Piemonte Orientale, the ITO supports were conveniently neutralized through a grafting reaction with a OH-terminated random poly(styrene)-r-poly(methylmethacrylate) (PS-r-PMMA) copolymer (RCP). In particular, the crosslinking reaction is activated by thermal treatment performed in a Rapid Thermal Processing (RTP) machine with three consecutive phases: the heating ramp (18 °C s^{-1}), the plateau and the relaxation ramp. [23]

Two different PS-r-PMMA random copolymers, called as FSM13 and FSM6, were used in the present activity, whose characteristics are reported in Tab. 6.1.

Tab. 6.1. Number average molecular weight (M_n), polydispersity index of the molecular masses (PDI = M_w/M_n), styrene fraction (f_S) and RTP Process characteristics.

Sample	**ITO (nm)**	**M_n (g/mol)**	**PDI**	**f_S (%)**	**RTP Process**	
					Time (s)	**T(°C)**
FSM13	160	5700	1.19	59.7	300	250
FSM6	160	8100	1.24	57.7	300	250

ITO supports coated with the random copolymers FSM13 and FSM6 were then used instead of bare ITO substrate to deposit the BCP and to study the effect of the annealing treatments on the morphological BCP evolution.

Thin films of PS-*b*-PMMA were prepared as previously discussed in paragraph 6.2 on ITO/FSM13 and ITO /FSM6 substrates. To improve the lamellar morphology of the BCP, these films were subjected to thermal annealing in vacuo at 150 °C for 6, 24 and 32 h. The corresponding TEM images are shown in Fig. 6.7 where the contrast is provided by staining with RuO_4.

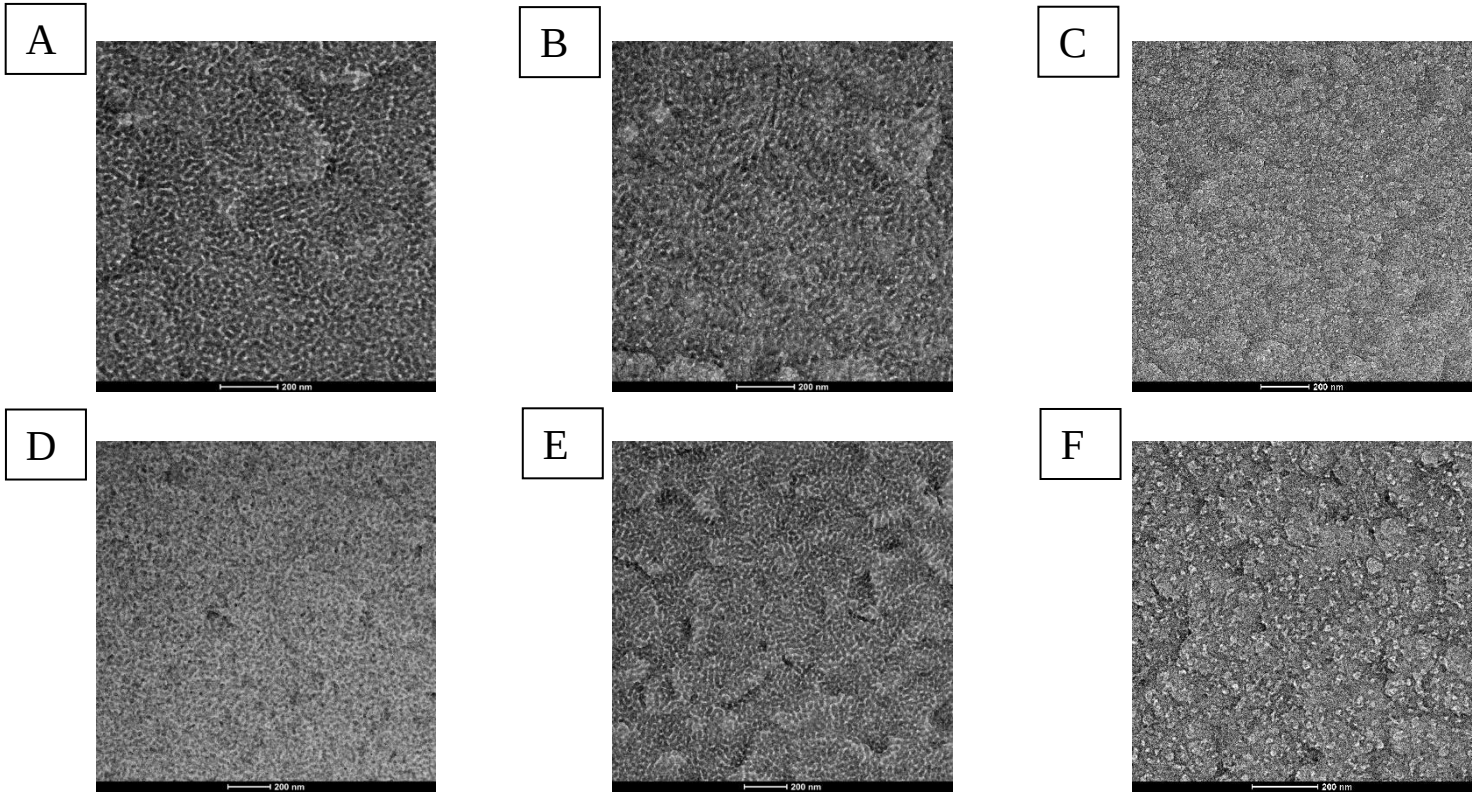

Fig. 6.7. Bright-field TEM images of PS-*b*-PMMA thin films obtained by spin coating BCP solutions on ITO/FSM13 substrates and subjected to thermal annealing in vacuo at 150 °C for 6 (A), 24 (B) and 32 h (C); BCP thin films obtained by spin coating BCP solutions on ITO/FSM6 substrates and subjected to thermal annealing in vacuo at 150 °C for 6 (D), 24 (E) and 32 h (F). The TEM grids were stained with RuO_4 before observation.

The TEM images exhibit the phase separation with a disordered morphology in which microdomains are mainly perpendicularly oriented to the substrate surface. The dark regions correspond to the stained PS lamellar microdomains while the lighter regions are the PMMA domains.
Significant results were obtained for a thermal annealing time of 24 h (Fig. 6.7 B, E). In fact, the PS-b-PMMA films deposited both on ITO/FSM13 and ITO/FSM6 are characterized by a good contrast between the blocks where the average lamellar spacing is estimated to be ~ 18 ± 2 nm for PS and 9.5 ± 2 nm for PMMA. Note that these values are not in agreement with the block sizes measured for PS-b-PMMA thin film shown in Fig. 6.2. It is worth noting that the situation deteriorates when the samples were annealed for 32 h (Fig. 6.7 C, F).
In order to improve the spatial and orientational control of BCP nanodomains, further tests were carried out increasing the annealing temperature to 190 °C for 24 h and 32 h.

In Fig. 6.8 representative bright-field TEM images of PS-b-PMMA thin films deposited both on ITO/FSM13 (Fig. 6.8 A, B) and ITO/FSM6 (Fig. 6.8 C, D) supports and subjected to thermal annealing in vacuo at 190 °C for 24 and 32 h are reported. The films were stained with RuO_4 to achieve a good contrast between PS and PMMA domains.

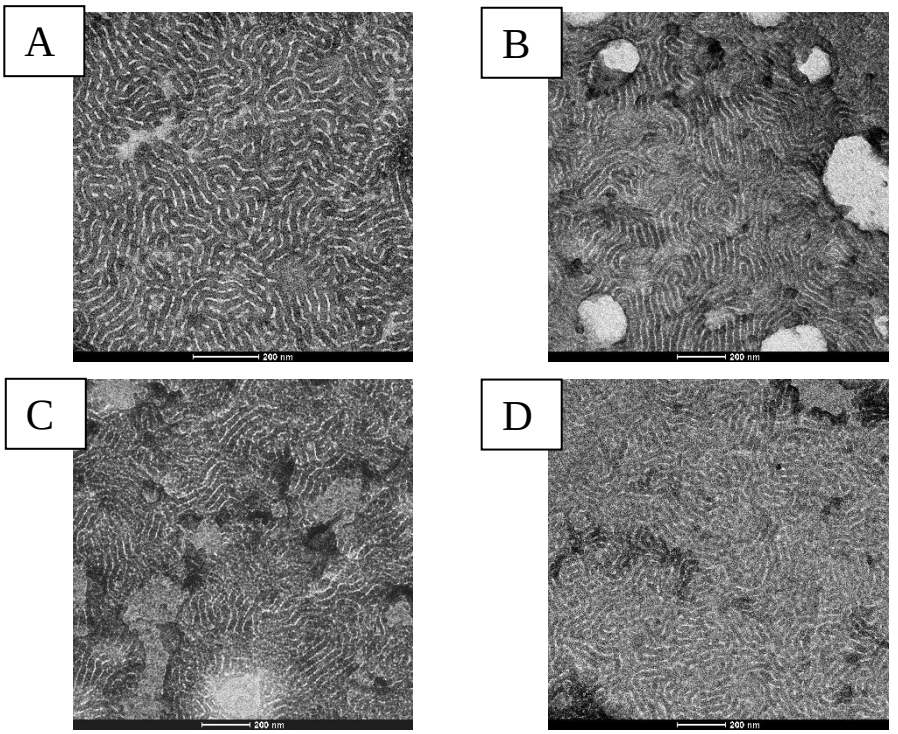

Fig. 6.8. Bright-field TEM images of PS-*b*-PMMA thin films obtained by spin coating BCP solutions on ITO/FSM13 substrates and subjected to thermal annealing in vacuo at 190 °C for 24 (A) and 32 h (B); BCP thin films obtained by spin coating BCP solutions on ITO/FSM6 substrates and subjected to thermal annealing in vacuo at 190 °C for 24 (C)and 32 h (D). The TEM grids were stained with RuO_4 before observation.

The images clearly show that annealing treatment at higher temperature (T=190 °C) allowed obtaining the desired morphology with the vertical orientation of the lamellar BCP nanodomains (Fig. 6.8 A-D).

The morphology of Fig. 6.8 (A, B) relative to BCP deposited on ITO/FSM13 is particularly interesting because highlights well-defined phase separation where parallel lamellar domains of ≈200nm cover the whole area of the thin film according to a well-connected pattern. The average lamellar spacing is substantially the same in both cases and is ~ 22 ± 2 nm and ~ 5 ± 1 nm for PS and PMMA, respectively.

Thin films subjected to thermal annealing both at 150 (Fig. 6.7 A, E) and 190 °C (Fig. 6.8 A, C) for 24 or 32 h on ITO substrate coated with FSM13 and FSM6 random copolymers, were further treated with UV radiation and subsequent washing with acetic acid to obtain nanoporous surfaces. The TEM images of the so prepared samples after staining with RuO_4 are shown in Fig. 6.9.

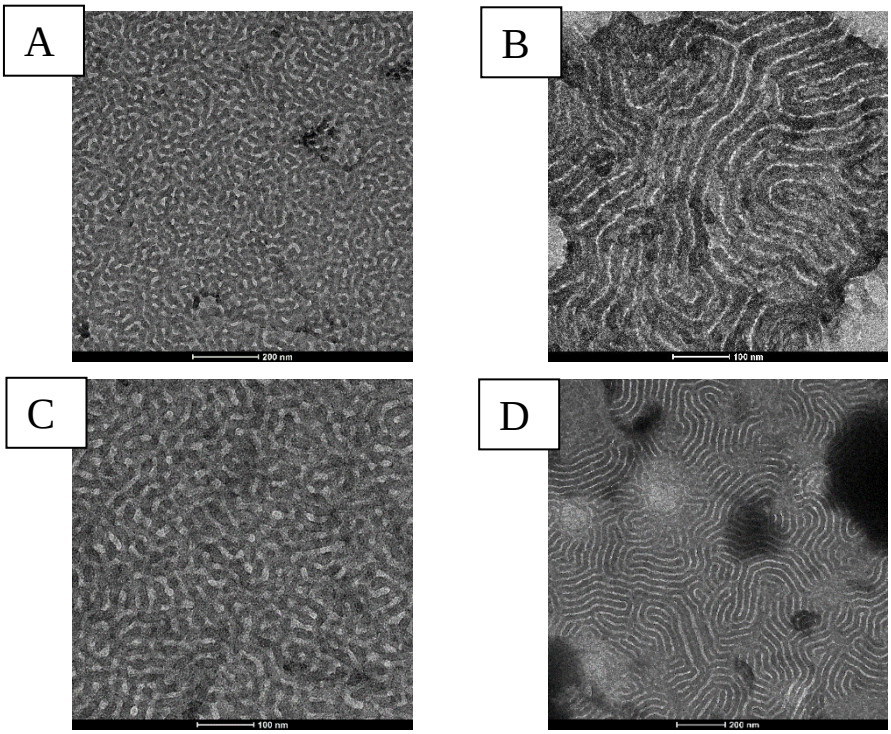

Fig. 6.9. Bright-field TEM images of PS-b-PMMA thin films obtained by spin coating BCP solutions on ITO/FSM13 substrates and subjected to thermal annealing in vacuo at 150 °C for 24 h (A) and 190 °C for 32 h (B); BCP thin films obtained by spin coating BCP solutions on ITO/FSM6 substrates and subjected to thermal annealing in vacuo at 150 °C (C) and 190 °C (D) for 24 h. The TEM grids were subjected to UV irradiation for 1h and subsequent acetic acid washing for 30 minutes. Finally, they were stained with RuO_4 before observation.

The phase separated morphology was observed for all samples. In fact, the TEM images (Fig. 6.9) of the etched thin films show a more remarkable contrast between the polymeric blocks than the films before the removal of

PMMA (Fig. 6.7 B, E and Fig. 6.8 B, C), demonstrating the effective removal process and consequent formation of nanopores.

No significant differences in morphology are observed in thin films prepared on neutralized ITO supports using both FSM13 and FSM6 random copolymers and subjected to thermal annealing at 150 °C as shown in Fig. 6.9 (A, C).

A well-defined phase separation with a disordered lamellar morphology and long-range order was observed for the nanoporous BCP thin film obtained by spin coating BCP solutions on ITO/FSM6 annealed at 190 °C for 24 h where the average spacing of PS lamellae is estimated to be ~ 20 ± 1 nm while the size of the pores left upon PMMA removal is ~ 8 ± 1 nm (Fig. 6.9 D).

Clearly, both the neutralization procedure of ITO substrates and the optimization of thermal annealing conditions for PS-b-PMMA thin film allowed obtaining well reproducible lamellar morphologies with the perpendicular orientation of lamellae with respect to the substrate surface.

6.4 PS-b-P4VP block copolymer

In a second research line aimed at fabrication of active layers for solar cells using BCP as templates for selective inclusion of *n*- and *p*- type semiconductor NPs in separated domains, the morphology of poly(styrene)-b-poly(4-vinylpyridine), (PS-b-P4VP) was investigated.

6.4.1 Thermal and structural analyses

The X-ray powder diffraction profile, registered at room temperature, and the DSC cooling and heating curves, recorded at 10 °C/min of the sample PS-b-P4VP, are reported in Fig. 6.10 (A, B), respectively. The BCP sample

is amorphous with glass transition temperatures of the PS and P4VP blocks of 104 °C and 154 °C, respectively.

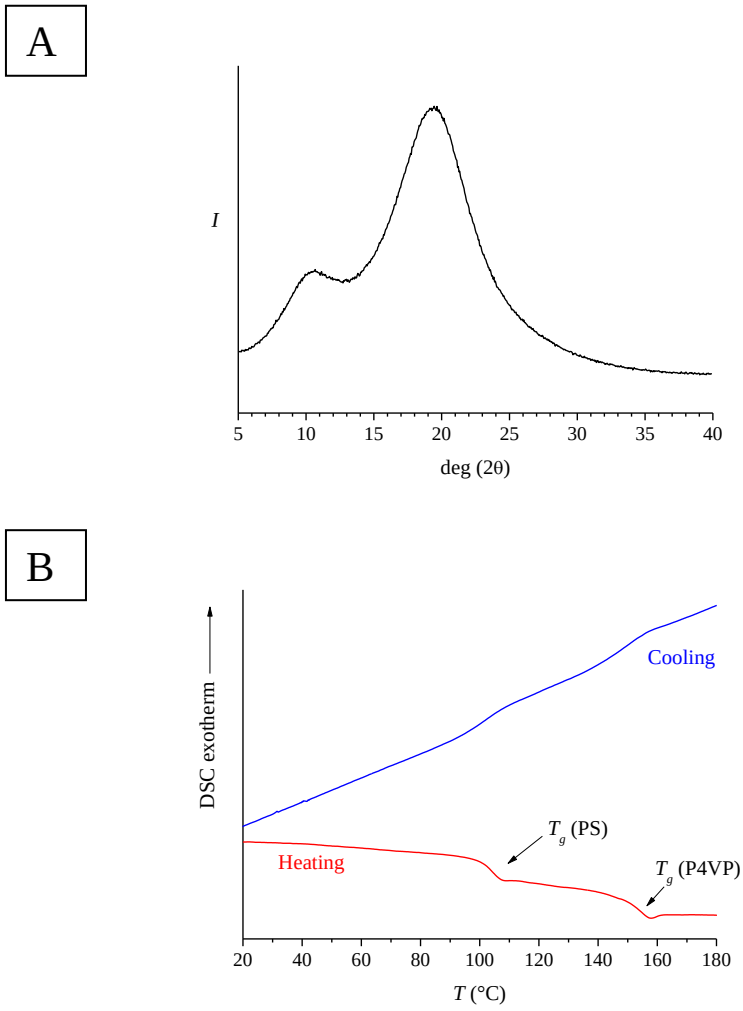

Fig. 6.10. A) X-ray powder diffraction profile; B) DSC heating and cooling curves of the sample PS-b-P4VP.

6.4.2 Morphological analysis of the neat PS-b-P4VP

PS-b-P4VP is nonionic amphiphilic diblock copolymer. [24] Its self-assembly behavior was widely investigated since the process toward formation of a lamellar morphology can be complicated by the strong tendency of the BCP to form micellar aggregates in the solutions, which could survive upon deposition onto the surface and in thin film formation. [25]

Solvent vapor annealing (SVA) strategy is usually adopted to obtain well-defined BCP film nanostructures improving both the kinetics of phase separation and the order of the structure. Indeed, annealing in selective solvents can lead to desired non-equilibrium structures with the proper microdomain orientation and long-range order. For this reason, the choice of the solvent for SVA is a critical step. Different parameters have to be evaluated, i.e., selectivity of the solvent to one of the blocks, vapor pressure and boiling point of the solvent. [26]

The Hildebrand solubility parameter (δ) can be used to indicate the similarity of the solvent to a polymer and, hence, solubility. [27] Materials with similar values of δ are likely to be miscible. This parameter δ is defined as the square root of the cohesive energy density (Eq. 6.1):

$$\delta = \sqrt{\frac{\Delta H_v - RT}{V_m}} \qquad Eq.\,6.1$$

where ΔH_v is the heat of vaporization, V_m the molar volume and RT is the ideal gas pV term.

The Hansen solubility parameters are an extension of the Hildebrand parameter to estimate individual contributions such as dispersive δ_d (van der Waals), polar δ_p and hydrogen bonding δ_H according to Eq. 6.2: [28]

$$\delta^2 = \delta_d^2 + \delta_p^2 + \delta_H^2 \qquad Eq.6.2$$

The Hansen solubility parameters and related contributions of PS, P4VP, PS-*b*-P4VP and possible useful solvents to obtain lamellar morphology are reported in Tab. 6.2.

Tab. 6.2. Hansen solubility parameters ($MPa^{0.5}$). [27, 28]

Material	**Dispersion Forces (δ_d)**	**Polarity (δ_p)**	**Hydrogen Bonds (δ_H)**	**Hansen solubility parameter (δ)**
PS	18.5	1.0	4.1	19.0
P4VP	18.1	7.2	6.8	20.6
Dimethylformamide *(*DMF*)*	17.4	13.7	11.3	24.9
1,4-dioxane	19.0	1.8	7.4	20.5
Chloroform ($CHCl_3$)	17.8	3.1	5.7	18.9
Toluene	18.1	1.4	2.0	18.3
Tetrahydrofuran *(*THF*)*	16.8	5.7	8.0	19.5
Ethanol	15.8	8.8	19.4	26.5

According to these values, suitable couples of solvents for the BCP in the dissolution step and successive SVA were selected. In particular, the solvent for the BCP dissolution has to be substantially neutral for both BCP blocks, whereas the solvent used for SVA was selected with a Hansen parameter close to that of a specific BCP block (PS or P4VP).

In a first trial, dimethylformamide (DMF) was used to dissolve BCP while *1,4*-dioxane to perform SVA. [29] In particular, the DMF is slightly selective solvent for P4VP blocks while *1,4*-dioxane for PS blocks.

In SVA process, another key aspect is the choice of substrate with particular attention to the nature of interactions that could be established at the interface of the BCP with both the substrate and the external

atmosphere. In fact, both interfaces can influence the wettability and impact the coating process and, consequently, the film thickness, uniformity and the morphology (i.e. preferential orientations of polymeric blocks) of BCP thin films.

In this work, thin films of PS-b-P4VP were prepared by spin-coating dilute solutions (1 wt%) of the BCPs in DMF on a silicon substrate (Si (100)) for preliminary tests and, subsequently, on the ITO substrates.

The morphological analysis was carried out by means of atomic force microscopy (AFM). The AFM images of PS-b-P4VP thin films obtained by spin coating BCP solutions on silicon substrates, before and after 48 and 65 h of SVA in *1,4*-dioxane atmosphere are reported in Fig. 6.11.

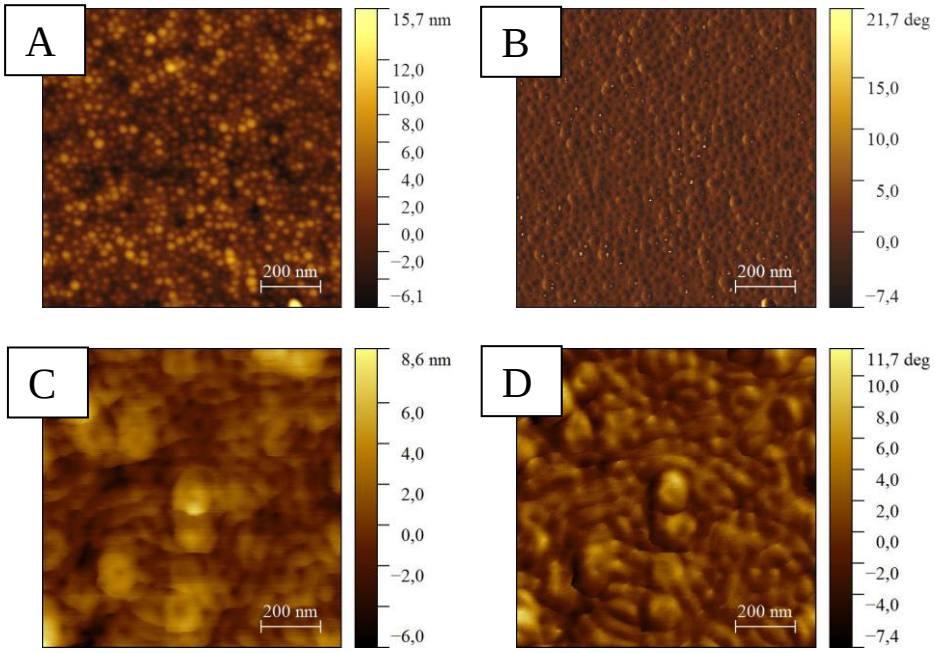

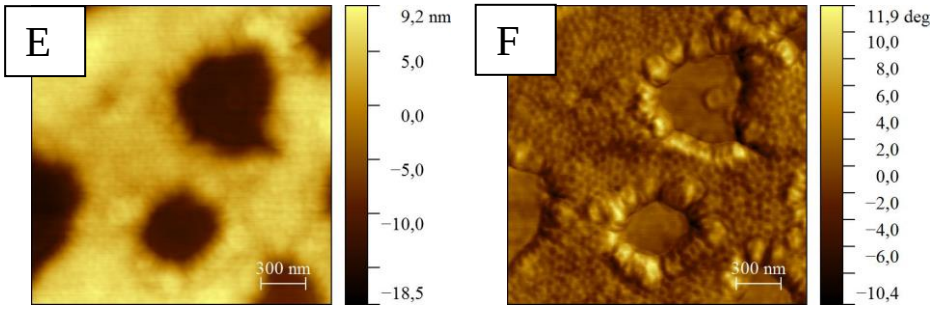

Fig. 6.11. AFM images of PS-b-P4VP thin film deposited on silicon substrate before (height A, phase B) and after being subjected to *1,4*-dioxane solvent vapor annealing for 48 (height C, phase D) and for 65 h (height E, phase F).

Note that a strong micellization phenomenon occurred when the thin film was formed with the appearance of the spherical micelle randomly distributed on the whole surface (Fig 6.11 A, B), the average size (*d*) being ~26± 3 nm.

The exposure to saturated *1,4*-dioxane vapors in a closed vessel at room temperature for 48 h led to a transition of micellar aggregates from spherical to worm-like where the average size is roughly ~ 45± 2 nm (Fig. 6.11 C, D). A further extension of annealing periods to 65 h (Fig. 6.11 C and 6.11 D) determined a partial de-wetting where it is still possible to observe the presence of spherical micelle (d~37± 2 nm) in the coated areas (Fig. 6.11 E, F).

The self-assembly behavior in thin films of PS-b-P4VP obtained by spin coating BCP solutions on ITO supports was also investigated using the same SVA protocol.

The AFM images of PS-b-P4VP thin films before and after 135 and 215h of SVA process still using *1,4*-dioxane vapor atmosphere are reported in Fig. 6.12.

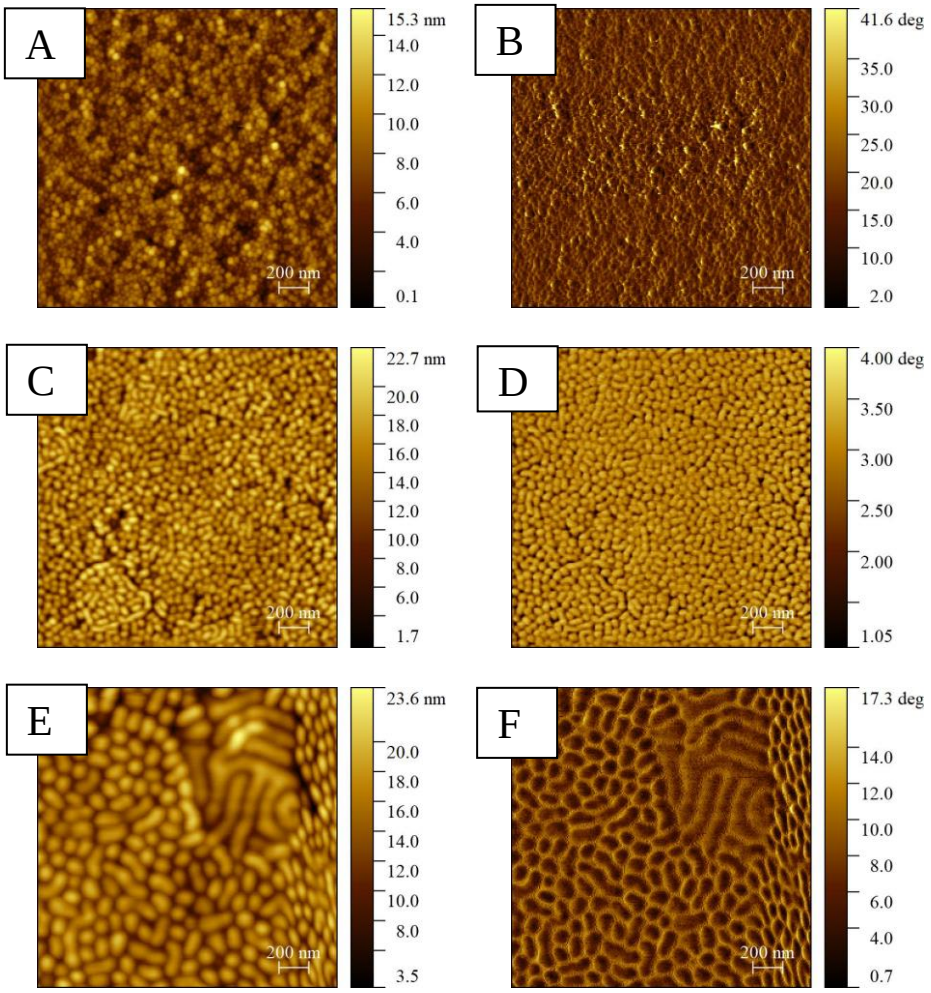

Fig. 6.12. AFM images of PS-b-P4VP thin film deposited on ITO substrate before (height A, phase B) and after being subjected to *1,4*-dioxane solvent vapor annealing for 135 (height C, phase D) and for 215h (height E, phase F).

As in the previous case, Fig. 6.12 (A, B) confirms the formation of micelle in the untreated BCP thin film using ITO as substrate. The average size of micelle is ~34 ± 1 nm.

Fig. 6.12 (C, D) illustrates the effect of the SVA process after 135 h on the BCP film where a transition from a disordered micellar arrangement to a more regular structure occurred leading to formation of regions of worm-

like entities (d~32 ± 2 nm) alternating with regions covered by spherical micelle (d~38 ± 3 nm).

By extending the annealing periods to 215 h, the mixed morphology changes only in small regions as shown in the encircled of Fig. 6.12 (E, F), where a wormlike morphology becomes apparent.

Since the self-assembly of lamellar forming systems for this BCP is really challenging to overcome the problem of micellization, a further trial test was carried out. It consisted of the preparation of PS-b-P4VP thin film obtained at room temperature by spin coating, after deposition of a slight excess of toluene-tetrahydrofuran (THF) mixtures (8:2 vol:vol) BCP solutions (0.5 wt%) onto ITO substrate. In particular, this solvent mixture was chosen to balance the strong selectivity of toluene for PS with a good solvent for the P4VP block. The polarity and hydrogen bonding contributions to the Hansen solubility parameter of THF, indeed, (Tab. 6.2) are in close match with those of P4VP. [30]

The SVA process was carried out by exposing the BCP thin film to THF vapor in a closed vessel at 50 °C. The higher neutrality of this solvent with respect to that of toluene solvent can be useful for decreasing the interactions between the PS and P4VP and enhance a separation of the blocks while increasing the chain mobility and facilitating defect annihilation. [26]

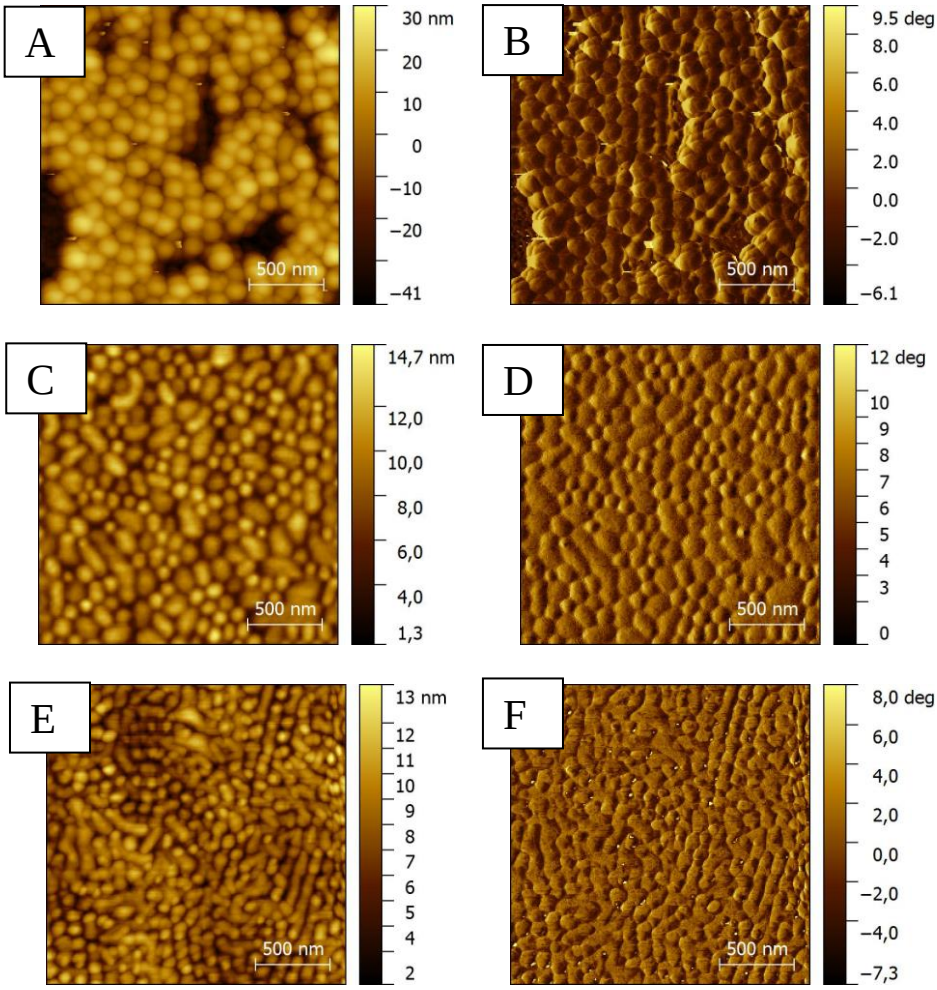

Fig. 6.13. AFM images of PS-b-P4VP thin film, obtained by spin coating solutions 0.5 wt% BCP in toluene/THF (8:2 vol:vol) solution on ITO substrate, before (height A, phase B) and after being subjected to THF solvent annealing for 3 h (height C, phase D) and for 6 h (height E, phase F) at 50 °C.

The thin film shows a strong micellization of PS-b-P4VP with the formation of very big spherical micelle whose size is about ~105 ± 4 nm as reported in Fig. 6.13 (A, B).

To rearrange these films into microphase separated structures, the solvent annealing in THF was carried out for 3 and 6 h at 50 °C (Fig. 6.13 C-F). The THF SVA allowed to modify the morphology only in part, as elongated micellar aggregates (d~53 ± 3 nm) were formed only in small regions,

whereas the majority of the surface remained covered by spherical micellar entities.

Bibliography of Chapter 6

[1] B. M. Kayes, H. A. Atwater and N. S. Lewis, *J. Appl. Phys.* , vol. 97, p. 114302, 2005.

[2] Y. F. Zhang, Y. F.Wang, N. Chen, Y. Y. Wang, Y. Z. Zhang, Z. H. Zhouand and L. M. Wei, *Nano Micro Lett.*, vol. 2, pp. 22-25, 2010.

[3] Y. Zhang, L. Wang and A. Mascarenhas, *Nano Lett.* , vol. 7, p. 1264, 2007.

[4] J. Schrier, D. O. Demchenko and L. W. Wang, *Nano Lett.* , vol. 7, p. 2377, 2007.

[5] Y. Cao, Z. Wu, J. Ni, W. A. Bhutto, J. Li, S. Li, K. Huang and J. Kang, *Nano-Micro Lett.* , vol. 4, no. 3, pp. 135-141, 2012.

[6] E. J. W. Crossland, M. Nedelcu, C. Ducati, S. Ludwigs, M. A. Hillmyer, U. Steiner and H. J. Snaith, *Nano Lett.* , vol. 9, p. 2813, 2009.

[7] E. L. Tae, S. H. Lee, J. K. Lee, S. S. Yoo, E. J. Kang and .. K. B. Yoon, *J. Phys. Chem. B* , vol. 109, p. 22513, 2005.

[8] K. S. Leschkies, R. Divakar, J. Basu, E. Enache-Pommer, J. E. Boercker, C. B. Carter, U. R. Kortshagen, D. J. Norris and E. S. Aydil, *Nano Lett.* , vol. 7, p. 1793, 2007.

[9] H. J. Lee, M. K. Wang, P. Chen, D. R. Gamelin, S. M. Zakeeruddin, M. Grätzel and M. K. Nazeeruddin, *Nano Lett.*, vol. 9, p. 4221–4227, 2009.

[10] S. A. Ivanov, A. Piryatinski, J. Nanda, S. Tretiak, K. R. Zavadil, W. O. Wallace, D. Werder and V. I. Klimov, *J. Am. Chem. Soc. 129:*, vol. 129, p. 11708–11719, 2007.

[11] H. Z. Zhong, Y. Zhou, Y. Yang, C. Yang and Y. F. Li, *J. Phys. Chem. C* , vol. 111, p. 6538, 2007.

[12] X. G. Lin, "Used for photovoltaic device of ZnO basetype II heterogeneous structure design," Xiamen University, 2010.

[13] Y. Tak, S. J. Hong, J. S. Lee and K. Yong, *J. Mater. Chem.*, vol. 19, pp. 5945-5951, 2009.

[14] K. Wang, J. J. Chen, W. L. Zhou, Y. Zhang, Y. F. Yan, J. Pern and A. Mascarenhas, *Adv. Mat.* , vol. 20, p. 3248, 2008.

[15] P. T. Chou, C. Y. Chen, C. T. Cheng, S. C. Pu, K. C. Wu, Y. M. Cheng, C. W. Lai, Y. H. Chou and H. T. Chiu, *Chem. Phys. Chem.*, vol. 7, pp. 222-228, 2006.

[16] W. F. Li, Y. G. Sun and J. L. Xu, *Nano Micro Lett.* , vol. 4, no. 2, p. 98, 2012.

[17] A. Malafronte, F. Auriemma, R. D. Girolamo, C. Sasso, C. Diletto, A. E. D. Mauro, E. Fanizza, P. Morvillo, A. M. Rodriguez, A. B. Muñoz-Garcia, M. Pavone and C. D. Rosa, *J. Phys. Chem. C*, vol. 121, no. 30, p. 16617–16628, 2017.

[18] C. Diletto, P. Morvillo, R. Di Girolamo, F. Auriemma and C. De Rosa, *J. Sol-Gel Sci. Technol.*, vol. 73, p. 634−640, 2015.

[19] M. C. Toroker, D. K. Kanan, N. Alidoust, L. Y. Isseroff, P. Liao and E. A. Carter, *Phys. Chem. Chem. Phys.* , vol. 13, p. 16644−16, 2011.

[20] M. Misner, H. Skaff, T. Emrick and T. Russell, *Adv. Mat.*, vol. 15, pp. 221-224, 2003.

[21] T. Thurn-Albrecht, R. Steiner, J. Derouchey, C. M. Stafford, E. Huang, M. Bal, M. Tuominen, C. J. Hawker and T. P. Russell, *Adv. Mater.* , vol. 12, p. 787–791, 2000.

[22] P. Mansky, Y. Liu, E. Huang, T. P. Russell and C. Hawker, *Science*, vol. 275, pp. 1458-1460, 1997.

[23] F. F. Lupi, T. J. Giammaria, M. Ceresoli, G. Seguini, K. Sparnacci, D. Antonioli, V. Gianotti, M. Laus and M. Perego, *Nanotechnology* , vol. 24, p. 315601 , 2013.

[24] S. Förster, M. Zisenis, E. Wenz and M. Antonietti, *J. Chem. Phys.* , vol. 104, no. 24, p. 9956−9970, 1996.

[25] J. F. Tassin, R. L. Siemans, W. T. H. G. Tang, J. D. Swalen and B. A. Smith, *J. Phys. Chem.*, vol. 93, p. 2106, 1989.

[26] C. Sinturel, M. Vayer, M. Morris and M. A. Hillmyer, *Macromolecules*, vol. 46, p. 5399 , 2013.

[27] E. H. I. J. Brandrup and E. A. Grulke, Polymer handbook, Wiley, Hoboken, NJ, 1999, 1999.

[28] C. M. Hansen, Solubility Parameters – An Introduction, Hansen Solubility Parameters, CRCPress, 1999 .

[29] H. Etxeberria, R. Fernandez, I. Zalakain, I. Mondragon, A. Eceiza and G. Kortaberria, *J. Col. and Interf. Sci.*, vol. 416, p. 25–29 , 2014.

[30] T. Ghoshal, A. Chaudhari, C. Cummins, M. T. Shaw, J. D. Holmes and M. A. Morris, *Soft Matter*, vol. 12, p. 5429—5437 , 2016.

CHAPTER 7

Conclusions

In recent years many efforts have been made to design, synthetize and characterize new materials for the fabrication of polymer solar cells (PSCs) with the purpose to achieve a correct compromise between efficiency and stability, fundamental properties for commercialization.

The development of this promising and alternative technology to inorganic photovoltaics (PV) is an effective approach to obtain a more economical, sustainable and environmentally friendly energy.

The aim of the present PhD thesis was the study of different materials and methods for the production of PSCs investigating various aspects such as the fabrication process using scalable deposition techniques of practical interest, the effect of temperature on the degradation process in the realized devices and, at the same time, the preparation and characterization of active layers based on nanostructured inorganic hybrid materials combining the semiconductor properties of nanoparticles (NPs) and self-assembly of block copolymers (BCPs).

In the Chapter 3, special attention was dedicated to the fabrication of the inverted bulk heterojunction (BHJ) organic solar cells with the study of various active layer materials based both on low and wide band-gap polymers as donors and both on fullerene and non fullerene compounds as acceptors.

In the first part of this section, the optimization of performance of PTB7-Th:[70]PCBM-based devices was investigated through an accurate study of active layer physical properties. A power conversion efficiency (PCE) of 9.17% was obtained by using the configuration glass/ITO/ZnO/PTB7-Th:[70]PCBM/MoO_x/Ag.

In order to understand the influence of temperature on the active layer, thermal tests were carried out at different temperatures. The study highlighted that the device performances remain substantially unchanged up to 80°C whereas a serious degradation was observed for higher temperatures due, probably, to the irreversible fullerene aggregation. Therefore, the active layer morphology can be considered thermal stable at 80 °C and, for this reason, this temperature was selected for the following working steps.

In order to realize a fully solution-processed solar cell, PSCs were fabricated by replacing evaporated materials such as MoO_x HTL layer with solution-processed alternatives and compatible with printing techniques, like PEDOT:PSS (annealed at 80°C instead of standard temperature 120°C). The PCE of the devices so realized was around 5%.

Moreover, a comparative study of the photovoltaic behavior of PSCs (with solution-processed PEDOT:PSS as HTL) built up using Ag back electrodes made via thermal evaporation and by screen-printing using a commercially Ag paste (heat cured at T=80°C) was made. A rapid deterioration of the electrical performance occurred when screen-printed Ag was used as back electrode. This was probably due to a too low curing temperature (T=80°C) of Ag paste and, therefore, the ink solvents remain trapped in the layer and, then, leak in and partly dissolves the underlying active layer.

The fabrication of all solution-processed solar cells is one the most fundamental challenges in the OPV field and this preliminary study

confirms that a careful selection of materials properties constituting the active layer is necessary and useful in order to tackle degradation process and low efficiency.

In the second part of this OPV section, the PBDB-T:ITIC-based solar cells were fabricated. This blend was chosen because it represents a promising optical, electrical and thermal stable combination.

The devices were optimized in inverted configuration (ITO/ZnO/ PBDB-T:ITIC/MoO_x/Ag) achieving as best result a PCE of 10.2 %.

The subsequent incorporation of a solution-processed HTL layer such as PEDOT:PSS, instead of evaporated MoO_x, led to a promising PCE of 7.3%.

Lifetime tests to verify the thermal and photostability were carried out on so prepared devices. In particular, the study highlighted a good stability after application of thermal stress at 100°C for 44 hours in dark and under inert atmosphere. However, a rapid and progressive deterioration of PSC performance was recorded after the light exposure for 30 minutes.

In order to improve the photovoltaic performance of PBDB-T:ITIC-based PSCs, ternary PSCs were also fabricated. In fact, the third component can play a key role thanks to the possible benefits that may derive from its use such as an enhancement of photon harvesting, a good energy level alignment, more efficiency of exciton dissociation, charge transport and extraction, a better stability and a good morphology.

Ternary PSCs were fabricated both with the configuration of either two donors/one acceptor (D1:D2:A) and one donor/two acceptors (D:A1:A2). In the former case, the influence of near-infrared (NIR) sensitizer, PDTP-DFBT polymer, in the ternary system was studied. In particular, the presence of third component gave a contribution to blend absorption in the 750-900 nm region but it did not lead to significant improvements for the electrical performance. This probably happened because there was not a

favorable supramolecular assembly in the blend film for achieving an optimal morphology and, thus, to promote an efficient charge dissociation and transport.

In the latter case, the active layer consisted of PBDB-T as donor polymer, ITIC as first acceptor and [70]PCBM as second acceptor. The incorporation of sensitizer led to a satisfying improvement of J_{SC}, compared to the binary control device based on PBDB-T:ITIC, with the overall PCE of ternary solar cell is ~9%.

In general, PBDB-T:ITIC-based PSCs possess a high potential for advancing PSCs technology and, for this reason, further investigations in the ternary field should be carried out as a promising way toward higher performance.

In the Chapter 4, the lamination method for the production of all-solution processable solar cells was investigated. It is an effective and appealing approach to realize low-cost, flexible and semitransparent PSCs for versatile applications.

In particular, ternary non fullerene-based polymer solar cells and mini-modules, coated on flexible PEDOT:PSS electrodes and processed by scalable roll lamination method, were fabricated. The active layer was based on novel materials combination, that is, TQ1 as donor polymer, IDTBR and IDFBR as first and second non fullerene acceptors, respectively.

The blend is an optically promising combination thanks to an optimal complementarity among materials absorption spectra in whole visible range. However, the devices were characterized by poor performance probably due to a not so efficient energy level alignment which may have caused recombination phenomena or traps in the active layer.

Moreover, in this study, an attempt of building series connected mini-modules was also performed. In particular, the blend layer was deposited both by spin coating and by blade coating (the latter is a technique fully compatible with roll-to-roll production). In both the examined cases, the mini-modules did not work. The electrical parameters were very low probably due to several factors that can affect both the fabrication process and the functioning of modules and, among these, the poor performance of the ternary blend should be also surely considered.

Nevertheless, these results can offer guidelines for the fabrication of flexible organic solar cells and modules with particular attention to the choice of active layer materials and the optimal lamination conditions in order to obtain an improvement of device performance and a better interfacial contact between the layers used as adhesive.

The lamination approach represents my research activity pursued during my stage abroad (three months) in the Research Group "Biomolecular and Organic Electronics" leaded by Prof. Olle Inganäs.

Finally, in the Chapter 6, the self-assembly of block copolymers (BCPs) was studied in order to make active layers for hybrid PSCs based on well-ordered polymeric morphology hosting *n*- and *p*-type semiconductor nanoparticles (NPs) in different domains. Herein, type II-heterojunction is formed by intimately mixing two different semiconductors such as ZnO/CdSe NPs.

The first step of this research was devoted to the preparation of hybrid nanocomposites based on *n*-type ZnO NPs and PS-b-PMMA copolymer. In particular, a simple BCP-based method to control the spatial arrangement of the ZnO NPs on solid supports (ITO-coated glass slides) was set up, obtaining thin films of hybrid nanostructured material with

promising electrical properties. Thin films characterized by selective inclusion of the surface-modified ZnO NPs in the lamellar PS nanodomains were successfully prepared by using self-assembly of a PS-b-PMMA block copolymer combined with thermal annealing treatments. ZnO NPs decorated at the surface with HDA and TBPA molecules were purposely synthesized to favour selective inclusion in the PS domains. The thermal treatment allowed obtaining in one step the vertical orientation of the lamellar BCP nanodomains and the migration of the NPs to the PS domains. The successive step of my activity in this field was focused on the fabrication of nanocomposites based on PS-b-PMMA and *p*-type CdSe nanoparticles.

The adopted approach is based on the selective degradation of sacrificial PMMA blocks from a self-assembled block copolymer structure and the subsequent backfilling of the porous structure with the inorganic NPs.

In particular, a procedure that allows building PS-b-PMMA nanoporous thin films was optimized by employing UV radiation for 1h followed by an acetic acid washing for 30 minutes. The resultant BCP morphology after PMMA removal was not reproducible showing a random orientation of BCP lamellae to the surface of ITO substrate due to preferential interactions of the polymer blocks at the interface with air and support.

Highly reproducible results could be achieved resorting to the neutralization process of the ITO surface through a grafting reaction with OH-terminated PS-r-PMMA. The use of the so-neutralized ITO surface allowed obtaining not only the desired perpendicular orientation of the lamellae in the PS-b-PMMA thin films, but also maintaining the perpendicular orientation of PS domains, after removal of PMMA blocks. Accordingly, a facile and robust approach was devised to prepare

nanoporous surfaces, characterized by interconnected channels with diameter of ≈8 nm, delimited by PS blocks of the initial PS-b-PMMA BCP. In a further research line, focused in the realization of hybrid nanocomposites exploiting self-assembly of BCP coupled with the selective incorporation of semiconductor nanoparticles, suitable protocols allowing to control the morphology of PS-b-P4VP were attempted.
Along this research line, several tests were carried out by submitting the BCP thin films to solvent vapor annealing treatments in order to obtain the lamellar morphology, as PS-b-P4VP presents a strong tendency to form micellar aggregates both in solutions and in thin films obtained by solvent evaporation.

In conclusion, the research activity performed within this PhD thesis was focused on the implementation of suitable strategies for the fabrication of polymer solar cells (PSCs) to improve the device performances. To this aim, several materials having specific chemical and physical properties were used, and new strategies for fabrication of solar cells were implemented using simple techniques of practical interest, in a view to develop feasible scale up processes. For each approach the efficiency limiting factors were identified, providing useful scientific basis for future investigations. Moreover, this work confirmed that the use of spontaneous BCPs self-assembly is a potential strategy to create tailored organic nanostructures able to precisely incorporate inorganic semiconductor nanoparticles (NPs) for the realization of active layers in the hybrid PSCs.

APPENDIX

A.1 I-V measurements

The electrical characteristics of the hybrid nanocomposites based on the BCP and PS matrices were evaluated by current/voltage (I−V) dark measurements in a previous work [1, 2]. The electrical behaviors were tested on a device in a sandwich architecture ITO/BCP-ZnO (or PS-ZnO) film/Al and the results are reported in Fig. A1.1.

A

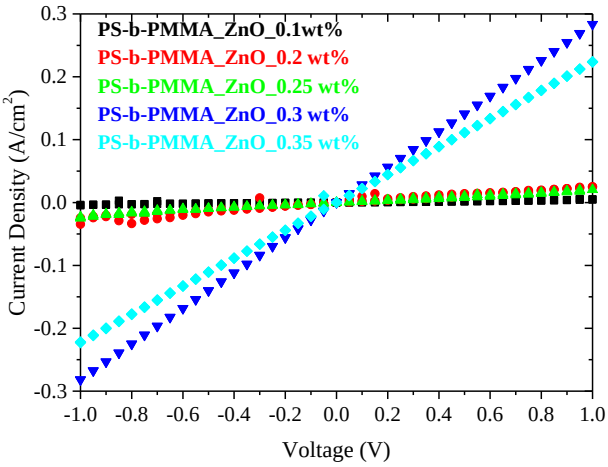

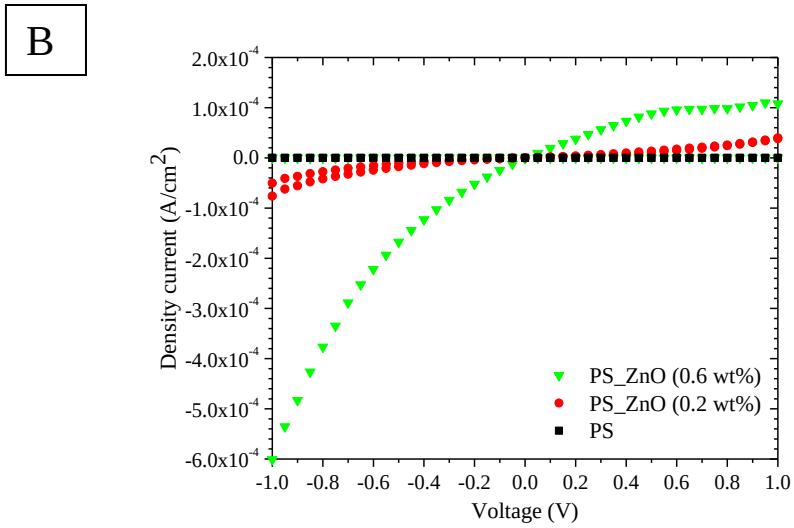

Fig. A1.1. measurements of ITO/BCP-ZnO/Al (A) and ITO/ PS-ZnO/Al (B) devices. For the device in (A), films of BCP with 0.1, 0.2, 0.25, 0.3 and 0.35 wt% ZnO NPs were tested. For the device in (B), neat PS and nanocomposites PS-ZnO containing 0.2 and 0.6 wt % of ZnO were tested. The relative error in density current is in the range 10−12%.

I−V measurements (Fig. A1.1A) were cyclically performed on the BCP-based nanocomposites and the I−V data show almost null current density for ZnO NPs content lower than a critical value of ∼0.25 wt %. For ZnO NPs concentrations of 0.3 and 0.35 wt %, the current density shows a linear increase with the voltage and from the slope of these I−V curves (0.282 and 0.222 A V^{-1} cm^{-2}, respectively) a conductivity of ∼7 × 10^{-6} S cm^{-1} can be roughly estimated, considering a global thickness of ∼300 nm for the device, where 300 nm is the sum of the thickness of the top and bottom electrodes (∼130 nm) and of the intermediate nanocomposite layer (∼70 nm). This indicates that an ohmlike conductive regime of the BCP-based nanocomposites is established for NPs concentrations higher than a critical value c* comprised between 0.25 and 0.3 wt %. Only above this critical concentration the NPs included in the PS domains are able to form a

continuous percolative path of charge carriers, which facilitates the current conduction.

Moreover, these data are compared with the electrical properties of the PS-ZnO nanocomposites (Fig. A1.1B) containing amounts of ZnO NPs (0.2 and 0.6 wt %) lower and higher than the aforementioned threshold concentration c*. It is apparent that the current density is negligibly small even at high loadings of ZnO NPs.

These results confirm that the key for the obtainment of conductive properties resides in the formation of a continuous path of charge carriers, achieved through the confinement of the semiconductor nanoparticles in the vertical BCP nanodomains as described in the section 6.2.

Bibliography of Appendix

[1] C. Diletto, “Nanostructured polymeric materials for morphology control on nanometer scale and nanotechnology applications,” Università degli Studi di Napoli “Federico II”, 2014.

[2] A. Malafronte, F. Auriemma, R. D. Girolamo, C. Sasso, C. Diletto, A. E. D. Mauro, E. Fanizza, P. Morvillo, A. M. Rodriguez, A. B. Muñoz-Garcia, M. Pavone and C. D. Rosa, *J. Phys. Chem. C*, vol. 121, no. 30, p. 16617–16628, 2017.